The Astrophysical Journal Supplement Series, 250:1 (45pp), 2020 September https://doi.org/10.3847/1538-4365/aba2c7

A Comprehensive Power Spectral Density Analysis of Astronomical Time Series. I. The Fermi-LAT Gamma-Ray Light Curves of Selected Blazars

Mariusz Tarnopolski[1], Natalia Żywucka[2], Volodymyr Marchenko[1], and Javier Pascual-Granado[3]
[1] Astronomical Observatory, Jagiellonian University, Orla 171, 30-244, Kraków, Poland; mariusz.tarnopolski@uj.edu.pl, volodymyr.marchenko@oa.uj.edu.pl
[2] Centre of Space Research, North-West University, Potchefstroom, South Africa; n.zywucka@oa.uj.edu.pl
[3] Instituto de Astrofísica de Andalucía—CSIC, E-18008 Granada, Spain; javier@iaa.es
Received 2020 March 14; revised 2020 June 24; accepted 2020 June 24; published 2020 August 20

Abstract

We present the results of the Fermi-Large Area Telescope 10 yr long light curve (LC) modeling of selected blazars: six flat-spectrum radio quasars (FSRQs) and five BL Lacertae (BL Lacs), examined in 7, 10, and 14 day binning. The LCs and power spectral densities (PSDs) were investigated with various methods: Fourier transform, Lomb–Scargle periodogram (LSP), wavelet scalogram, autoregressive moving average (ARMA) process, continuous-time ARMA (CARMA), Hurst exponent (H), and the $\mathcal{A}$–$\mathcal{T}$ plane. First, with extensive simulations we showed that parametric modeling returns unreliable parameters, with a high dispersion for different realizations of the same stochastic model. Hence, any such analysis should be supported with Monte Carlo simulations. For our blazar sample, we find that the power-law indices β calculated from the Fourier and LSP modeling mostly fall in the range $1 \lesssim \beta \lesssim 2$. Using the wavelet scalograms, we confirm a quasi-periodic oscillation (QPO) in PKS 2155−304 at a 3σ significance level, but do not detect any QPOs in other objects. The ARMA fits reached higher orders for 7 day binned LCs and lower orders for 10 and 14 day binned LCs for the majority of blazars, suggesting there might exist a characteristic timescale for the perturbations in the jet and/or accretion disk to die out. ARMA and CARMA modeling revealed breaks in their PSDs at timescales of a few hundred days. The estimation of H was performed with several methods. We find that most blazars exhibit $H > 0.5$, indicating long-term memory. Finally, the FSRQ and BL Lac subclasses are clearly separated in the $\mathcal{A}$–$\mathcal{T}$ plane.

Unified Astronomy Thesaurus concepts: Active galactic nuclei (16); Blazars (164); Light curves (918); Time series analysis (1916); High energy astrophysics (739); BL Lacertae objects (158); Quasars (1319)

Supporting material: figure sets

1. Introduction

Blazars are jetted radio-loud objects, which constitute a peculiar class of active galactic nuclei (AGNs). They are originally defined as extragalactic objects that possess a nonthermal continuum along the entire electromagnetic spectrum, exhibit a high degree of radio-to-optical polarization as well as compact radio emission, and whose relativistic jets point toward an observer (see, e.g., Angel & Stockman 1980; Urry & Padovani 1995; Padovani et al. 2017 for a review). Blazars show variability in different energy bands, often rapid with short-lasting flares, from months down to minutes (Wagner & Witzel 1995; Rani et al. 2010b; Nilsson et al. 2018). They are commonly divided into two subgroups, i.e., flat-spectrum radio quasars (FSRQs) and BL Lacertae (BL Lac) objects, based on characteristics visible in their optical spectra. FSRQs have prominent emission lines with equivalent width >5 Å, while spectra of BL Lacs are featureless (with a smooth continuum) or display weak lines only. This division can be also done based on different accretion regimes of AGNs, i.e., FSRQs have high accretion rates while BL Lacs have low accretion rates (Ghisellini et al. 2011). Moreover, taking into account the position of the synchrotron peak, $\nu_{\rm peak^s}$, of the spectral energy distribution (SED; in the ν–νF plane), BL Lacs are split into low-peaked (LBL), intermediate-peaked (IBL), and high-peaked (HBL) BL Lacs (Abdo et al. 2010b). An additional group of extreme HBLs, having $\nu_{\rm peak^s} \gtrsim 10^{17}$ Hz, is also considered (Costamante et al. 2001; Akiyama et al. 2016).

Over the years, many multiwavelength as well as different single-energy-band studies have been conducted to investigate the physical processes causing the variability visible in blazars' light curves (LCs), especially their power spectral densities (PSDs). In particular, the timescales at which the PSD changes its character, e.g., breaks, could give an indication of the emission regions, i.e., accretion disk, in for instance FSRQs, microquasars, or X-ray binary systems, or the jet in BL Lacs, and thus of the physical mechanism of the observed variations caused in these regions. Several LC investigations were based on the high-energy (HE; $E > 100$ MeV) γ-ray Fermi-Large Area Telescope (LAT) data. Eleven months long weekly binned LCs of 104 blazars, including 58 FSRQs, 42 BL Lacs, and 4 objects with uncertain classification, were analyzed by Abdo et al. (2010c). Their PSDs were obtained with the structure function (SF) and fitted with a power law (PL), $1/f^{\beta}$, giving an index of $1.1 \lesssim \beta \lesssim 1.6$ for a majority of blazars. It was also found that the FSRQs, LBLs, and IBLs show larger variations than HBLs, wherein all studied blazars can be described as steady sources with a series of flares. Sobolewska et al. (2014) studied 4 yr long, adaptively binned, densely sampled Fermi-LAT LCs of 13 well-known and bright blazars, i.e., 8 FSRQs and 5 BL Lacs. The LCs were modeled with the Ornstein–Uhlenbeck (OU) process and a superposition of OU processes (sup-OU). It turned out that the majority (i.e., 10) of investigated objects are better described by the sup-OU model, with the PL index $\beta \sim 1$. It is worth mentioning that the index does not depend on the

redshift or blazar classification. Recently, Ryan et al. (2019) analyzed long-term (9.5 yr) daily and weekly binned Fermi-LAT LCs (taken from the Fermi Science Support Center[4]) of 13 blazars previously studied by Sobolewska et al. (2014). The LCs were analyzed with the continuous-time autoregressive moving average (CARMA) model (Kelly et al. 2014), indicating that the OU processes, i.e., CARMA(1, 0), do not pick up the characteristics of variability in the data, while higher-order processes, i.e., CARMA(2, 1), provide a much better description of the variability. The multiwavelength analysis of the famous source OJ 287 yielded CARMA(1, 0) as the best fit for the HE data, while optical and radio LCs (with many more measurements) exhibited higher-order CARMA models (Goyal et al. 2018).

Regarding the PSD study, quasi-periodic oscillations (QPOs) in AGNs, where a QPO is defined as the "concentration of variability power over a limited frequency range" (Vaughan & Uttley 2005), may help to establish the variability regions and physical processes responsible for variability as well as to place constraints on the black hole (BH) mass estimations as it is in the case of microquasars, neutron stars, and X-ray sources (e.g., Stella & Vietri 1998; Muno et al. 1999; Abramowicz et al. 2004; Török et al. 2005). Most of the analyses aimed at searching for QPOs focus around different implementations of periodograms and scalograms. Espaillat et al. (2008) analyzed the X-ray XMM-Newton LCs of 10 bright AGNs. The observations were conducted in the energy range of 0.75–10 keV, while the analysis was performed with the continuous wavelet transform (CWT) and the SF. A QPO was found for only one AGN, i.e., 3C 273, with a period of 55 minutes at a significance level $>3\sigma$, and the range of BH mass was estimated as $[7.3 \times 10^6, 8.1 \times 10^7]\,M_\odot$. Lachowicz et al. (2009) looked for QPOs in the 0.3–10 keV band observations of PKS 2155−304 by analyzing a 64 ks XMM-Newton LC with the multiharmonic analysis of variance periodogram (Schwarzenberg-Czerny 1996), the SF, and the wavelet scalogram (Torrence & Compo 1998). A QPO with a period of ∼4.6 hr was found in the data at $>3\sigma$ significance level, which allowed the authors to estimate the BH mass to be within the range $[3.3 \times 10^7,\ 2.1 \times 10^8]\,M_\odot$. Gupta et al. (2009) collected a set of 20 V and R filter optical LCs of the blazar PKS 0716+714, lasting from 7.7 hr up to 12.3 hr. Each LC was studied separately with a wavelet plus randomization technique, giving a set of possible QPO timescales and corresponding BH mass estimates (see Table 1 in Gupta et al. 2009 for details). Subsequently, Rani et al. (2010a) studied a 9.6 hr long R-band optical LC of PKS 0716+714, delivered by the Physical Research Laboratory in India, using the SF and Lomb–Scargle periodogram (LSP), as well as fitting a pure PL to the derived PSD. The authors found a QPO with a period of ∼3 minutes with significance $>3\sigma$. The BH mass was estimated to be within $[1.5 \times 10^6, 9.6 \times 10^6]\,M_\odot$. In the four examples of a QPO search in the X-ray data presented above, the lower value of the BH mass estimation is based on a nonrotating BH model, while the higher value stems from the assumption of a maximally rotating BH. It was also assumed that a QPO is connected to fluctuations in the accretion disk and its timescale corresponds to an orbital timescale originating near the last stable orbit, i.e., the innermost parts of the accretion disk. On the other hand, the BH mass estimates of 3C 273 given by Espaillat et al. (2008) do not agree with previous values obtained with the reverberation-mapping method or the correlation between host galaxy luminosity and BH mass. This suggests that the QPO found in X-ray data rather does not originate in the inner parts of the accretion disk, as it is in the case of microquasars, neutron stars, and X-ray sources.

Regarding a search for QPOs in AGNs, especially blazars, in the HE γ-ray regime, Fermi-LAT provides long-term, high-quality, and densely sampled data of many bright and well-known sources. For example, Ackermann et al. (2015) analyzed the ∼6.9 yr long LC of the blazar PG 1553+113 in the energy range 0.1–300 GeV, with the LSP and the CWT. They found a possible QPO with a period of 798 ± 30 days, where the γ-ray signal peaked at >99% confidence level. The authors stressed that the presence of a binary supermassive BH (SMBH) could initiate the observed long-term quasi-oscillations. Prokhorov & Moraghan (2017) investigated 10 γ-ray sources, including 3 binary systems and 7 blazars. The blazars' LCs, spanning over 7.8 yr in the energy range 0.3–500 GeV, were analyzed with the generalized LSP (Zechmeister & Kürster 2009). QPOs were found in three cases, i.e., PG 1553+113, PKS 2155−304, and BL Lacertae, with periods of 798, 644, and 698 days, respectively; the QPOs reached the significance level $>5\sigma$. The remaining blazars from this sample are considered as candidates for blazars with QPO signals in their γ-ray emission as well as blazars having a binary SMBH at their central regions. Zhou et al. (2018) analyzed 10 yr long data in the energy range 0.1–300 GeV, using the weighted wavelet Z-transform (WWZ) and LSP. A QPO in PKS 2247−131 with a period of ∼34 days with a significance of $\sim 4.6\sigma$ was found, supporting the suggestion that the flux quasi-oscillation is caused by the helical structure of the jet. Tavani et al. (2018) reanalyzed the same data of PG 1553+113 as Ackermann et al. (2015), extending the LC by two subsequent years. Using the CWT, the authors confirmed the QPO and its period found by the previous study of this blazar and, again, interpreting the quasi-oscillation in the signal to be a result of the binary SMBH system.

A bunch of possible interpretations of QPOs appearing in the blazar multiwavelength data was introduced and discussed in recent literature. The short-term, monthly, periodic modulation may arise directly in the jet due to its helical structure, intrinsic rotation, or precession (e.g., Rieger 2004; Vlahakis & Königl 2004; Caproni et al. 2013) as well as by processes causing perturbations and instabilities in the accretion disk–jet system (e.g., Romero et al. 2000; Pihajoki et al. 2013). Another widely discussed possible origin of a QPO is the presence of a gravitationally bound binary SMBH at the center of a blazar, which might cause instabilities in the jet (e.g., Katz 1997; Valtonen et al. 2008; Cavaliere et al. 2017; Holgado et al. 2018). However, the origin of radio, optical, X-ray, and γ-ray QPOs is still uncertain. In particular, QPOs might as well arise from intrinsically aperiodic stochastic processes without a connection to any physical periodic behavior underlying the observed variability. QPOs naturally appear in many stochastic autoregressive (AR) models, starting with AR(2) as the simplest such model that allows a Lorentzian-like peak in its PSD. Therefore, an apparent quasi-periodicity need not be a real physical periodicity, but form due to particular auto-correlations present in the governing process.

[4] http://fermi.gsfc.nasa.gov/ssc/data/access/lat/msl_lc/

We aim to conduct a comprehensive analysis of the temporal properties of blazar LCs, in particular constraining the shape and features of the PSD, by employing a wide range of methods and performing extensive testing of their reliability. We start, in Section 2, by describing the preparation of data, in particular the processing of Fermi-LAT data to produce the LCs (Section 2.1), followed by justifying the nonlinear model that allows flux values to be transformed to amplitudes of the underlying stochastic process governing the variability (Section 2.2) and outlining the algorithm for interpolating missing data (Section 2.3). The overall purpose of this paper is threefold: first, we aim (in Section 3) to provide a possibly exhaustive, yet compact, mathematical description of the various time-series analysis techniques employed further on. Section 3 can be considered as a tutorial, explaining what the methods can and cannot do. Second, we validate them in Section 4 by extensive benchmark testing. The design was to ascertain the reliability of outcomes returned by each method. We describe the levels to which they provide reliable results and highlight, in particular, that owing to genuine randomness of stochastic processes, different realizations of the same process can lead to remarkably different results. Finally, in Section 5, we apply all these methods to γ-ray LCs of some of the brightest or otherwise famous blazars, bearing in mind the limitations uncovered in Section 4. Most of the chosen blazars have been intensively examined in the literature, allowing for a detailed comparison with our results. We also investigate some objects that recently gained more attention (TXS 0506+056, PKS 1830−211) in an attempt to provide insight into their driving mechanisms. In Section 6.1 we discuss the results, comparing them with previous findings from the literature (Section 6.2), putting them in context (Section 6.3), and listing several applications for the employed methodology (Section 6.4). This work can therefore be considered either from the point of view of a critical evaluation of some computational techniques (Sections 3 and 4), or purely from the point of astrophysical research (Sections 2, 5, 6). A brief summary of our findings is provided in Section 7. As a whole, it forms a comprehensive overview of variable astrophysical sources, blazars in particular.

2. Data

2.1. Processing of Fermi data

The Fermi-LAT (Atwood et al. 2009) is a HE γ-ray telescope, sensitive to photons in the energy range from 20 MeV to 300 GeV and with a wide field of view of 2.4 sr. It allows individual sources, such as point-like AGNs, to be resolved; transients to be detected; and variability to be monitored.

We performed a standard binned maximum likelihood analysis[5] using the latest 1.2.1 version of FERMITOOLS, i.e., the conda distribution of the Fermi ScienceTools,[6] and the FERMIPY (Wood et al. 2017) facilities. The binned likelihood analysis is recommended to analyze long time periods and large bins of bright known sources. It allows us to balance the accuracy of analyses with their execution time and computational power. All data analyzed here come from the LAT 8 yr Source Catalog (4FGL; Abdollahi et al. 2020), spanning the time range of 239557417–577328234 MET, i.e., 2008 August 4 to 2019 April 19, giving in total ∼11 yr of data. In the binned analysis, we defined the spatial bin size to be $0.^{\circ}1$, and the number of energy bins per decade is 8. We considered the 128 event class, i.e., events having a high probability of being photons, from the region of interest (ROI) of 10°, centered on the selected blazars, and the event type equal to 3. We used the energy range between 100 MeV and 300 GeV. The HE level was introduced to avoid energy reconstruction oversaturation; while analyzing photons <100 MeV, a point-spread function gets large and the event reconstruction is not accurate enough (see, e.g., Atwood et al. 2007; Principe et al. 2018 for more details). The zenith angle was set to 90° to avoid Earth's limb, which is a strong γ-ray background source. Additionally, we made sure that the data quality is good enough and the time intervals are proper by choosing `DATA_QUAL > 0` and `LAT_CONFIG == 1` options. Finally, we used the instrument response function `P8R3_SOURCE_V2` and the latest Pass 8 background models, i.e., the Galactic diffuse emission (`gll_iem_v07.fits`) and the extragalactic isotropic diffuse emission (`iso_P8R3_SOURCE_V2_v1.txt`) models, also including all known point-like foreground/background sources in the ROI.

We generated a set of three LCs for each blazar (see Section 2.5 for a description of the objects), using three time bins, i.e., 7, 10, and 14 days, and including observations with test statistic TS > 25 (significance of $\gtrsim 5\sigma$). They are displayed in Figures 1 and 2.

2.2. Nonlinear Model

Blazars often exhibit flares during which their brightness increases by several orders of magnitude. Such occurrences make the observed LCs highly nonstationary, making their analysis difficult. The most straightforward method of converting a nonstationary time series to a stationary one is to differentiate the series, i.e., to investigate the consecutive differences of the original data. Such an approach is natural for linear processes (Section 3.6.5). However, taking the logarithms of the fluxes is another way and an astrophysically motivated one. Indeed, one can write

$$f(t) = \exp[l(t)], \tag{1}$$

where $f(t)$ is the LC, and $l(t)$ is some stochastic process underlying the observed variability. Equation (1) carries meaning when (Uttley et al. 2005)

1. the distribution of the observed fluxes is lognormal, and
2. the rms–flux relation is linear.

The rms is the amplitude of the variability, i.e., it is the standard deviation of the time series' values. To examine how the rms depends on the flux, one proceeds as follows:

1. Divide the LC into k non-overlapping segments, each consisting of N_j points, $j = 1, \ldots, k$.
2. Compute the mean, $\bar{f}_j$, of fluxes $\{f_i\}_j$ in the jth segment.
3. In each segment, compute the rms. The variance in the LC is a sum of the true variability and the uncertainties of the flux measurements. Therefore, one should consider the excess variance (Vaughan et al. 2003):

$$\sigma_{xs,j}^2 = S_j^2 - \overline{\sigma_{\mathrm{err}}^2}_{,j}, \tag{2}$$

[5] https://fermi.gsfc.nasa.gov/ssc/data/analysis/scitools/binned_likelihood_tutorial.html
[6] https://github.com/fermi-lat/Fermitools-conda/wiki

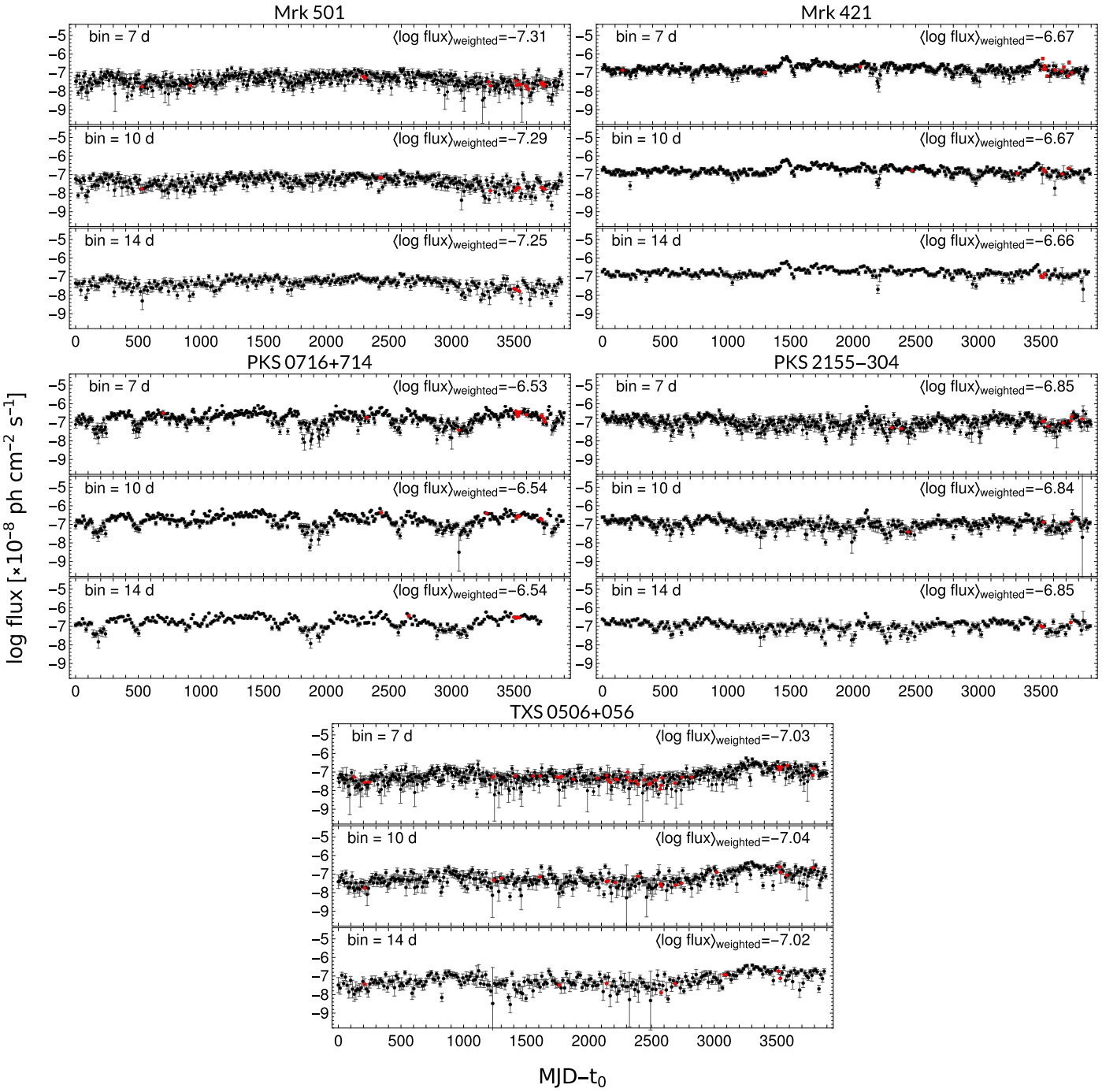

Figure 1. Logarithmic LCs of BL Lacs. The red points are the interpolations done with MIARMA. The uncertainties of the weighted means are $\leqslant 0.01$.

where

$$S_j^2 = \frac{1}{N_j - 1}\sum_{i=1}^{N_j}(f_i - \bar{f}_j)^2 \tag{3}$$

is the variance in the jth segment, and

$$\overline{\sigma_{\rm err}^2}_{,j} = \frac{1}{N_j}\sum_{i=1}^{N_j}\Delta f_i^2 \tag{4}$$

is the mean square error. Then, the rms is $\sigma_{xs,j}$.

4. The standard error of $\bar{f}_j$ is the standard error of the mean, i.e., $\Delta\bar{f}_j = \sigma_j/\sqrt{N_j}$, where σ_j is the standard deviation of the fluxes.
5. The error of the rms is computed herein via the law of error propagation:

$$\Delta\sigma_{xs,j} = \frac{1}{2\sigma_{xs,j}}\sqrt{\Delta S_j^2 + \Delta\overline{\sigma_{\rm err}^2}_{,j}}, \tag{5}$$

for which one needs to know the errors of S_j^2 and $\overline{\sigma_{\rm err}^2}_{,j}$.

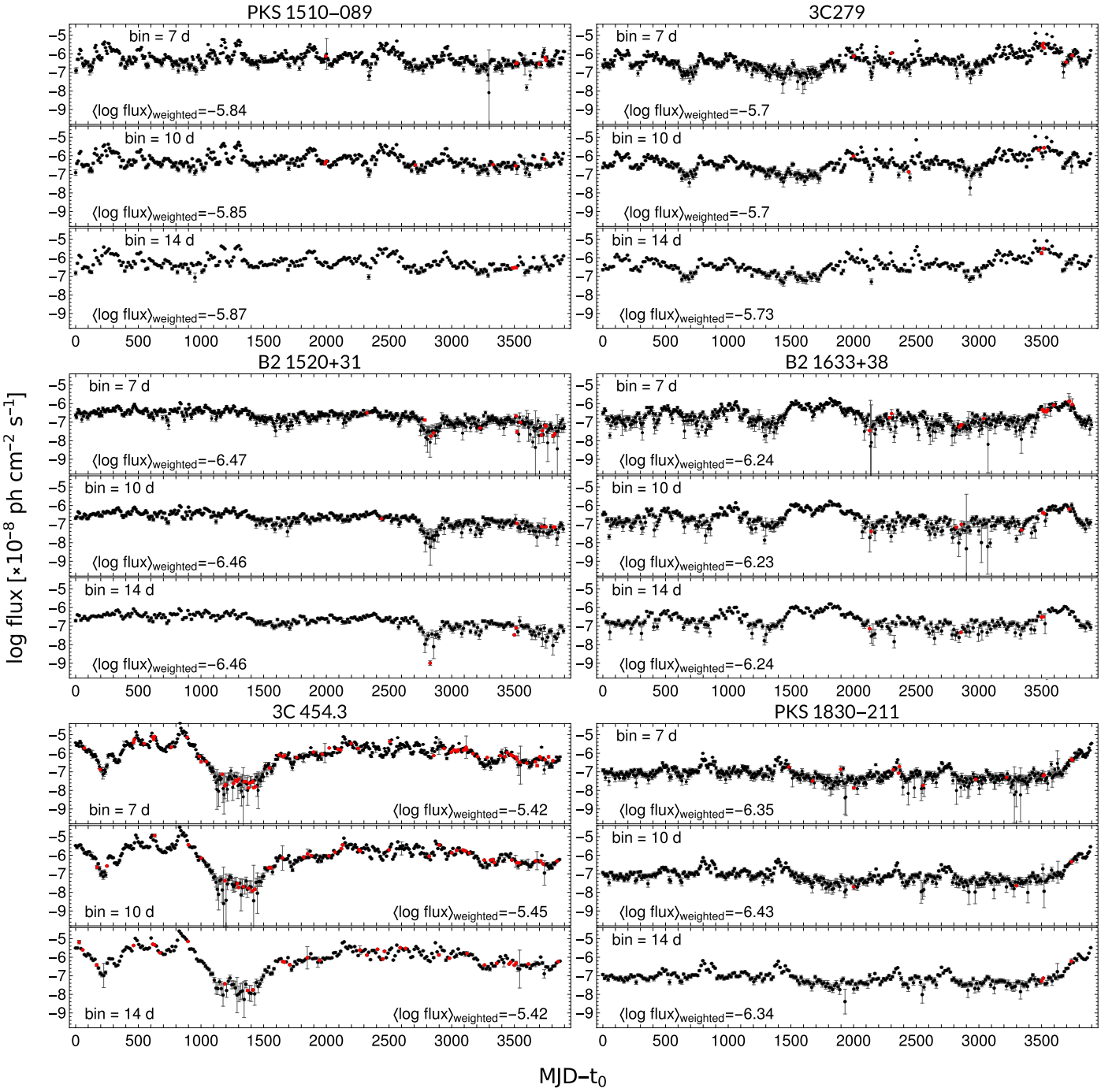

Figure 2. Same as Figure 1, but for FSRQs.

6. The error of S_j^2 is given as (Rao 1973)

$$\Delta S_j^2 = \sqrt{\frac{1}{N_j}\left(\mu_{4,j} - \frac{N_j - 3}{N_j - 1} S_j^4\right)}, \tag{6}$$

where $\mu_{4,j}$ is the fourth central moment.

7. Because $\sigma_{\mathrm{err},j}^2$ is the mean of squares, its error, $\Delta\overline{\sigma_{\mathrm{err},j}^2}$, will therefore be the standard error of the mean (calculated as in point 4.)
8. One finally obtains k pairs $(\bar{f}_j, \sigma_{xs,j})$, each equipped with uncertainties $(\Delta\bar{f}_j, \Delta\sigma_{xs,j})$.

In Figures 3 and 4 the rms–flux relations are shown for all objects considered herein. Each object is analyzed in three binnings, indicated by the colors. The LCs were divided into $k \sim 20$ segments. Fitting a straight line when each point possesses uncertainties in both x and y directions is performed via weighted orthogonal regression[7] (York 1966). In all instances, the slopes were positive when taking into account their errors—even for the dimmest among the considered sources, i.e., Mrk 501, for which the linearity of the rms–flux relation is ambiguous. Also displayed are the probability

[7] https://mathematica.stackexchange.com/a/13122/22013

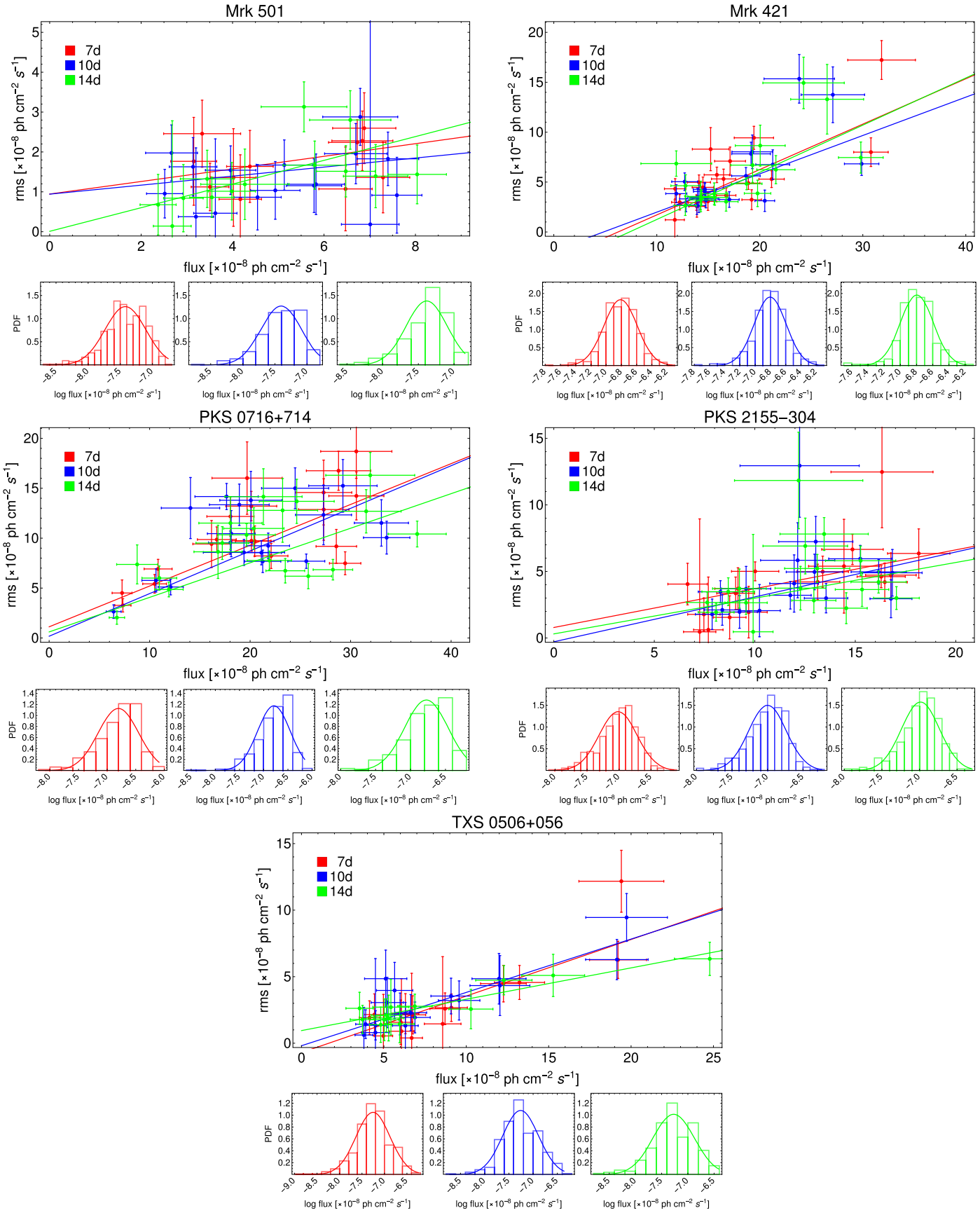

Figure 3. The rms–flux relations and logarithmic distributions of flux for BL Lacs.

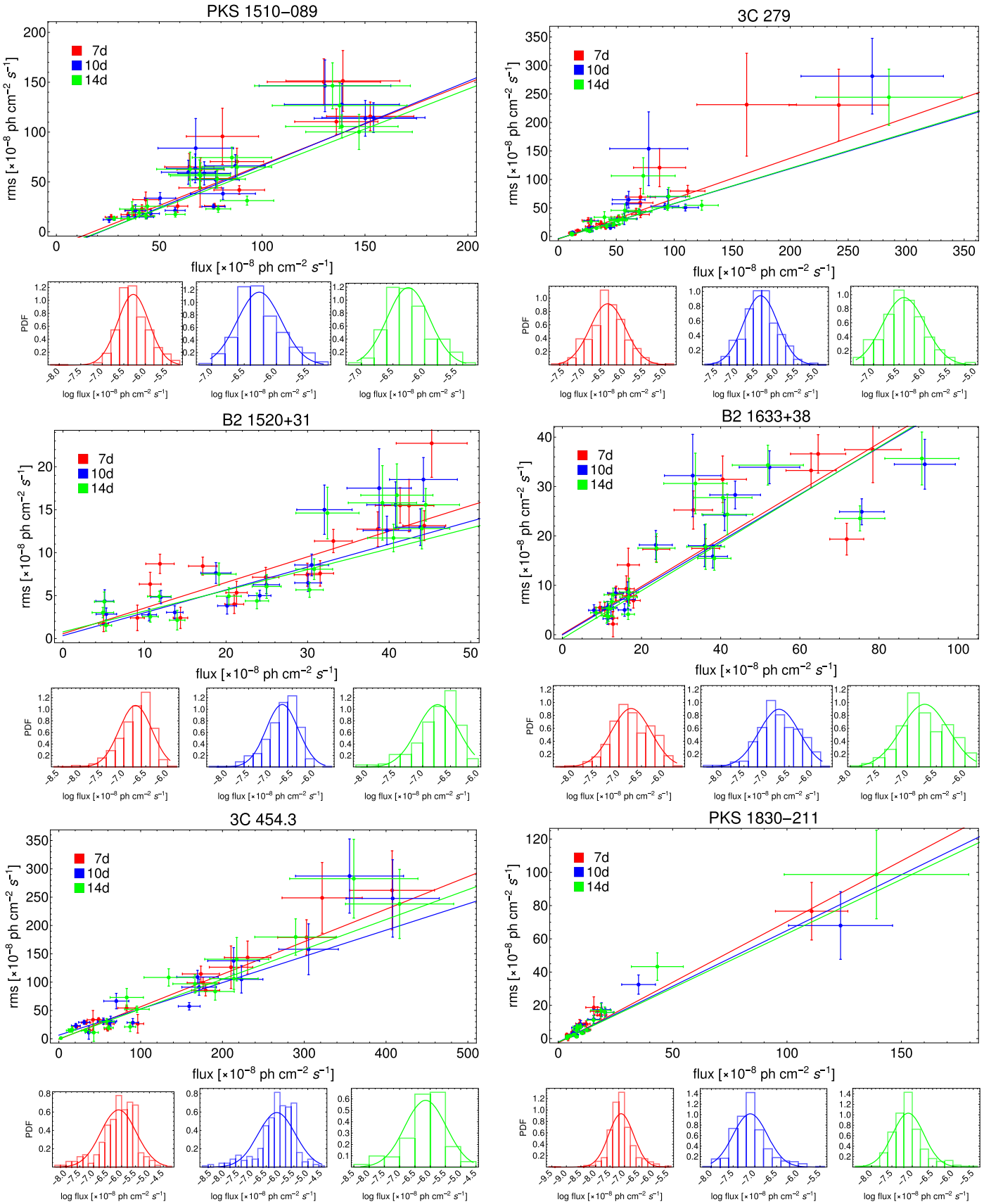

Figure 4. Same as Figure 3, but for FSRQs.

density functions (PDFs) of the logarithmic fluxes, with best-fitting Gaussians overlaid. We emphasize that the distribution fitting was performed by maximizing the log likelihood over the data, not by a regression to the histograms, which are displayed for illustration only. The results for Mrk 421, PKS 1510−089, and B2 1520+31 are consistent with those of Kushwaha et al. (2017). Overall, we conclude that utilizing Equation (1) is justified. Therefore, hereinafter we investigate the underlying process $l(t)$ by analyzing the (decimal) logarithms of the fluxes. Note, however, that steep PSDs ($\beta \gtrsim 1$, i.e., nonstationary processes) might lead to flux distributions being neither normal nor lognormal (Morris et al. 2019).

2.3. Interpolation

The fraction of missing data varies from one LC to another, ranging in our sample from 0.4% up to 13%. Interpolation of gaps provides homogenization of the sample. Furthermore, gaps might potentially hamper any variability study due to the resulting irregularly sampled time series. For instance, the spectral window function associated with observation times introduces spurious peaks in the PSD (Deeming 1975). Also, gaps make the calculation of autocorrelation or cross-correlation functions challenging, as these functions are only properly defined for evenly sampled time series.

Pascual-Granado et al. (2018) showed that the frequency content extracted from PSD estimation might be biased when simple interpolation, like polynomial, is used for filling the gaps in time series. We therefore use the method of interpolation by autoregressive and moving average (MIARMA; Pascual-Granado et al. 2015) which is aimed at preserving the original frequency content irrespective of the spectral properties of a given signal. Because it is based on autoregressive moving average (ARMA) models, it can fit not only analytic, i.e., deterministic, components but also stochastic signals, so it is suitable for application to blazar LCs.

The MIARMA algorithm is based on a forward–backward-weighted prediction based on ARMA models fitted to the segments bracketing the gaps. The optimal order is estimated and fixed at the first step of the algorithm sequence using Akaike coefficients. ARMA models are fitted for each gap independently, that is, a local prediction is obtained. This allows weakly nonstationary signals to be interpolated, too.

To generate the estimates of errors for the missing data interpolated with MIARMA, we draw the missing errors from the empirical distribution of the uncertainties at hand and complement the interpolated values with such obtained errors. We therefore sustain the distribution of errors and employ one such realization for subsequent computations.

2.4. Akaike and Bayesian Information Criteria

Different fits to the same data set are compared using the small-sample Akaike[8] and Bayesian Information Criteria (AIC_c and BIC), given by

$$\mathrm{AIC}_c = 2p - 2\mathcal{L} + \frac{2(p+1)(p+2)}{N-p-2} \tag{7}$$

and

$$\mathrm{BIC} = p\ln N - 2\mathcal{L}, \tag{8}$$

where $\mathcal{L}$ is the log likelihood, with N data points and p parameters (Akaike 1974; Schwarz 1978; Hurvich & Tsai 1989; Burnham & Anderson 2004). A preferred model is one that minimizes AIC_c or BIC. AIC_c is liberal and has a tendency to overfit, i.e., it might point at an overly complicated model in order to follow the data better. BIC is much more stringent and tends to underfit, i.e., it prefers models with a smaller number of parameters. Therefore, when the two IC point at different models, the truth lies somewhere in between.

What is essential in assessing the relative goodness of a fit in the AIC_c method is the difference, $\Delta_i = \mathrm{AIC}_{c,i} - \mathrm{AIC}_{c,\min}$, between the AIC_c of the ith model and the one with the minimal AIC_c. If $\Delta_i < 2$, then there is substantial support for the ith model (or the evidence against it is worth only a bare mention), and the proposition that it is a proper description is highly probable. If $2 < \Delta_i < 4$, then there is strong support for the ith model. When $4 < \Delta_i < 7$, there is considerably less support, and models with $\Delta_i > 10$ have essentially no support (Burnham & Anderson 2004).

In the case of BIC, $\Delta_i = \mathrm{BIC}_i - \mathrm{BIC}_{\min}$, and the support for the ith model (or evidence against it) also depends on the differences: if $\Delta_i < 2$, then there is substantial support for the ith model. When $2 < \Delta_i < 6$, then there is positive evidence against the ith model. If $6 < \Delta_i < 10$, the evidence is strong, and models with $\Delta_i > 10$ yield a very strong evidence against the ith model (essentially no support; Kass & Raftery 1995).

2.5. Notes on Individual Objects

We provide here basic information on the examined blazars. Their properties are summarized in Table 1.

2.5.1. Markarian 501

Markarian 501 (Mrk 501; $\alpha = 16^{\mathrm{h}}53^{\mathrm{m}}52\overset{\mathrm{s}}{.}22$, $\delta = 39°45'36\overset{''}{.}61$ in the J2000 epoch) is one of the most intensively monitored blazars from radio up to very HE (VHE; $E > 100$ GeV) γ-rays. The source was identified in X-rays based on observations conducted by the High Energy Astronomy Observatory 1 (Schwartz et al. 1978) and is one of the first HBLs detected in VHE γ-rays in the observing program of nearby BL Lacs by the Whipple Observatory ($z < 0.1$, Quinn et al. 1996). Ulrich et al. (1975) measured the spectroscopic redshift of $z = 0.034$, and showed polarimetric variability of Mrk 501. The mass of the central BH was estimated as $8.5 \times 10^8\,M_\odot$ based on the stellar velocity dispersion method (Falomo et al. 2002). Recently, Bhatta (2019) found a QPO in ∼10 yr long Fermi-LAT data, with a period of ∼330 days. Moreover, this HBL is considered as a candidate HE neutrino emitter (Righi et al. 2019).

2.5.2. Markarian 421

Markarian 421 (Mrk 421; $\alpha = 11^{\mathrm{h}}04^{\mathrm{m}}27\overset{\mathrm{s}}{.}31$, $\delta = 38°12'31\overset{''}{.}80$ in the J2000 epoch), located at $z = 0.031$ (Ulrich et al. 1975) and with the BH mass of $3.2 \times 10^8\,M_\odot$ (Falomo et al. 2002), is one of the nearest and intensively monitored HBLs in various energy bands. Its optical LC is one of the longest, starting in 1899 (Miller 1975), showing rapid flux and polarization variability (e.g., Fraija et al. 2017), and bright

[8] It is advised (Hurvich & Tsai 1989; Burnham & Anderson 2004) to employ the small-sample correction when $N/p < 40$, which is the case when fitting the PSDs herein.

Table 1
Summary of the Parameters of Individual Blazars from the Literature

Object (1)	Blazar Type (2)	z (3)	$M_{\rm BH}$ ($M_\odot$) (4)	β (5)	QPO (days) (6)	QPO Significance (7)
Mrk 501	HBL	0.034	8.5×10^8	0.99 ± 0.01[a]	$\sim$330[a]	2.58σ
Mrk 421	HBL	0.031	3.2×10^8	1.20 ± 0.11[b]	$\sim$285[c]	3.6σ
PKS 0716+714	IBL	0.310	5.6×10^8	1.11 ± 0.12[d]	$\sim$346[c]	3.9σ
PKS 2155−304	HBL	0.116	1.3×10^7	1.11 ± 0.16[d]	$\sim$610[c]	4.5σ
TXS 0506+056	IBL/HBL	0.337	3.0×10^8	...	...	...
PKS 1510−089	FSRQ	0.361	1.6×10^8	1.10 ± 0.30[e]	115[f]	2.58σ
3C 279	FSRQ	0.536	2.7×10^8	1.08 ± 0.25[e]	39 and 24[f]	3σ
B2 1520+31	FSRQ	1.489	8.3×10^8	1.15 ± 0.09[b]	$\sim$71[g]	3σ
B2 1633+38	FSRQ	1.814	2.3×10^9	1.70 ± 0.20[h]	581–646[i]	2–4σ
3C 454.3	FSRQ	0.859	8.3×10^8	1.50 ± 0.16[e]	...	...
PKS 1830−211	FSRQ	2.507	5.0×10^8	1.25 ± 0.12[j]	...	...

Notes. Columns: (1) source name; (2) detailed classification of the object; (3) redshift; (4) BH mass; (5) literature value of the power-law index β for γ-ray PSD (Fermi-LAT data); (6) QPOs in Fermi-LAT data (if "...," then no QPO search was done for this object); (7) significance of the QPO, where 1.96σ is 95%, 2.58σ is 99%, and 3σ is 99.73%.
PSD indices β and QPO periods taken from:
[a] Bhatta (2019) based on analysis of 10 yr long data.
[b] Kushwaha et al. (2017)—7 yr long data.
[c] Bhatta & Dhital (2020)—10 yr long data.
[d] Covino et al. (2019)—10 yr long data.
[e] Nakagawa & Mori (2013)—4 yr long data.
[f] Sandrinelli et al. (2016)—8 yr long data.
[g] Gupta et al. (2019)—7 yr long data.
[h] Algaba et al. (2018)—3 yr long data.
[i] Otero-Santos et al. (2020)—10 yr long data.
[j] Abdo et al. (2015)—3 yr long data.

flares in different epochs. Extreme flux variability was also detected in X-ray data (see, e.g., Kataoka & Stawarz 2016; Kapanadze et al. 2018). Mrk 421 is the first BL Lac detected in HE γ-rays by the Energetic Gamma Ray Experiment Telescope (EGRET; Lin et al. 1992) and VHE γ-rays by the Whipple Observatory (Punch et al. 1992). Moreover, it is highly variable (Błażejowski et al. 2005; Kushwaha et al. 2017) and is actively flaring across the entire electromagnetic spectrum, also showing correlations between particular energy bands, i.e., X-rays and γ-rays (Fossati et al. 2008; Aleksić et al. 2015; Ahnen et al. 2016); near-infrared (IR), optical, ultraviolet (UV), and γ-rays (Carnerero et al. 2017); and radio and γ-rays (Hovatta et al. 2015). Similarly to Mrk 501, Mrk 421 is considered a promising HE neutrino-emitter candidate (Turley et al. 2016; Organokov & Pradier 2019). No QPO was reported by Gupta et al. (2019) in 7 yr long and by Sandrinelli et al. (2017) in 8 yr long Fermi-LAT LC. Recently, Bhatta & Dhital (2020) found a QPO in $\sim$10 yr long Fermi-LAT data, with a period of $\sim$285 days.

2.5.3. PKS 0716+714

PKS 0716+714 ($\alpha = 07^{\rm h}21^{\rm m}53\overset{\rm s}{.}45$, $\delta = 71°20'36\overset{''}{.}36$, J2000 epoch) is an IBL blazar (Giommi et al. 1999) particularly known for its intraday and long-term variability at different frequencies (e.g., Villata et al. 2008; Rani et al. 2013; Liao et al. 2014) as well as short flaring events (Chandra et al. 2015). Because no emission/absorption lines were observed in IR, optical, and UV spectra, Nilsson et al. (2008) estimated its redshift to be $z = 0.31$ based on an average luminosity of the host galaxy, and Danforth et al. (2013) confirmed this value by analyzing high-resolution far-UV data. Sandrinelli et al. (2017) reported no QPOs in HE γ-rays and the optical band. On the contrary, Prokhorov & Moraghan (2017) analyzed 9 yr long Fermi-LAT data, using the generalized LSP to find a QPO with a period of $\sim$340 days, with $>5\sigma$ confidence level against white noise. Also, Li et al. (2018) analyzed the 0.1–200 GeV data of PKS 0716+714 with the Jurkevich method (Jurkevich 1971), LSP, and the red-noise spectra (REDFIT38 software; Schulz & Mudelsee 2002). A tentative QPO with a period of 344 ± 16 days was found at a significance level of $>1.96\sigma$. Recently, Bhatta & Dhital (2020) found a QPO in $\sim$10 yr long Fermi-LAT data, with a period of $\sim$346 days at a significance level of 3.9σ. Kaur et al. (2018) estimated a BH mass of $5.6 \times 10^8\,M_\odot$, while Liu et al. (2019b) give separate values for the Schwarzchild case, $2.7 \times 10^8\,M_\odot$, and the Kerr BH, $8.1 \times 10^8\,M_\odot$. Covino et al. (2019) examined γ-ray LCs of, among others, PKS 0716+714, finding a PL index $\beta = 1.11 \pm 0.12$ of its PSD.

2.5.4. PKS 2155−304

PKS 2155−304 ($\alpha = 21^{\rm h}58^{\rm m}52\overset{\rm s}{.}07$, $\delta = -30°13'32\overset{''}{.}12$, J2000 epoch), at $z = 0.116$ (Falomo et al. 1993) and a BH mass of $1.3 \times 10^7\,M_\odot$ (Liang & Liu 2003), was detected in VHE γ-rays by the University of Durham Mark 6 γ-ray telescope (Chadwick et al. 1999). Since then, comprehensive monitoring in VHE energies revealed short and bright flares as well as long- and short-term variability (e.g., Aharonian et al. 2005; Foschini et al. 2007; Ghisellini & Tavecchio 2008). Moreover, Zhang et al. (2014) discovered a QPO with a period of 317 days in 35 yr long optical data, confirmed by Sandrinelli et al. (2014) who found a period of 315 days, analyzing different data sets. Sandrinelli et al. (2014) also studied a 6 yr

long Fermi-LAT LC between 0.1 and 300 GeV, noticing ∼2 times the optical period, i.e., a periodicity peak at 650–660 days. Sandrinelli et al. (2016) confirmed the previous result, obtaining 642 days with 3σ significance, and revealed two more peaks, at 61 and 52 days, with 2.58σ significance. Hints of a possible QPO with a period of ∼670–700 days were seen in a 5.5 yr long Fermi-LAT LC as well (H.E.S.S. Collaboration et al. 2017). Subsequently, Zhang et al. (2017a) reported a periodicity of ∼635 days with a 4.9σ significance, based on an 8 yr long Fermi-LAT LC, while Bhatta & Dhital (2020) found a period of ∼610 days with a 4.5σ significance, using ∼10 yr long Fermi-LAT data. Most recently, Peñil et al. (2020) analyzed a 9 yr long Fermi-LAT LC and identified, with several methods, a QPO with a period of ∼620 days, on a significance level of 2σ–4σ. PKS 2155−304 is also the first AGN with a QPO detection in optical polarization, showing two peaks, at 13 and 30 minutes (Pekeur et al. 2016). Covino et al. (2019) found a PL index of $\beta = 1.11 \pm 0.16$ of its PSD.

2.5.5. TXS 0506+056

TXS 0506+056 ($\alpha = 05^{\rm h}09^{\rm m}25\overset{\rm s}{.}96$, $\delta = 05°41'35\overset{''}{.}33$, J2000 epoch), located at $z = 0.3365$ (Paiano et al. 2018), was first detected in radio at 5 GHz by the Arecibo telescope (Lawrence et al. 1983), and then in HE γ-rays by EGRET (Lamb & Macomb 1997) and Fermi-LAT (Abdo et al. 2010b). TXS 0506+056 is a bright BL Lac, occupying the transition region between IBLs and HBLs, considered lately to be a counterpart of the IceCube neutrino event (e.g., Ansoldi et al. 2018; IceCube Collaboration et al. 2018; Padovani et al. 2018; Halzen et al. 2019). Its BH mass was recently estimated to be $3.0 \times 10^8\,M_\odot$ (Padovani et al. 2019).

2.5.6. PKS 1510−089

PKS 1510−089 ($\alpha = 15^{\rm h}12^{\rm m}50\overset{\rm s}{.}53$, $\delta = -09°05'59\overset{''}{.}83$, J2000 epoch) is a bright and highly variable FSRQ located at $z = 0.361$ (Burbidge & Kinman 1966; Thompson et al. 1990), with a central BH mass of $1.6 \times 10^8\,M_\odot$ (Liang & Liu 2003). The blazar was detected in HE γ-rays by EGRET (Hartman et al. 1999), and then in the VHE regime by the High Energy Stereoscopic System (H.E.S.S. Collaboration et al. 2013). Several multiwavelength observational campaigns were conducted to study its variability and to search for correlations between different energy bands. Abdo et al. (2010a) reported a complex variability in γ-rays and optical/UV bands, showing a strong correlation of γ-rays and optical fluxes. Foschini et al. (2013) reported the shortest flux variability ever detected in HE, with the timescale of ∼20 minutes. Aleksić et al. (2014) concluded that HE and VHE emission originates in the same region, presumably situated behind the broad-line region, also finding similar variability patterns in HE and radio (at 137 MHz) emission. More recently, Sandrinelli et al. (2016) looked for QPOs in multiwavelength data of PKS 1510−089, uncovering an HE γ-ray periodicity with a period of 115 days at the 2.58σ significance level and two optical peaks at 345 and 575 days. On the other hand, neither Castignani et al. (2017) nor Gupta et al. (2019) found any QPOs in 8 yr long and 7 yr long Fermi-LAT LCs, respectively.

2.5.7. 3C 279

3C 279 ($\alpha = 12^{\rm h}56^{\rm m}11\overset{\rm s}{.}17$, $\delta = -05°47'21\overset{''}{.}53$, J2000 epoch), located at $z = 0.536$ (Burbidge & Rosenberg 1965) and with a BH mass of $2.7 \times 10^8\,M_\odot$ (Woo & Urry 2002), is one of the well-monitored and -studied FSRQs at multi-wavelength (Collmar et al. 2010; Hayashida et al. 2015; Patiño-Álvarez et al. 2018). It is one of the first blazars discovered in γ-rays by EGRET (Hartman et al. 1992) and subsequently in VHE by the Major Atmospheric Gamma-ray Imaging Cerenkov (MAGIC) telescope (MAGIC Collaboration et al. 2008). Several outbursts were monitored in a broadband spectrum, i.e., γ-ray flares in 2013 (Asano & Hayashida 2015), 2014 (Paliya et al. 2015), and 2015 (Ackermann et al. 2016). Sandrinelli et al. (2016) found QPOs with peaks at 24 and 39 days in 6 yr long Fermi-LAT data, as well as several peaks in near-IR and optical LCs. Interestingly, Qian et al. (2019) reported a possible binary SMBH system as an engine of 3C 279, examining 31 superluminal components in the jets.

2.5.8. B2 1520+31

B2 1520+31 ($\alpha = 15^{\rm h}22^{\rm m}09\overset{\rm s}{.}99$, $\delta = 31°44'14\overset{''}{.}38$, J2000 epoch) is a high-redshift ($z = 1.489$; Shaw et al. 2012) FSRQ with a BH mass of $8.3 \times 10^8\,M_\odot$ (Sbarrato et al. 2012), detected in HE γ-rays by Fermi-LAT in the three-month sky survey (Abdo et al. 2009). Kushwaha et al. (2017) noticed a log-normal distribution in 7 yr long Fermi-LAT LCs, while its PSD is typical for an accretion-powered compact source with a PL profile showing hints of a break. A QPO in a ∼4 yr long and 3 day binned Fermi-LAT LC with a period of ∼71 days was reported by Gupta et al. (2019).

2.5.9. B2 1633+38

B2 1633+38 ($\alpha = 16^{\rm h}35^{\rm m}15\overset{\rm s}{.}49$, $\delta = 38°08'04\overset{''}{.}5$, J2000 epoch) is an FSRQ-type blazar, located at $z = 1.814$ (Strittmatter et al. 1974) and with a BH mass of $2.3 \times 10^9\,M_\odot$ (Sbarrato et al. 2012), first detected in the HE range by the EGRET instrument (Compton observatory; Mattox et al. 1993). This blazar is highly variable at radio and optical frequencies (classified as an optically violent variable blazar) as well as X-ray and HE γ-ray energies (e.g., Barthel et al. 1995; Raiteri et al. 2012). Algaba et al. (2018) analyzed, among others, its γ-ray LC and fitted its PSD with a PL with $\beta = 1.7$. Recently, Otero-Santos et al. (2020) reported possible QPOs in the optical R and V bands, with periods between 657 and 705 days, at a significance of 2σ–5σ, in the polarized optical data at 654–701 days (2σ–4σ) and, finally, in a 10 yr long Fermi-LAT LC at 581–646 days (2σ–4σ).

2.5.10. 3C 454.3

3C 454.3 ($\alpha = 22^{\rm h}53^{\rm m}57\overset{\rm s}{.}75$, $\delta = 16°08'53\overset{''}{.}56$, J2000 epoch) is the brightest in γ-rays (Vercellone et al. 2011) and a relatively distant FSRQ with $z = 0.859$ (Lynds 1967), a BH mass of $8.3 \times 10^8\,M_\odot$ (Woo & Urry 2002), and known for its high variability in multiwavelength as well as prominent flaring activity (e.g., Gupta et al. 2017; Kushwaha et al. 2017). The 2010 outburst, which made the blazar the brightest in HE in the sky (Abdo et al. 2011), was particularly well studied. Sasada et al. (2014) analyzed mid-IR and optical data, spanning over 4 yr, finding a large-amplitude outburst lasting months and rapid flares appearing and disappearing within a few days. Diltz & Böttcher (2016) modeled the broadband SED generated with data gathered during the 2010 flare, concluding that the one-zone lepto-hadronic model provides merely poor fits. Interestingly, Weaver et al. (2019) discovered a QPO with a

characteristic period of 36 minutes by analyzing *R*-band optical data of the 2016 flare.

2.5.11. PKS 1830–211

PKS 1830−211 ($\alpha = 18^{\rm h}33^{\rm m}39\overset{\rm s}{.}92$, $\delta = -21°03'39\overset{''}{.}9$, J2000 epoch) is a well-known distant gravitationally lensed quasar (Pramesh Rao & Subrahmanyan 1988; Subrahmanyan et al. 1990), with $z = 2.507$ (Lidman et al. 1999) and a BH mass of $5.0 \times 10^8\,M_\odot$ (Nair et al. 2005); the lens is a spiral galaxy located at $z = 0.89$ (Wiklind & Combes 1996). Jauncey et al. (1991) reported a surprisingly bright radio Einstein ring, which is several times brighter than other phenomena of this type. PKS 1830−211 is the brightest high-redshift γ-ray blazar detected by Fermi-LAT with a large flaring activity in HE γ-rays (Abdo et al. 2015). Moreover, this blazar seems to be variable in both submillimeter flux density and linear polarimetry (Marti-Vidal & Muller 2019). Because PKS 1830−211 is a distant γ-ray emitter, it can be used to study extragalactic background light and to examine cosmological models.

3. Methods

We denote the values of a time series by x. For discrete data, we use the notation x_k, $k \in \{1, \ldots, N\}$, measured at times t_k, and Δx_k denotes the measurement uncertainties. For a continuous process, we use $x(t)$ or x_t for simplicity, $t \in \mathbb{R}$. Obviously, $x_k(t_k)$ is a sampled set of observations of the underlying $x(t)$.

3.1. Fourier Spectra

The discrete Fourier transform (DFT) of the set $\{x_k\}_{k=1}^N$ is

$$\mathrm{DFT}(f_s) = \sum_{k=1}^{N} x_k \exp\left[-2\pi i f_s t_k\right] \tag{9}$$

for a discrete set of frequencies $f_s = \frac{s-1}{N\delta t}$, $s \in \{1, \ldots, N\}$, where $\delta t = t_{k+1} - t_k$ is a constant time interval between consecutive observations, its inverse being the sampling rate, $\mathrm{SR} = 1/\delta t$. The first point, $\mathrm{DFT}(f_{s=1}) = \mathrm{DFT}(0) = \sum_{k=1}^N x_k$, is the zero-frequency value (so-called DC value). Subtracting from the time series its mean, $\bar{x}$, removes this spurious component from the DFT and the subsequent PSD. The Nyquist frequency $f_{\rm Nyq} = 1/(2\delta t)$ is half the SR, i.e., it corresponds to twice the sampling interval and denotes the maximal frequency (minimal period) that can be meaningfully inferred from the observed time series.

The Fourier PSD is defined herein to be

$$P(f_s) = \frac{2\delta t}{N} |\mathrm{DFT}(f_s)|^2. \tag{10}$$

For the range $f_s \in [f_{\rm Nyq}, 2 \cdot f_{\rm Nyq}]$ it is a symmetric reflection of the PSD in $f_s \in [0, f_{\rm Nyq}]$, hence only half of the N frequencies are physically meaningful.

The Poisson noise level, coming from the statistical noise due to uncertainties in the measurements, Δx_k, is given by

$$P_{\rm Poisson} = \frac{2\delta t}{N} \sum_{k=1}^{N} \Delta x_k^2. \tag{11}$$

For fitting a PL in log–log space,

$$P(f) = \frac{P_{\rm norm}}{f^\beta}, \tag{12}$$

or a PL plus Poisson noise (PLC) power spectrum,

$$P(f) = \frac{P_{\rm norm}}{f^\beta} + C, \tag{13}$$

where $P_{\rm norm}$ is a normalizing constant, and C is an estimate of $P_{\rm Poisson}$, one needs to take into account two things. First, the evenly spaced frequencies f_s are no longer uniformly spaced when logarithmized, i.e., their density is greatly increased at higher f_s values (where the Poisson noise can be expected to be significant). A straightforward least-squares fitting would then rely mostly on points clustered in one region of the $\log f_s$ values. To circumvent this, binning is applied. The values of $\log f_s$ are binned into equal-width bins, with at least two points in a bin, and the representative frequencies are computed as the geometric mean in each bin. The PSD value in a bin is taken as the arithmetic mean of the logarithms of the PSD (Papadakis & Lawrence 1993; Isobe et al. 2015). Second, the logarithm of a PSD is biased in the sense that the expected value of the logarithmic PSD is shifted upwards by $\gamma/\ln(10) \approx 0.250682$ from the computed PSD, where γ is the Euler–Mascheroni constant (Vaughan 2005). Hence, the bias-corrected logarithmic PSD is obtained by subtracting 0.250682 from the raw logarithmic PSD.

3.2. Lomb–Scargle Periodogram

The LSP (Lomb 1976; Scargle 1982; Press & Rybicki 1989; VanderPlas 2018) for arbitrarily spaced data (i.e., unevenly sampled time series) is computed as

$$P_{LS}(\omega) = \frac{1}{2\sigma^2}\left[\frac{\left(\sum_{k=1}^N (x_k - \bar{x})\cos[\omega(t_k - \tau)]\right)^2}{\sum_{k=1}^N \cos^2[\omega(t_k - \tau)]} + \frac{\left(\sum_{k=1}^N (x_k - \bar{x})\sin[\omega(t_k - \tau)]\right)^2}{\sum_{k=1}^N \sin^2[\omega(t_k - \tau)]}\right], \tag{14}$$

where $\omega = 2\pi f$ is the angular frequency, $\tau \equiv \tau(\omega)$ is

$$\tau(\omega) = \frac{1}{2\omega}\arctan\left[\frac{\sum_{k=1}^N \sin(2\omega t_k)}{\sum_{k=1}^N \cos(2\omega t_k)}\right], \tag{15}$$

and $\bar{x}$ and σ^2 are the sample mean and variance.

The lower limit for the sampled frequencies is $f_{\rm min} = 1/(t_{\rm max} - t_{\rm min})$, corresponding to the length of the time series. The upper limit, $f_{\rm max}$, would be the Nyquist frequency, the same as in the Fourier spectrum (Section 3.1), if the data were uniformly sampled. For unevenly spaced data, the common choices for a pseudo-Nyquist frequency are somewhat arbitrary (VanderPlas 2018). The result of Eyer & Bartholdi (1999) gives a proper and meaningful way to assess the high-end frequency limit in the case of nonuniform sampling: $f_{\rm Nyq} = 1/2p$, where p is the smallest value that satisfies $t_k = t_1 + n_k p$, $n_k \in \mathbb{N}$. Such p is a kind of the greatest common

divisor of the set $\{t_k - t_1\}_{k=2}^{N}$. This, however, may not exist if t_k are irrational; strictly speaking, p is then equal to zero, hence $f_{\rm Nyq} = \infty$. In reality, the Nyquist frequency is limited by the temporal precision of the measurements, giving a large, but not infinite, value.

The frequency grid should not be too sparse because it would then miss spectral structures between the grid points. On the other hand, a too-fine grid will require a longer computation time with no value added. A general approach is to choose a grid so that every peak in the periodogram is sampled $n_0 = 5$–10 times (VanderPlas 2018). This leads to the total number of sampling frequencies being

$$N_P = n_0 \frac{f_{\rm max}}{f_{\rm min}}. \tag{16}$$

We employ $n_0 = 10$ hereinafter.

Finally, to adjust the Poisson noise level from Equation (11) to the normalization that is used in Equation (14), a conversion is employed:

$$P_{\rm Poisson,LS} = \frac{1}{2\sigma^2}\frac{1}{2\delta t} P_{\rm Poisson}. \tag{17}$$

3.3. Wavelet Scalogram

3.3.1. Wavelets

A wavelet $\psi(t)$ (Farge 1992; Flandrin 1992; Wojtaszczyk 1997; Torrence & Compo 1998; Addison 2002; Mallat 2009; Martínez et al. 2009; Kirby & Swain 2013) is a short, temporally and spectrally localized oscillation with finite energy (i.e., normalized in the L^2 norm, $\langle \psi(t), \psi(t)\rangle = 1$) and zero mean,[9] $\langle \psi(t)\rangle = 0$. A mother wavelet generates the dictionary, or child wavelets, forming the basis:

$$\psi_{s,l}(t) = \frac{1}{\sqrt{s}}\psi\left(\frac{t-l}{s}\right). \tag{18}$$

The term $l \in \mathbb{R}$ refers to translation, hence location of the wavelet, and $s \in \mathbb{R}_+$ is the scale, corresponding to dilation. The factor $1/\sqrt{s}$ ensures energy normalization across different scales, $\langle \psi_{s,l}(t), \psi_{s,l}(t)\rangle = 1$. A CWT allows the signal $x(t)$ to be decomposed into a combination of $\psi_{s,l}(t)$ using the wavelet coefficients

$$W(s, l) = \langle x(t), \psi_{s,l}(t)\rangle = \int_t x(t)\psi^*_{s,l}(t)dt. \tag{19}$$

The signal can therefore be reconstructed as

$$x(t) = \sum_{s,l} W(s, l)\psi_{s,l}(t). \tag{20}$$

[9] The zero-mean criterion is equivalent to the admissibility criterion:

$$C_g = \int_0^\infty \frac{|\hat{\psi}(f)|^2}{f} df < \infty,$$

where $\hat{\psi}(f)$ is the Fourier transform of the mother wavelet. It follows that $\hat{\psi}(0) = 0$, otherwise the above integral would blow up. C_g is called the admissibility constant. For the Morlet wavelet, the admissibility criterion is satisfied for $\omega > 5$.

A discrete wavelet transform (DWT) is a CWT computed for a discrete set of translations and scales:

$$d_{j,k} = \langle x(t), \psi_{j,k}(t)\rangle = \int_t x(t)\psi_{j,k}(t)dt \tag{21}$$

with child wavelets

$$\psi_{j,k}(t) = \frac{1}{2^{j/2}}\psi\left(\frac{t}{2^j} - k\right), \tag{22}$$

where $j \in \mathbb{Z}$ represents the octave (timescale) and $k \in \mathbb{Z}$ the position of the wavelet. The octaves are divided into an integer number of voices. By comparison with Equation (18), 2^j corresponds to the scale s and $k \cdot 2^j$ to the location l. For a discrete realization of a time series, $\{x_t\}$, the CWT and DWT can be computed by changing the integration to summation in Equations (19) and (21).

Among the many wavelet families, for CWT we use throughout this work the complex-valued Morlet wavelet (Figure 5(a)),

$$\psi_{\rm Morlet}(t) = \frac{1}{\pi^{1/4}}\left[\exp(i\omega t) - \exp\left(-\frac{\omega^2}{2}\right)\right] \times \exp\left(-\frac{t^2}{2}\right), \tag{23}$$

with $\omega = 5.5$, so that the admissibility criterion is satisfied. For the DWT, we employ the Haar wavelet (Figure 5(b)),

$$\psi_{\rm Haar}(t) = \begin{cases} 1 & 0 \leqslant t < \frac{1}{2} \\ -1 & \frac{1}{2} \leqslant t < 1 \\ 0 & \text{otherwise} \end{cases}. \tag{24}$$

3.3.2. Scalogram

The scalogram—a wavelet periodogram—is a two-dimensional, time–frequency (l, s) representation of the energy-density map,

$$P_{\rm wav}(s, l) = |W(s, l)|^2, \tag{25}$$

i.e., it shows the temporal localization of a (possibly transient) frequency present in the signal $x(t)$. This is significantly different from the Fourier spectra or LSPs, where only global components are investigated, without their time evolution. Such a global wavelet periodogram can be obtained as an average over the observed period for each scale s:

$$P_{\rm wav}(s) = \frac{1}{N}\sum_{l=1}^{N}|W(s, l)|^2. \tag{26}$$

3.3.3. Cone of Influence

Because of the finiteness of $\{x_k\}$ and due to the underlying assumption of a cyclic data set, near the end points ($l = 1$ and $l = N$) the scalogram is prone to errors. This erroneous zone is called the cone of influence (COI), and its border is obtained as the distance from the highest peak of the autocorrelation of the wavelet's power to the point where it decays to e^{-1} of the peak's height. For the Morlet wavelet, the border of the COI extends $s\sqrt{2} \approx 1.41\,s$ from the edges of the scalogram (Torrence & Compo 1998), for each scale s. A more

conservative choice, employed hereinafter, is to extend the COI to $3s$.

3.3.4. Irregularly Sampled Time Series

The above considerations lead to a straightforward implementation in the case of regularly sampled time series. For data with irregular sampling, such as the LCs herein, we employ the Welch overlapping segment averaging (WOSA) method, implemented in the package WAVEPAL[10] (Lenoir & Crucifix 2018a, 2018b). WOSA consists of segmenting the time series into overlapping segments, tapering them, taking the periodogram on each segment, and taking the average of all the periodograms. The COI is precisely defined as those $\{l, s\}$ that fulfill

$$|l - t_m| \leqslant 3\omega s, \tag{27}$$

where $m = \min$ and $m = \max$. The maximum scale that can be probed is therefore

$$s_{\max} = \frac{t_{\max} - t_{\min}}{6\omega}. \tag{28}$$

The gaps in the data obviously prevent any inference within them, and therefore, they constitute the Shannon–Nyquist exclusion zone (SNEZ), excluded due to local aliasing issues. The SNEZ is computed based on the local Shannon–Nyquist theorem. See Lenoir & Crucifix (2018a, 2018b) for mathematical details of the whole procedure.

To test the significance of the detected features in the scalograms, they are tested against a CARMA stochastic model (see Section 3.5). This is a more general family of noise than the easily tested white noise or the commonly considered colored noise (Uttley et al. 2002). We employ the significance testing to search for QPOs at the level of at least 3σ (99.73% confidence level).

3.4. ARMA Processes

The ARMA process of order (p, q), denoted ARMA(p, q), is a (preferably stationary) stochastic process obeying the difference equation (Scargle 1981; Box et al. 1994; Brockwell & Davis 1996, 2002; Moreno et al. 2019)

$$x_t = c + \sum_{k=1}^{p} \varphi_k x_{t-k} + \sum_{k=1}^{q} \theta_k \varepsilon_{t-k} + \varepsilon_t, \tag{29}$$

where ε_t denotes white noise, $\varepsilon_t \sim \mathcal{N}(0, \sigma^2)$, φ_k are the autoregression (AR), and θ_k are the moving average (MA) coefficients. The current value, x_t, of an ARMA(p, q) process depends on a linear combination of p previous ones, $\{x_{t-k}\}_{k=1}^{p}$, a linear combination of q previous noise terms, $\{\varepsilon_{t-k}\}_{k=1}^{q}$, and the current noise term ε_t. When $q = 0$, an ARMA(p, q) becomes an autoregressive AR(p) process of order p, with no dependence on previous noise terms ε_{t-k}, except for the current one, ε_t. Likewise, when $p = 0$, ARMA(p, q) is a moving average MA(q) process with no dependence on the previous x_{t-k} values at all.

A convenient formulation of an ARMA(p, q) is through the backshift operator B, which acts like

$$By_t = y_{t-1}, \tag{30}$$

[10] https://github.com/guillaumelenoir/WAVEPAL

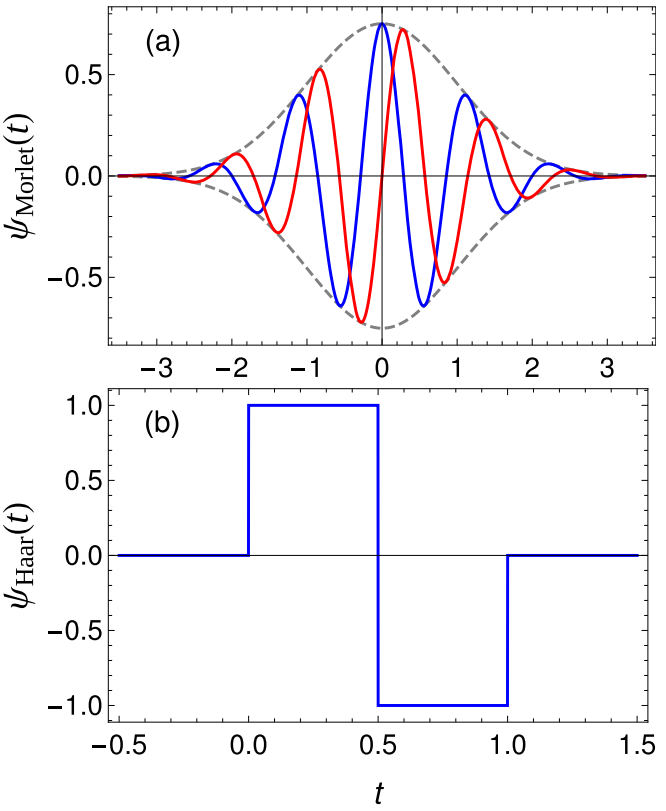

Figure 5. (a) The real (blue) and imaginary (red) parts of the Morlet wavelet from Equation (23) and its Gaussian envelope (gray dashed). (b) The Haar wavelet from Equation (24).

so that $B^k y_t = y_{t-k}$, giving a concise form of Equation (29) as

$$\varphi(B)x_t = c + \theta(B)\varepsilon_t, \tag{31}$$

with polynomial operators

$$\varphi(B) = 1 - \sum_{k=1}^{p} \varphi_k B^k,$$
$$\theta(B) = 1 + \sum_{k=1}^{q} \theta_k B^k. \tag{32}$$

With these definitions, the constraint on the φ_k coefficients for an ARMA(p, q) process to be stationary is $\varphi(z) \neq 0\ \forall z \in \mathbb{C} \wedge |z| \leqslant 1$ (i.e., the roots of the autoregression polynomial lie outside the unit circle).

A second-order stationary process can be written as a linear process (after subtracting the deterministic component):

$$x_t = \sum_{k=-\infty}^{\infty} \psi_k \varepsilon_{t-k} \equiv \psi(B)\varepsilon_t, \tag{33}$$

where

$$\psi(B) = \sum_{k=-\infty}^{\infty} \psi_k B^k \tag{34}$$

and $\sum_{k=-\infty}^{\infty} |\psi_k| < \infty$. The identity $\psi(z) = \theta(z)/\varphi(z)$ links the coefficients φ_k, θ_k, and ψ_k. If $\psi_k = 0$ for $j < 0$, Equation (33) is an MA(∞) process.

The constant c is related to the mean μ of the ARMA process values $\{x_t\}$ via

$$\mu = \frac{c}{1 - \sum_{k=1}^{p} \varphi_k}. \tag{35}$$

The autocovariances γ_j can be obtained by solving the system of recurrent equations:

$$\begin{aligned}\gamma_0 &= \sum_{k=1}^{p} \varphi_k \gamma_k + \sigma^2 \left(1 - \sum_{k=1}^{q} \theta_k \psi_k\right),\\ \gamma_j &= \sum_{k=1}^{p} \varphi_j \gamma_{k-j} - \sigma^2 \sum_{k=0}^{q} \theta_{j-k} \psi_k,\end{aligned} \tag{36}$$

for $j \in \{1, \ldots, p\}$ and with $\theta_0 = -1$. The variance of $\{x_t\}$ is therefore γ_0.

The PSD of an ARMA(p, q) process is

$$P_{\mathrm{ARMA}}(\lambda) = \frac{\sigma^2}{2\pi} \frac{|\theta(e^{-i\lambda})|^2}{|\varphi(e^{-i\lambda})|^2}, \quad -\pi \leqslant \lambda \leqslant \pi, \tag{37}$$

with λ (continuous) corresponding in range to the Fourier frequencies (Brockwell & Davis 1996, 2002), $-\pi < f_j \equiv 2\pi j/N \leqslant \pi$, $j \in \mathbb{Z}$, and the PSDs for the AR(p) and MA(q) process are obtained by setting $\theta(z) = 1$ or $\varphi(z) = 1$ (i.e., $q = 0$ or $p = 0$), respectively.

A further generalization of an ARMA(p, q) process is described in Section 3.6.5. Fittings are routinely performed by the method of moments or maximum likelihood estimation (Beran 1994; Box et al. 1994; Brockwell & Davis 1996, 2002; Beran et al. 2013).

3.5. CARMA Modeling

CARMA (Brockwell & Davis 2002; Moreno et al. 2019) is a stochastic process that obeys the stochastic differential equation:

$$\begin{aligned}&\frac{d^p x(t)}{dt^p} + \alpha_{p-1} \frac{d^{p-1} x(t)}{dt^{p-1}} + \ldots + \alpha_0 x(t)\\ &= \beta_q \frac{d^q \varepsilon(t)}{dt^q} + \beta_{q-1} \frac{d^{q-1} \varepsilon(t)}{dt^{q-1}} + \ldots + \varepsilon(t),\end{aligned} \tag{38}$$

with $\alpha_p = 1$ and $\beta_0 = 1$. Stationarity is ensured if $p > q$. The PSD of a CARMA(p, q) is

$$P_{\mathrm{CARMA}}(\lambda) = \sigma^2 \frac{\left| \sum_{j=0}^{q} \beta_j (2\pi i \lambda)^j \right|^2}{\left| \sum_{k=0}^{p} \alpha_k (2\pi i \lambda)^k \right|^2}, \quad -\pi \leqslant \lambda \leqslant \pi. \tag{39}$$

When CARMA(1, 0) is considered, i.e., the OU process (Koen 2005; Kelly et al. 2009, 2011; Sobolewska et al. 2014), the PSD simplifies to

$$P_{\mathrm{OU}}(\lambda) = \frac{\sigma^2}{\alpha_0^2 + (2\pi\lambda)^2}, \quad -\pi \leqslant \lambda \leqslant \pi, \tag{40}$$

i.e., it is a Lorentzian centered at zero and with a break frequency at $\alpha_0/(2\pi)$. The general PSD from Equation (39) can be expressed as a weighted sum of such Lorentzian functions, hence it allows variability in different timescales to be flexibly modeled, QPOs to be detected, and variability-based classification of astrophysical sources to be determined. The PSD can allow for several breaks, corresponding to a number of zero-centered Lorentzians, whose widths are the locations of the breaks. Non-zero-centered Lorentzians are used to model QPOs. CARMA accounts for irregular sampling and error measurements, and fits an LC in the time domain using the publicly available[11] Markov Chain Monte Carlo (MCMC) sampler developed by Kelly et al. (2014). In short, Equation (38) is translated into a state space representation:

$$\begin{cases} x(t) = \boldsymbol{b}\boldsymbol{y}(t) + \delta(t) \\ d\boldsymbol{y}(t) = A\boldsymbol{y}(t)dt + \boldsymbol{e}dW(t) \end{cases}, \tag{41}$$

where $W(t)$ is a Wiener process (i.e., a continuous Brownian motion, whose stochastic derivative forms the white noise $\varepsilon(t)$), $\delta(t)$ represents measurement errors, $\boldsymbol{b} = (\beta_0, \ldots, \beta_{p-1})$, $\beta_j = 0$ for $j > q$, $\boldsymbol{e} = (0, \ldots, 0, \sigma)^\top$ is p-dimensional, and the matrix A has elements $A_{p,j} = -\alpha_{j-1}$, $A_{i,i+1} = 1$, and zero otherwise. Instead of a costly maximization of the corresponding likelihood function, a Kalman filter algorithm is applied. This requires converting the solution of Equation (41),

$$\boldsymbol{y}(t) = \boldsymbol{y}_0 \exp(At) + \int_0^t \exp[A(t-u)]\boldsymbol{e}dW(u), \tag{42}$$

into that of the discrete time process evaluated at the sampled time stamps by integrating between consecutive measurements. The maximum likelihood estimation is performed with Bayesian inference via an adaptive Metropolis algorithm as the MCMC sampler (see Kelly et al. 2014 for details on the implementation).

3.6. Hurst Exponent

The Hurst exponent H (Hurst 1951; Mandelbrot & van Ness 1968; Flandrin 1992; Beran 1994; Katsev & L'Heureux 2003; Tarnopolski 2016; Knight et al. 2017) measures the statistical self-similarity of a time series $x(t)$. It is said that $x(t)$ is self-similar (or self-affine) if it satisfies

$$x(t) \doteq \lambda^{-H} x(\lambda t), \tag{43}$$

where $\lambda > 0$ and $\doteq$ denotes equality in distribution. Self-similarity is connected with long-range dependence (memory) of a process via the autocorrelation function at lag k,

$$\rho(k) = \frac{1}{2}[(k+1)^{2H} - 2k^{2H} + (k-1)^{2H}]. \tag{44}$$

$\rho(k)$ decays to zero as $k \to \infty$ so slowly that its accumulated sum does not converge (i.e., $\rho(k) \propto |k|^{-\delta}$, $0 < \delta < 1$) when $H > 0.5$, and $x(t)$ is then called a persistent process.

The meaning of H can be understood as follows: for a persistent stochastic process, if some measured quantity attains relatively high values, the system prefers to keep them high. The process is, however, probabilistic (Grech & Mazur 2004), and hence at some point the observed quantity will eventually drop to oscillate around some relatively low value. But the process still has long-term memory (being a global feature), therefore it prefers to stay at those low values until the transition occurs randomly again. In the case of $H < 0.5$, the process is antipersistent, and it possesses short-term memory, meaning that the observed values frequently switch from relatively high to relatively low (more precisely, the

[11] https://github.com/bckelly80/carma_pack

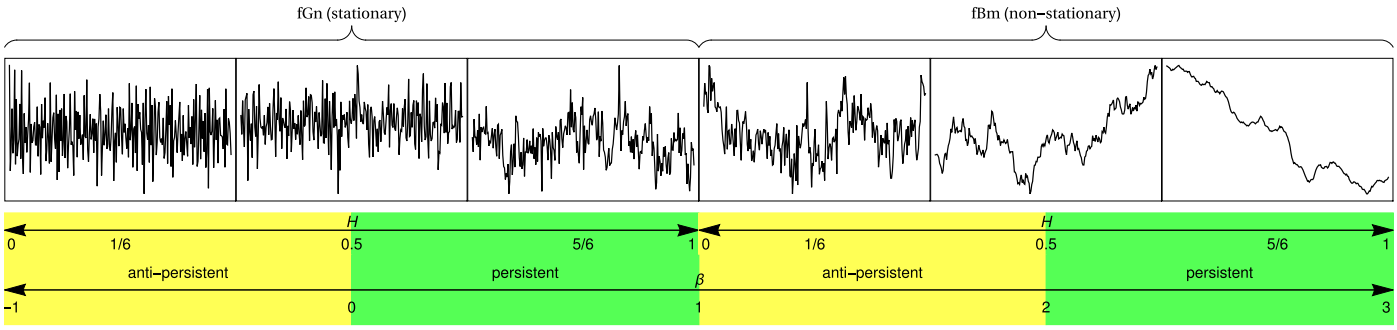

Figure 6. The discontinuity of the Hurst exponent on the border between fGn and fBm. The high-H fGn and low-H fBm, both with PL index $\beta \approx 1$, can be easily misidentified. (Figure based on Gilfriche et al. 2018).

autocorrelations $\rho(k)$ decay fast enough so that their sums converge to a finite value), and there is no preference among the increments. This is a so-called mean-reverting process.

The properties of H can be summarized as

1. $0 < H < 1$,
2. $H = 0.5$ for an uncorrelated process (white noise or Brownian motion),
3. $H > 0.5$ for a persistent (long-term memory, correlated) process, and
4. $H < 0.5$ for an antipersistent (short-term memory, anticorrelated) process.

The archetypal processes with long-range dependence are the fractional Gaussian noise (fGn, a stationary process) and fractional Brownian motion (fBm, a nonstationary process). Their PSD is of PL type, with $\beta_{\rm fBm} = 2H + 1$ and $\beta_{\rm fGn} = 2H - 1$ (Serinaldi 2010). The increments of fBm constitute an fGn. There is a discontinuity of H at the border between the two, i.e., for $\beta \approx 1$, where an fGn with $H \lesssim 1$ is visually similar to an fBm with $H \gtrsim 0$, as illustrated in Figure 6, and the two can be easily misidentified. Section 4.5 is devoted to testing the reliability of various algorithms (described in the following sections) for extraction of H and assessing regions of the (0, 1) interval where misidentification is likely to occur.

The employed algorithms for computing H rely on the PL or exponential scaling of σ versus t, where σ is a measure of the dispersion in the analyzed time series, hence the slope of the appropriate linear regression in the log–log or semi-log spaces yields the sought value of H.

3.6.1. Extraction from a PSD

A self-affine process exhibiting long-range dependence is characterized by a PL PSD (Malamud & Turcotte 1999; Gao et al. 2003; Serinaldi 2010; Tarnopolski 2016):

$$P(f) \propto \frac{1}{f^{\beta}}. \tag{45}$$

The exponent β is linearly related to the value of H via

1. $H = \frac{\beta+1}{2}$ for an fGn-like process, i.e., with $\beta \in (-1, 1)$, and
2. $H = \frac{\beta-1}{2}$ for an fBm-like process, i.e., with $\beta \in (1, 3)$.

This property makes it easy to simulate processes with a given H, but also to obtain an estimate of H for time series exhibiting a PLC spectrum from Equation (13), where the Poisson noise level C results from fluctuations present in the data, and the PL part of the PSD is considered to carry meaningful information about the examined system and the underlying stochastic process governing it. It should be pointed out that some processes, like ARMA from Section 3.4, might have PL regions in their PSDs, but associating an H with their exponent is unjustified and can lead to spurious detections. Therefore, a justification of long-range dependence in an examined system should be provided before any attempt to extract H is undertaken. A fundamental first step is to establish whether the signal is stationary (fGn like) or nonstationary (fBm like).

3.6.2. Rescaled Range Algorithm

The rescaled range algorithm (R/S) is described herein following Mandelbrot & Wallis (1969) and Suyal et al. (2009).[12] Let $\{x_k\}_{k=1}^{N}$ be an evenly spaced time series. For a temporal window w such that $w_0 \leqslant w \leqslant N$, where w_0 is the smallest window size, consider the subset of the original data set $\{X_j(t_0, w)\} = \{x_j\}_{j=t_0}^{t_0+w-1}$, where $1 \leqslant t_0 \leqslant N - w + 1$. For simplicity, one can rename the index $j \rightarrow j'$ for each subset so that j' goes from 1 to w. Then the mean of each of these subsets is

$$\overline{X}(t_0, w) = \frac{1}{w} \sum_{j'=1}^{w} X_{j'}(t_0, w). \tag{46}$$

Similarly one calculates the standard deviation S corresponding to the above means:

$$S(t_0, w) = \left[\frac{1}{w-1} \sum_{j'=1}^{w} (X_{j'}(t_0, w) - \overline{X}(t_0, w))^2 \right]^{\frac{1}{2}}. \tag{47}$$

We hereafter adopt $w_0 = 4$. The data sets are then rescaled by their mean

$$Y_{j'}(t_0, w) = X_{j'}(t_0, w) - \overline{X}(t_0, w) \tag{48}$$

and new variables y_k are defined by calculating the accumulative sum

$$y_k(t_0, w) = \sum_{j'=1}^{k} Y_{j'}(t_0, w). \tag{49}$$

The range R is defined as the difference between the maximal and minimal values in each set $\{y_k\}_{k=1}^{w}$:

$$R(t_0, w) = \max\{y_k(t_0, w)\} - \min\{y_k(t_0, w)\}. \tag{50}$$

[12] We utilize the implementation from http://demonstrations.wolfram.com/HurstExponentOfStockPrice/.

Finally, the rescaled range R/S is defined as

$$(\mathrm{R/S})(t_0, w) = \frac{R(t_0, w)}{S(t_0, w)}. \tag{51}$$

Taking t_0 to run from 1 to $(N - w + 1)$, one calculates the R/S for each temporal window w as the average of those values:

$$(\mathrm{R/S})(w) = \frac{1}{N - w + 1} \sum_{t_0=1}^{N-w+1} (\mathrm{R/S})(t_0, w). \tag{52}$$

In practice, w is uniformly spaced on a logarithmic grid. The slope of the linear regression of $\log(\mathrm{R/S})(w)$ versus $\log w$ gives an estimate for H.

3.6.3. Detrended Fluctuation Analysis

In the detrended fluctuation analysis (DFA) algorithm (Peng et al. 1994, 1995; Hu et al. 2001; Grech & Mazur 2005), one starts with calculating the accumulative sum:

$$X_t = \sum_{k=1}^{t} (x_k - \bar{x}) \tag{53}$$

which is next partitioned into non-overlapping segments of length s each. In each segment, the corresponding part of the time series X_t is replaced with its linear fit,[13] resulting in a piecewise-linear approximation of the whole X_t, denoted by $X_{\mathrm{lin}}(t)$. The fluctuation as a function of the segment length s is defined as

$$F(s) = \left[\frac{1}{N} \sum_{t=1}^{N} (X_t - X_{\mathrm{lin}}(t))^2 \right]^{\frac{1}{2}}. \tag{54}$$

The slope α of the linear regression of $\log F(s)$ versus $\log s$ is an estimate for H: $H = \alpha$ if $\alpha \in (0, 1)$, i.e., for fGn-like signals, and $H = \alpha - 1$ if $\alpha \in (1, 2)$, i.e., for fBm-like signals.

3.6.4. Wavelets

AWC—We utilize the averaged wavelet coefficient (AWC) method of Simonsen et al. (1998). It relies on the scaling in Equation (43) and employs the CWT as from Equation (19). Applying the CWT to Equation (43), one arrives at

$$W(\lambda s, \lambda l) = \lambda^{H+1/2} W(s, l). \tag{55}$$

The AWC is defined as the standard arithmetic mean over the translations l at a given scale s:

$$W(s) = \langle |W(s, l)| \rangle_l. \tag{56}$$

By a linear regression of $W(s)$ versus s in a log–log plot, H can be obtained from the slope α_{fBm} or α_{fGn} via $H = \alpha_{\mathrm{fBm}} - 1/2$ for an fBm-like process, and $H = \alpha_{\mathrm{fGn}} + 1/2$ for an fGn-like one.

DWT—H can be obtained with the DWT (Veitch & Abry 1999; MacLachlan et al. 2013; Tarnopolski 2015a, 2016; Knight et al. 2017) using, e.g., the Haar wavelet as the basis (see Section 3.3.1). The basis is obtained from a mother wavelet according to Equation (18). The relation between the variance of the wavelet transform coefficients $d_{j,k}$ from Equation (21) and the scale j can be obtained as

$$\log_2 \mathrm{var}(d_{j,k}) = \alpha \cdot j + \mathrm{const}. \tag{57}$$

The slope α is obtained by fitting a line to the linear part of the $\log_2 \mathrm{var}(d_{j,k})$ versus j. The relation between α and H is $H = \frac{\alpha - 1}{2}$ when $\alpha \in (1, 3)$ and $H = \frac{\alpha + 1}{2}$ when $\alpha \in (-1, 1)$.[14]

3.6.5. FARIMA Process

The fractional autoregressive integrated moving average process, FARIMA(p, d, q) (Granger & Joyeux 1980; Hosking 1981; Beran 1994; Brockwell & Davis 2002; Beran et al. 2013), is an ARIMA(p, d, q) process (Scargle 1981; Box et al. 1994; Brockwell & Davis 1996, 2002) with d allowed to be fractional. An ARIMA(p, d, q) process, in turn, is a generalization of an ARMA(p, q) process (see Section 3.4), in which the observed values are replaced with their consecutive differences, and this differencing operation is repeated d times.

Using the backshift operator B, an ARIMA(p, d, q) process, $d \in \mathbb{N}$, obeys the difference equation

$$\varphi(B)(1 - B)^d x_t = c + \theta(B)\varepsilon_t \tag{58}$$

with $\varphi(z)$ and $\theta(z)$ as defined in Section 3.4. This is a nonstationary process for all $d \neq 0$, and reduces to the ARMA (p, q) process when $d = 0$. If x_t is an ARIMA(p, d, q) process, then $y_t := (1 - B)^d x_t$ is an ARMA(p, q) one; hence, differencing d times removes the nonstationarity.[15]

FARIMA(p, d, q) is described by the same Equation (58) as ARIMA(p, d, q), but with the constraint on d relaxed so that d can take fractional values. To define fractional differencing, one uses the identities

$$(1 - B)^d = \sum_{k=0}^{d} \binom{d}{k} (-B)^k,$$
$$\binom{d}{k} = \frac{d!}{k!(d-k)!} = \frac{\Gamma(d+1)}{\Gamma(k+1)\Gamma(d-k+1)}. \tag{59}$$

Extending d to be any real number, formally the definition of the fractional differencing operator becomes

$$(1 - B)^d = \sum_{k=0}^{\infty} \frac{\Gamma(d+1)}{\Gamma(k+1)\Gamma(d-k+1)} (-B)^k. \tag{60}$$

For $-0.5 < d < 0.5$, FARIMA(p, d, q) is stationary; instances with $d > 0.5$ can be reduced to $|d| < 0.5$ by differencing. d is related to H via $H = d + 0.5$, hence $d \in (0, 0.5)$ are signatures of long-range dependence, i.e., a persistent process (Abry et al. 2000). Likewise, $d \in (-0.5, 0)$ signifies an antipersistent process, with short-term memory. The PSD of a FARIMA(p, d, q) process is

$$P_{\mathrm{FARIMA}}(\lambda) = \frac{\sigma^2}{2\pi} \frac{|\theta(e^{-i\lambda})|^2}{|\varphi(e^{-i\lambda})|^2} |1 - e^{-i\lambda}|^{-2d}, \tag{61}$$

where $-\pi \leqslant \lambda \leqslant \pi$ correspond to Fourier frequencies.

[13] This is the first-order DFA. Fitting a polynomial of order q constitutes the DFA of order q.

[14] Two most common instances, related to fBn and fGn; see MacLachlan et al. (2013), Tarnopolski (2016), Knight et al. (2017), and references therein for additional details.

[15] Note that $(1 - B)x_t = x_t - x_{t-1}$.

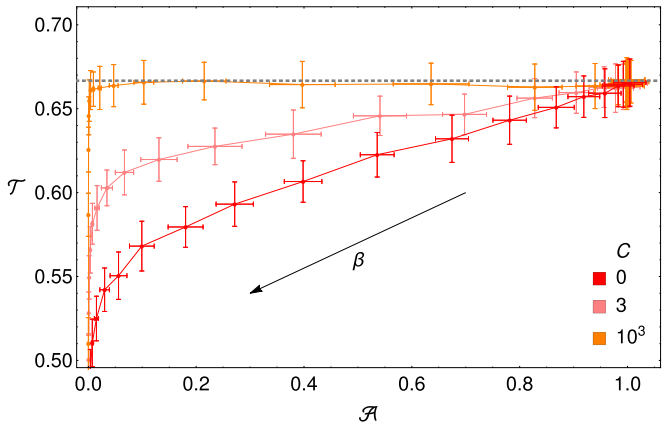

Figure 7. Locations in the $\mathcal{A}$–$\mathcal{T}$ plane of the PL plus Poisson noise spectra of the form $P(f) \propto 1/f^{\beta} + C$, with $\beta \in \{0, 0.1, \ldots, 3\}$. For each PSD, 100 realizations of the time series were generated, and the displayed points are their mean location. The error bars depict the standard deviation of $\mathcal{A}$ and $\mathcal{T}$ over these 100 realizations. The case $\beta = 0$ is pure white noise, with $(\mathcal{A}, \mathcal{T}) = (1, 2/3)$. The generic PL case ($C = 0$) is the lowest curve (red); with an increasing level of the Poisson noise, C, the curves are raised and shortened, as the white-noise component starts to dominate over the PL part.

3.7. The $\mathcal{A}$–$\mathcal{T}$ Plane

The $\mathcal{A}$–$\mathcal{T}$ plane was initially introduced to provide a fast and simple estimate of the Hurst exponent (Tarnopolski 2016). It is, however, also able to differentiate between different types of colored noise, $P(f) \propto 1/f^{\beta}$, characterized by different PL indices β (Zunino et al. 2017). In Figure 7 the locations in the $\mathcal{A}$–$\mathcal{T}$ plane of PLC spectra of the form $P(f) \propto 1/f^{\beta} + C$ are shown.

Three consecutive data points, x_{k-1}, x_k, x_{k+1}, can be arranged in six ways; in four of them, they will create a peak or a valley, i.e., a turning point (Kendall & Stuart 1973; Brockwell & Davis 1996; Tarnopolski 2016, 2019a). The probability of finding a turning point in such a subset is therefore $2/3$, and the expected value for a random data set is $\mu_T = \frac{2}{3}(N-2)$—the first and last points cannot form turning points. Let T denote the number of turning points in a time series, and $\mathcal{T} = T/N$ be their fraction in a time series. $\mathcal{T}$ is asymptotically equal to $2/3$ for a purely random time series (white noise). A process with $\mathcal{T} > 2/3$ (i.e., with raggedness exceeding that of a white noise) will be noisier than white noise. Similarly, a process with $\mathcal{T} < 2/3$ will be less ragged than white noise.

The Abbe value (von Neumann 1941a, 1941b; Williams 1941; Kendall 1971; Mowlavi 2014; Tarnopolski 2016, 2019a) is defined as

$$\mathcal{A} = \frac{\frac{1}{N-1}\sum_{i=1}^{N-1}(x_{i+1} - x_i)^2}{\frac{2}{N}\sum_{i=1}^{N}(x_i - \bar{x})^2}. \quad (62)$$

It quantifies the smoothness of a time series by comparing the sum of the squared differences between two successive measurements with the variance of the time series. It decreases to zero for time series displaying a high degree of smoothness, while the normalization factor ensures that $\mathcal{A}$ tends to unity for a purely noisy time series (more precisely, for a white-noise process).

4. Benchmark Testing

4.1. Fourier Spectra and Lomb–Scargle Periodograms

We generated 6000 time series[16] of length $N = 512$ (i.e., comparable to our actual LCs) with a time step $\delta t = 7$ d with the PLC spectrum from Equation (13), with $\beta = 1.4$ (representative value based on the blazar results; see Sections 5.1 and 5.2) and $P_{\rm norm}/C = 0.005/3.07$ (giving a clear transition from the PL part of the PSD to the white-noise region that covers a significant range of frequencies), computed their Fourier PSDs, binned them according to Section 3.1, and fitted Equation (13). Additionally, we considered the pure PL with $C = 0$ and the same $\beta = 1.4$. The distributions of the obtained indices β are displayed in Figure 8(a). In the case of a pure PL, the results are close to $\beta = 1.4$, although systematically smaller. On the other hand, only in 23.5% of simulations are the fitted β consistent with 1.4 within the standard error of the fit. For the PLC ($C \neq 0$), the retrieved indices span a significantly wider range of 0.1–2, and the typical error is five times larger than when $C = 0$. This high standard error is the reason why 42.9% indices are equal to 1.4 within error, nearly twice as many as in the pure PL case; see the bottom row of Figure 8(a). We also performed the same simulation with $N = 2048$ (in order to simulate a longer/better sampled, yet still an observationally plausible gamma-ray LC) and observed that the mode is much closer to the true value $\beta = 1.4$, and the distribution is only slightly narrower. A reasonable expectation would be that the longer the time series, the more accurate the estimation of the spectral index would be; however, the convergence appears to be slow.

The analysis was repeated with the LSPs. The results, displayed in Figure 8(b), are very similar to the DFT ones. For PLC, the distributions of β are more symmetric than in the case of the DFT approach, and due to a larger number of frequencies being tested (five times more than Fourier frequencies, according to Equation (16)), the distributions of standard errors are narrower.

Overall, we conclude that assessing the shape of the spectrum via binning and fitting—be it either the DFT or LSP—can be unreliable, especially in the PLC case, as the output is barely related to the input true index β. The situation is somewhat better when the Poisson noise component is absent, and the spectrum can be considered a pure PL. The scatter then gives a range of possible true values of β yielding the observed PSD; however, it it relatively narrow, and the resulting value might be used as a rough estimate. A systematic effect is that the fitted β is likely underestimated.

4.2. Wavelet Scalogram

To investigate the typical features of different types of processes in the time–frequency domain, the wavelet scalograms for various time series (of length $N = 500$) were generated: ARMA[17] and CARMA (both expected to have $H = 0.5$), FARIMA (See Footnote 17) with $d = \pm 0.25$, i.e., $H = 0.25$ and $H = 0.75$, fBm and fGn with $H = 0.25$ and $H = 0.75$, PLC with $\beta = 1$, i.e., borderline between high-H fGn and low-H fBm (see also Figure 6), and $\beta = 2$, i.e., corresponding to $H = 0.5$. The values $H = 0.25$ and 0.75 are

[16] Increasing the number by 1000 until we reached convergence of the distributions of interest.

[17] ARMA and FARIMA were realized with parameters generated in Section 4.3.

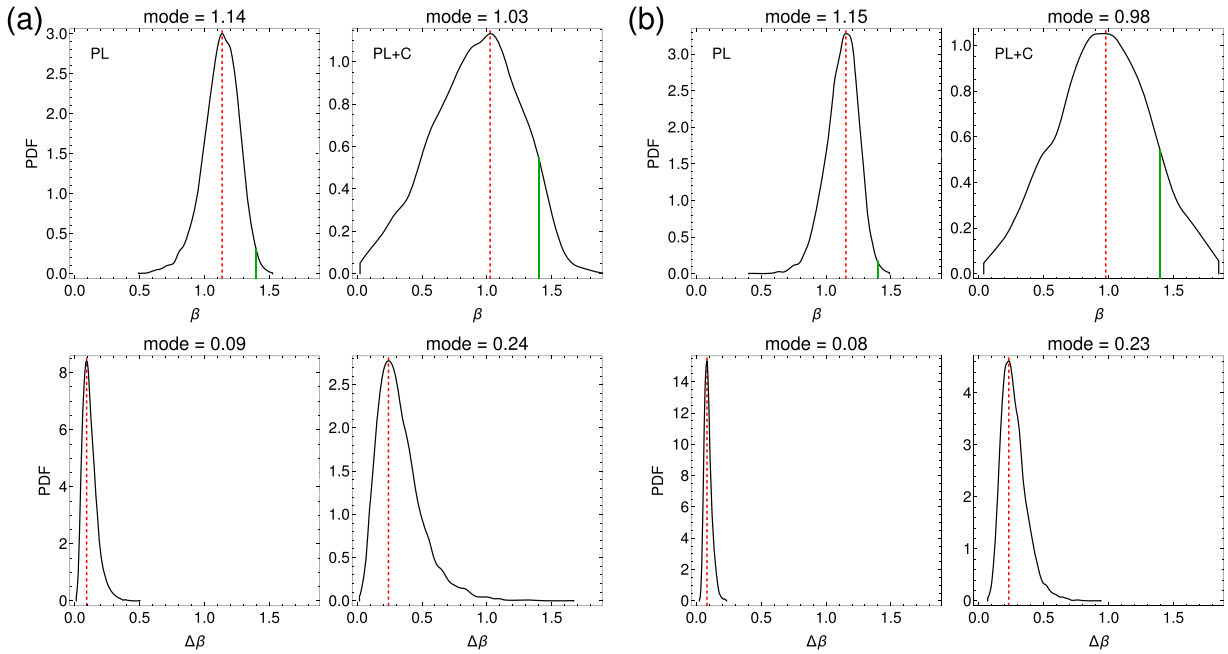

Figure 8. The distributions of the PL index β (upper row) and its error (bottom row) from fitting to (a) Fourier spectra, and (b) LSPs. Both panels display the pure PL with $N = 512$ (left column) and PLC with $N = 512$ (right column). The red dashed lines mark the modes of the distributions, and the solid green line in the upper row denotes the input value of $\beta = 1.4$.

representative for short- and long-term memory processes, respectively. For each of the 10 process types, 100 random realizations were generated. In Figure 9 we present some typical examples and their scalograms.

We observe that fBm with $H = 0.75$ is dominated by low-frequency components, i.e., short-term variations are negligible compared to the long-term behavior. In fact, in a majority of the realizations, the whole global PSD lies above the 3σ confidence level. Therefore, CARMA models that the scalograms are tested against are poor models for persistent, highly nonstationary fBm. In the case of $H = 0.25$, the frequencies are more spread out, and a QPO rarely emerges. Usually no structure at all is observed for fGn regardless of H. Likewise for PLC processes, for both $\beta = 1$ and $\beta = 2$. ARMA and FARIMA often (∼30%–40% of instances) exhibit QPO-like features. CARMA(5, 3) models were set to explicitly contain a QPO, which is nearly always detected by the scalogram, but with a very wide spread of the corresponding periods. This is due to the fact that the testing is made against a CARMA(1, 0) background, as justified by the results of CARMA fittings to the blazar LCs of interest (see Section 5.5 for details). We often record tentative QPOs at very high frequencies in the global wavelet PSD, resulting from individual spikes in the time series that contribute significantly to the total power at a given scale. Therefore, in Figure 10 we show the histograms of only QPO periods exceeding 200 days, i.e., focusing on ∼year-long periods often reported in the literature. Overall, QPOs arise in ARMA, FARIMA, and CARMA models, in whose PSDs they can be immanent, yet stochastic, features.

4.3. ARMA and FARIMA Processes

To investigate how accurate the fitting of ARMA and FARIMA processes is, we perform MC simulations in the following manner:

1. We choose the order of an ARMA(p, q) process to be (5, 3) and keep it fixed throughout. It is high enough to allow for nontrivial features in the PSDs, but low enough to be computationally efficient.
2. We randomly generate a set of (φ, θ, σ) parameters and verify that it leads to a stationary ARMA process. φ and θ are drawn from a $\mathcal{U}(-1, 1)$, and σ from a $\mathcal{U}(0.1, 1)$ distribution.
3. We simulate 150 time series of length $N = 512$ with the above set of parameters.
4. For every time series, we fit a total of 100 ARMA(p, q) processes, with $p, q \in \{0, \ldots, 9\}$. We record their AIC_c and BIC values, based on which we choose the order of the best-fitting process. As we have generated 150 time series from the same parameters, we have 150 such best-fitting orders, from which we construct a density map in the (p, q) space.
5. We choose the order that is the commonest as the most probable, and record it for further use.
6. We perform points 4 and 5, fitting a FARIMA(p, d, q) process. Additionally, we record the 150 values of d for each set of (φ, θ, σ) parameters and construct an empirical probability density of d.
7. We repeat the above procedure 250 times,[18] i.e., for 250 different sets of (φ, θ, σ) parameters.
8. We therefore obtain sets of density maps for ARMA and FARIMA fittings, and for both fitted models we have 250 such maps based on AIC_c and 250 maps based on BIC. In other words, we obtain 250 best-fitting ARMA orders based on AIC_c for each set of parameters, 250 best-fitting orders based on BIC, and similarly two sets of best-fitting orders (also 250 values each) for the fitted FARIMA processes.

[18] We verified that for 500 iterations, the results are practically the same.

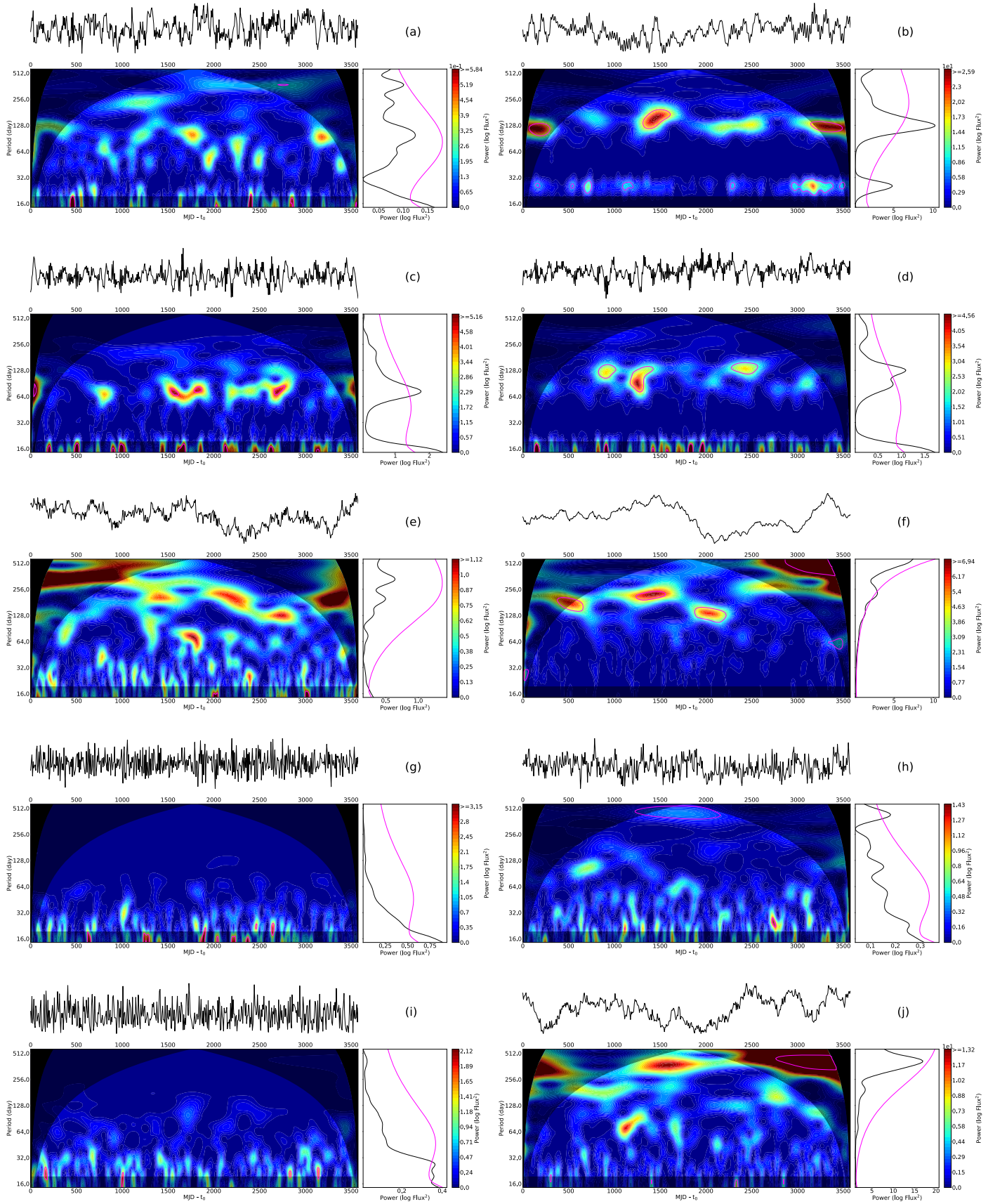

Figure 9. Exemplary wavelet scalograms and global periodograms for different stochastic models: (a) ARMA, (b) CARMA, (c) FARIMA with $H = 0.25$, (d) FARIMA with $H = 0.75$, (e) fBm with $H = 0.25$, (f) fBm with $H = 0.75$, (g) fGn with $H = 0.25$, (h) fGn with $H = 0.75$, (i) PLC corresponding to $H = 0.25$, and (j) PLC corresponding to $H = 0.75$. The magenta lines and contours denote 3σ global and local confidence levels, respectively.

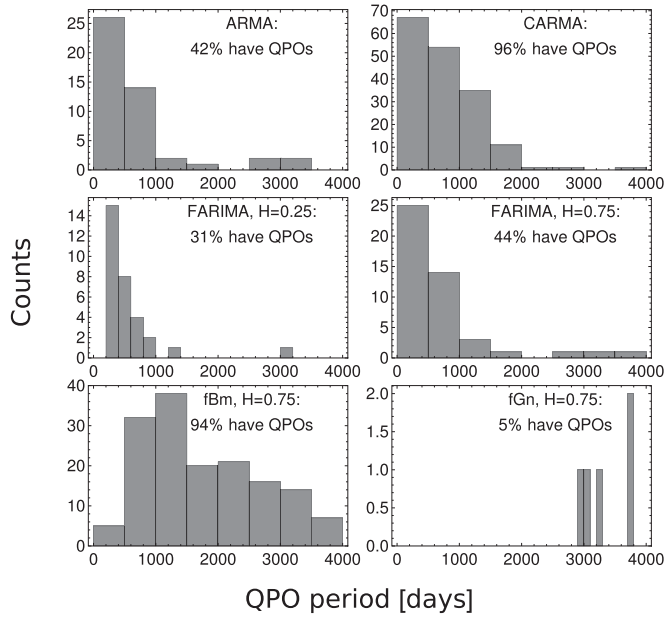

Figure 10. Distributions of QPO periods of various simulated stochastic processes, found with the wavelet scalograms. For fBm and fGn with $H = 0.25$, and PLC with $\beta = 1$ and $\beta = 2$, the fraction is 0% and hence are not displayed here.

9. From these 4 sets of 250 orders each, we construct final density maps.

We next employ exactly the same procedure, but generating the time series (to which we again fit both ARMA and FARIMA processes) from a FARIMA(5, d, 3) process. The set of input parameters (φ, θ, σ) is hence complemented with d, which we choose to be $d = 0.3$, i.e., corresponding to $H = 0.8$.

We perform such testing (for mock time series generated from both ARMA and FARIMA processes) in two instances:

1. for *clean* data—generated exactly as described above;
2. for *noisy* data—values are obtained as drawn from $\mathcal{N}(x_k, (\max\{|x_k|\}/5)^2)$ distributions, where x_k are the *clean* data points, and the fluctuations' standard deviation is set to 20% of the most extremal value.

The results for *clean* data are displayed in Figures 11(a) and (b): distributions of the best orders (p, q) and the differencing parameter d, generated from ARMA (Figure 11(a)) and FARIMA (Figure 11(b)) processes. Displayed are the distribution of all 250 × 150 recorded individual values of d and the distribution of the 250 modes $d_{\rm mode}$, obtained from the distributions of d for each set of parameters (φ, θ, σ). In most cases, the true order (5, 3) is correctly identified, although in some instances an overabundance of high-order AR(p) processes is obtained. This is particularly the case when a FARIMA model was fitted to data generated from a FARIMA process (see Figure 11(b)). The distributions of the differencing parameter d are peaked around the correct values (i.e., $d = 0$ and $d = 0.3$ for ARMA and FARIMA processes, respectively). A prominent peak, however, is observed at $d = 0.5$ (and to a smaller extent at $d = -0.5$). This is a sign of nonstationarity present in the data. We stress that all generated time series come from stationary processes, although some particular realizations might be spuriously identified as nonstationary. Based on the positions of local minima of the distributions, an outcome falling in the range $d \in (-0.4, 0.4)$ should be a safe estimate. Values outside this range could be verified by differencing the time series, i.e., examining the set of differences $\{x_k - x_{k-1}\}$ instead of the original data $\{x_k\}$. This turns a nonstationary process with a given d to one with $d - 1$. Second differences can be employed if the issue persists (although it is rare, and if occurs a careful verification of the quality of the data is strongly suggested).

A less appealing picture is painted when we consider *noisy* data (Figures 11(c) and (d)). While the distributions of d are of similar shapes to the case of *clean* data sets, the order (p, q) is systematically misidentified: a high-order AR(p) process is pointed at instead of the correct (5, 3). We see that for both *clean* and *noisy* data, the MA component of the underlying ARMA or FARIMA process is spuriously interpreted as nonstationarity or adds to the order of the resulting AR process.

The above simulations were repeated for $N = 100$ and $N = 2000$. A reasonable expectation is that the scatter in the retrieved order would be larger for shorter time series, which is indeed the case—the correct order (within Δp, $\Delta q = \pm 1$) was retrieved ∼10 times more often for $N = 2000$ than for $N = 100$. Moreover, while the retrieval of AR and MA coefficients is satisfactory, with a concentration around the $y = x$ line, where x are the input parameters and y are the fitted ones; its rms error, as expected, also considerably decreases when N increases (from ∼0.37 for $N = 100$, to ∼0.30 and ∼0.27 for $N = 512$ and $N = 2000$, respectively).

4.4. CARMA Modeling

Ryan et al. (2019) performed very detailed simulations to assess the reliability of fitting CARMA(1, 0) and (2, 1) models, focusing on retrieving the break timescales and local PL indices β. They found that CARMA(2, 1) is flexible enough to correctly recover β even from a pure PL and identifies the breaks with sufficient accuracy. They also gave a way of assessing the reality of a break: it is likely a physical feature if it is consistently detected by both lower- and higher-order CARMA fits.

Herein, we investigate the accuracy of fitting a CARMA model to data in the sense of recovering the correct order (p, q). To do so, we perform MC simulations according to the following procedure:

1. We choose a relatively high order, (p, q) = (5, 3), to challenge the algorithm and for correspondence with Section 4.3.
2. We choose the values of σ, the MA parameters β_i, and the roots of the AR polynomial—in this way we ensure the simulated process to be stationary.
3. We choose the total length of the time series to be $N_{\rm tot} = 550$ points; next, we randomly discard 50 of them, creating an unevenly sampled time series with $N = 500$ observations (i.e., we end with ∼9% of the data missing).
4. We then simulate 100 realizations of the CARMA(5, 3) stochastic process with the above described characteristics. The final time series are subject to random fluctuations drawn from a truncated Gaussian distribution—these are to mimic observational errors.
5. For each realization, we perform fitting of CARMA models with $1 \leqslant p \leqslant 6$ and corresponding $0 \leqslant q < p$. For each of these (p, q) pairs, we compute the AIC_c and BIC, based on which we choose the best process order—

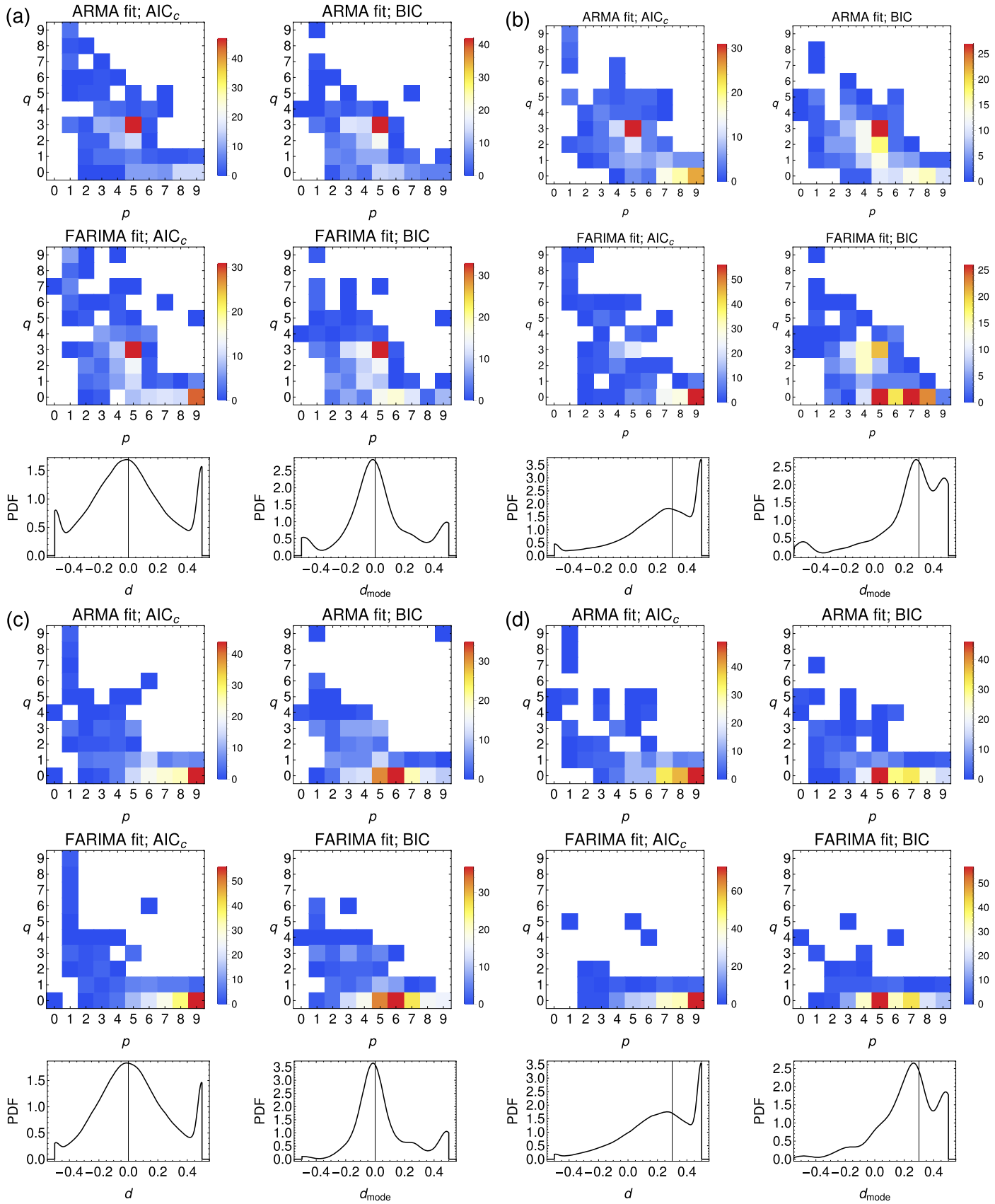

Figure 11. Benchmark results for *clean* time series generated from (a) an ARMA(5, 3) and (b) a FARIMA(5, 0.3, 3) process: density maps of the ARMA(p, q) and FARIMA(p, d, q) best-fit orders according to AIC$_c$ and BIC, and distributions of the differencing parameter d and the mode d_{mode} obtained for each set of parameters (φ, θ, σ). Vertical lines denote the underlying true value. Panels (c) and (d) are the same as (a) and (b), respectively, but for *noisy* data.

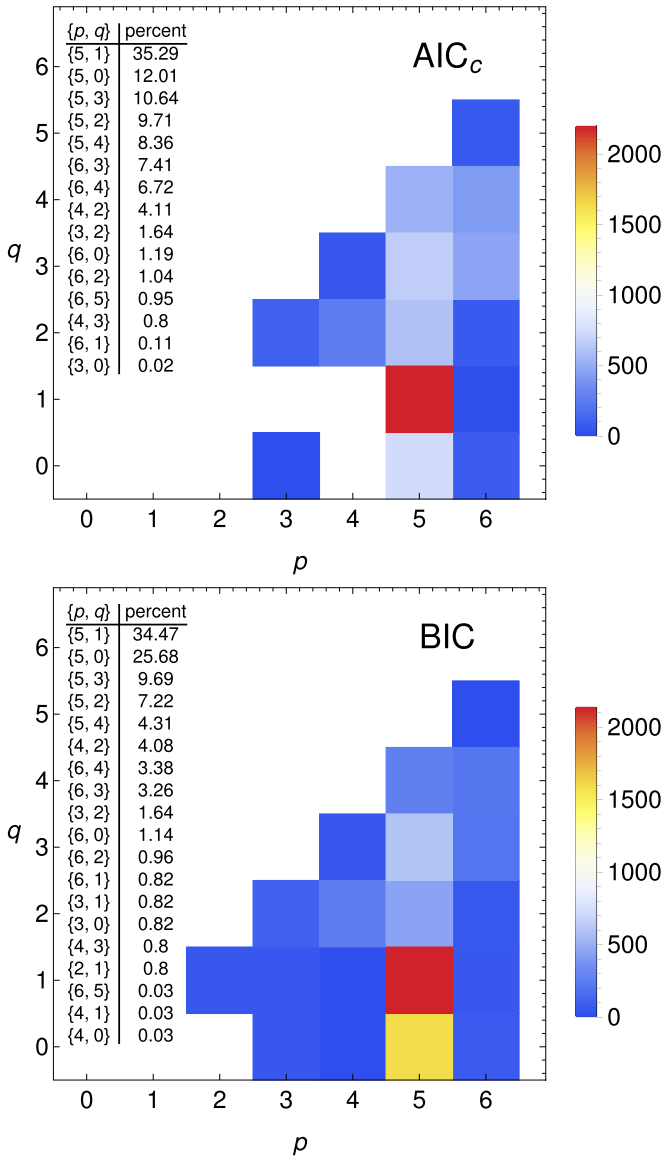

Figure 12. Density maps of CARMA(p, q) best-fit orders, fitted to 6222 realizations of the CARMA(5, 3) process, according to AIC$_c$ and BIC.

the one with the lowest AIC$_c$ or BIC. Note that all 100 realizations come from the same underlying process, so we expect to obtain (5, 3) or nearby orders in a majority of instances.

6. We build a density map of the obtained best (p, q) pairs in the p–q plane.

Using the above procedure, with realistically spaced irregular data resembling that of the Fermi-LAT LCs of blazars in our sample, we constrain the validity and reliability of the CARMA fitting. The results are displayed in Figure 12. About 35% of realizations are recognized as CARMA(5, 1) by both IC, hence the order of the MA part is underestimated. In the case of BIC, the second most common order is (5, 0) in 25%. The input order (5, 3) is returned in 10% of instances. In total, models with the correct $p = 5$ are returned in 76% and 81% of cases by employing AIC$_c$ and BIC, respectively. The lowest order (1, 0) is never returned, likewise (2, 1) with AIC$_c$ and is among the rarest pointed at by BIC. Hence, even when the fitting missed the value $p = 5$, higher orders, relatively close to the correct one, were preferred. Overall, we conclude that the procedure is indeed sufficiently reliable and robust in assessing the order of the fit, and we utilize BIC hereinafter.

4.5. Hurst Exponent

We test the H estimation algorithms from Section 3.6 on the following time series, all of length $N = 512$:

1. fBm and fGn, with $H \in \{0.05, 0.1, \ldots, 0.95\}$—1000 realizations for each H;
2. FARIMA(5, d, 3) for a few randomly chosen sets of parameters generated in Section 4.3, with $d \in \{-0.45, -0.4, \ldots, 0.45\}$—100 realizations for each d;
3. generated from a PLC spectrum, with $\beta \in \{1.1, 1.2, \ldots, 2.9\}$—1000 realizations for each β;
4. ARMA(5, 3) for all 250 sets of parameters from Section 4.3—100 realizations for each set;
5. CARMA(5, 3) for 250 sets of parameters (different than for ARMA and FARIMA)—100 realizations for each set.

The results are gathered in Figure 13. For fBm, fGn, FARIMA, and PLC—for which an input H value can be explicitly set—we show the resulting distributions as distribution charts (violin plots), i.e., for each input $H_{\rm in} \in \{0.05, 0.1, \ldots, 0.95\}$ (depicted on the horizontal axis) a distribution of the resulting output $H_{\rm out}$ is shown, spanning the vertical direction on the plots. For a nearly ideal algorithm, the distributions should be centered at $H_{\rm out} = H_{\rm in}$ and with a small dispersion. For ARMA and CARMA, which in turn are expected to give $H = 0.5$, the PDFs of all obtained H values, and for the medians of each parameter set, are plotted. For the PLC time series, we compared estimates from two approaches: one is a straightforward fit of a pure PL, and second is fitting the proper underlying PLC model. In the first approach, one should expect the outcomes to be underestimated, because the flat region of the PSD (the high-frequency Poisson noise component) will flatten the fitted PSD model and yield lower indices than the input β values. For the second approach, we expect the results to be roughly appropriate; however, from Section 4.1 we already know that the expected scatter of the calculated value of β is substantial, hence the distributions should be wide. This is indeed the case, as shown in the double panel in the first row of Figure 13. This clearly illustrates the importance of validating the presence of a PL component in the PSD of any examined time series—we stress that the algorithms for extracting H are not black boxes: the long-range dependence manifests itself through a PL PSD.

No single algorithm turns out to be best; some work well for a particular stochastic process, but fail miserably for others, e.g., fitting a PL rarely gives the correct estimate for fBm, but works quite well for fGn. The R/S method significantly overestimates H for all examined processes except for ARMA ones, and fails completely for nonstationary fBm (North & Halliwell 1994; Gilmore et al. 2002). Likewise, it overestimates for CARMA processes. DFA, DWT, and AWC give consistent and roughly correct results for processes with a nearly PL PSD (i.e., fBm, fGn, and FARIMA), but miss the correct $H = 0.5$ in the case of ARMA and CARMA. Fitting a FARIMA model and inferring the value of H from the obtained d works well for fGn, FARIMA, and ARMA, although with a big dispersion around the correct value. However, for nonstationary processes it clusters at $d = 0.5$. This issue might be resolved by differencing, however, as discussed in Section 4.3. In many cases one can observe that very high and very low H values

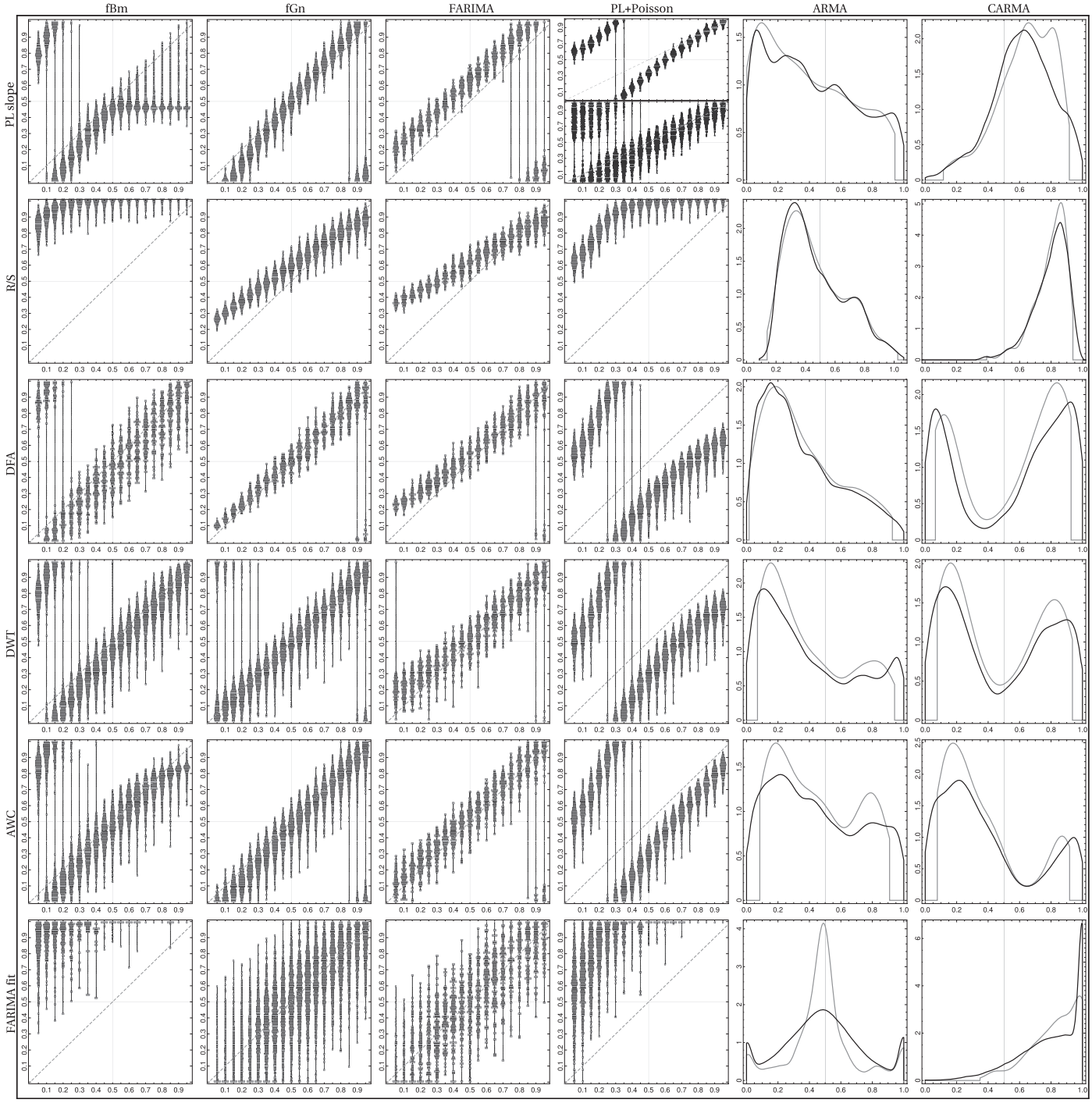

Figure 13. Results, in the form of violin plots (with [0, 1] × [0, 1] range) and PDFs (with a [0, 1] support), of the benchmark testing of various algorithms (*rows*) for estimating H, for different types of stochastic processes (columns). For the four columns from the left (i.e., labeled fBm, fGn, FARIMA, and PLC) the horizontal axis denotes the input $H_{\rm in}$ values, and the vertical axis marks the values $H_{\rm out}$ returned by the respective algorithms (labeling the rows). The diagonal dashed line denotes the equality line. The PLC model, in the PL slope approach, was evaluated in two ways: by fitting a pure PL (the upper panel in the double plot) and a PLC (lower panel). For the two columns on the right (labeled ARMA and CARMA), the plots show the PDFs of the obtained values of H; for these two processes, $H_{\rm in} = 0.5$ (marked with the vertical thin line) is expected. The black line in each plot denotes the distribution for all 250 × 100 time series, while the gray line is for the 250 medians for each parameter set.

lead to improper characterization of the time series, resulting in drastic misclassification, e.g., the DFA tends to return a very high H for processes with very low input H. Finally, the PSD of the CARMA process (Equation (39)) cannot be considered to be a PL even approximately (for the employed sets of parameters and frequency ranges of the PSDs), hence the long-term dependence is difficult to assess.

We therefore recommend simultaneously employing a few algorithms when computing H and examine the consistency of the obtained estimates. The shape of the investigated time series' PSD should be also evaluated to justify the presence of long-term dependence before any attempts to extract H are undertaken.

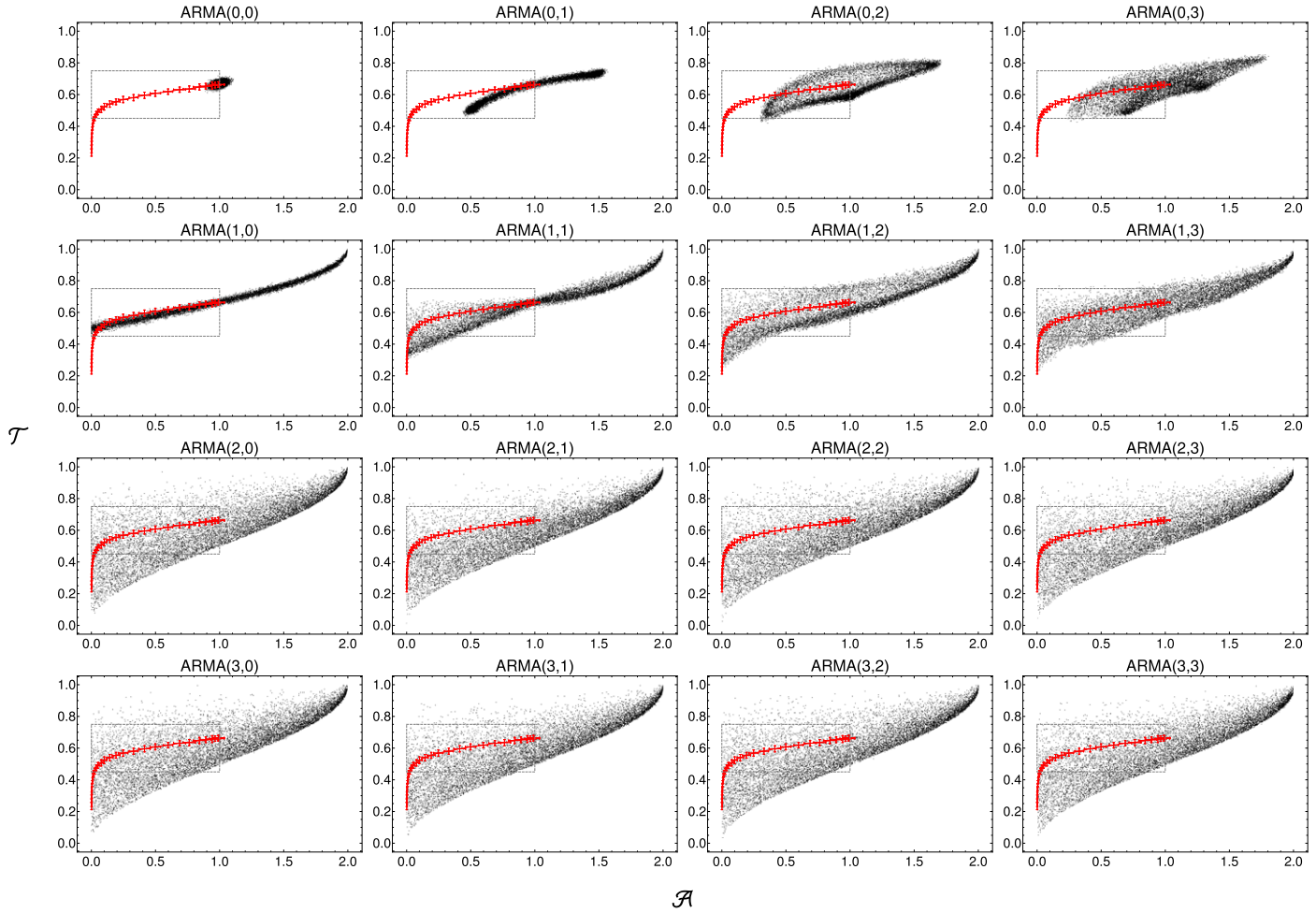

Figure 14. Stationary ARMA(p, q) processes, with $0 \leqslant p \leqslant 3$, $0 \leqslant q \leqslant 3$, in the $\mathcal{A}$–$\mathcal{T}$ plane. The gray dashed box encloses the region from Figure 7; the red line is the pure PL with $0 \leqslant \beta \leqslant 3$ (i.e., red line from Figure 7).

4.6. $\mathcal{A}$–$\mathcal{T}$ Plane

In Section 3.7, the $\mathcal{A}$–$\mathcal{T}$ plane was described, and the locations of different processes with PSDs of PLC form were displayed in Figure 7. Herein we investigate what regions of the $\mathcal{A}$–$\mathcal{T}$ plane is occupied by some other stochastic processes considered in this work.

We examine the family of ARMA(p, q) processes, with $0 \leqslant p \leqslant 3$, $0 \leqslant q \leqslant 3$. We generate 10^4 sets of AR and MA coefficients, drawn uniformly from the regions of the parameter space of the AR coefficients φ_k that ensure stationarity, with MA coefficients drawn from $\mathcal{U}(-1, 1)$, and compute the locations $(\mathcal{A}, \mathcal{T})$. Results are displayed in Figure 14. We also checked whether the regions occupied by each process change when the coefficients are drawn from a $\mathcal{U}(5, 5)$ distribution and find that the boundaries are the same.

The ARMA(0, 0) process is just white noise, so it clusters around $(\mathcal{A}, \mathcal{T}) = (1, 2/3)$. The PSD of ARMA(1, 0) is a close approximation to a PL, hence its $(\mathcal{A}, \mathcal{T})$ values closely follow the true PL line depicted in the plots, deviating only for $\beta \gtrsim 2$. We emphasize that the pure PL line follows the fBm line (Tarnopolski 2016; Zunino et al. 2017; Tarnopolski 2019a). Other ARMA models spread out into larger parts of the $(\mathcal{A}, \mathcal{T})$ plane, with less internal structure for higher orders. See Tarnopolski (2019a) for an analytic treatment of the

Table 2
PL Indices β from Fourier PSDs

Source (1)	7 days (2)	10 days (3)	14 days (4)
BL Lacs			
Mrk 501	1.96 ± 0.45[a]	2.53 ± 1.00[a]	1.73 ± 0.36[a]
Mrk 421	0.93 ± 0.12[b]	0.94 ± 0.13[b]	0.84 ± 0.17[b]
PKS 0716+714	0.97 ± 0.21[b]	0.94 ± 0.25[b]	0.94 ± 0.33[b]
PKS 2155−304	0.67 ± 0.12[b]	0.73 ± 0.10[b]	0.78 ± 0.12[b]
TXS 0506+056	2.13 ± 0.24[a]	0.91 ± 0.21[b]	1.02 ± 0.22[b]
FSRQs			
PKS 1510−089	1.03 ± 0.08[b]	1.09 ± 0.09[b]	1.06 ± 0.11[b]
3C 279	1.12 ± 0.07[b]	1.14 ± 0.07[b]	1.17 ± 0.08[b]
B2 1520+31	1.69 ± 0.06[a]	1.38 ± 0.09[b]	1.34 ± 0.10[b]
B2 1633+38	1.22 ± 0.15[b]	1.25 ± 0.18[b]	1.03 ± 0.16[b]
3C 454.3	1.68 ± 0.13[b]	1.73 ± 0.13[b]	1.79 ± 0.14[b]
PKS 1830−211	1.05 ± 0.15[b]	1.03 ± 0.16[b]	1.14 ± 0.20[b]

Notes. Columns: (1) source name; (2) β for 7 day binning; (3) β for 10 day binning; (4) β for 14 day binning.
[a] PLC.
[b] Pure PL.

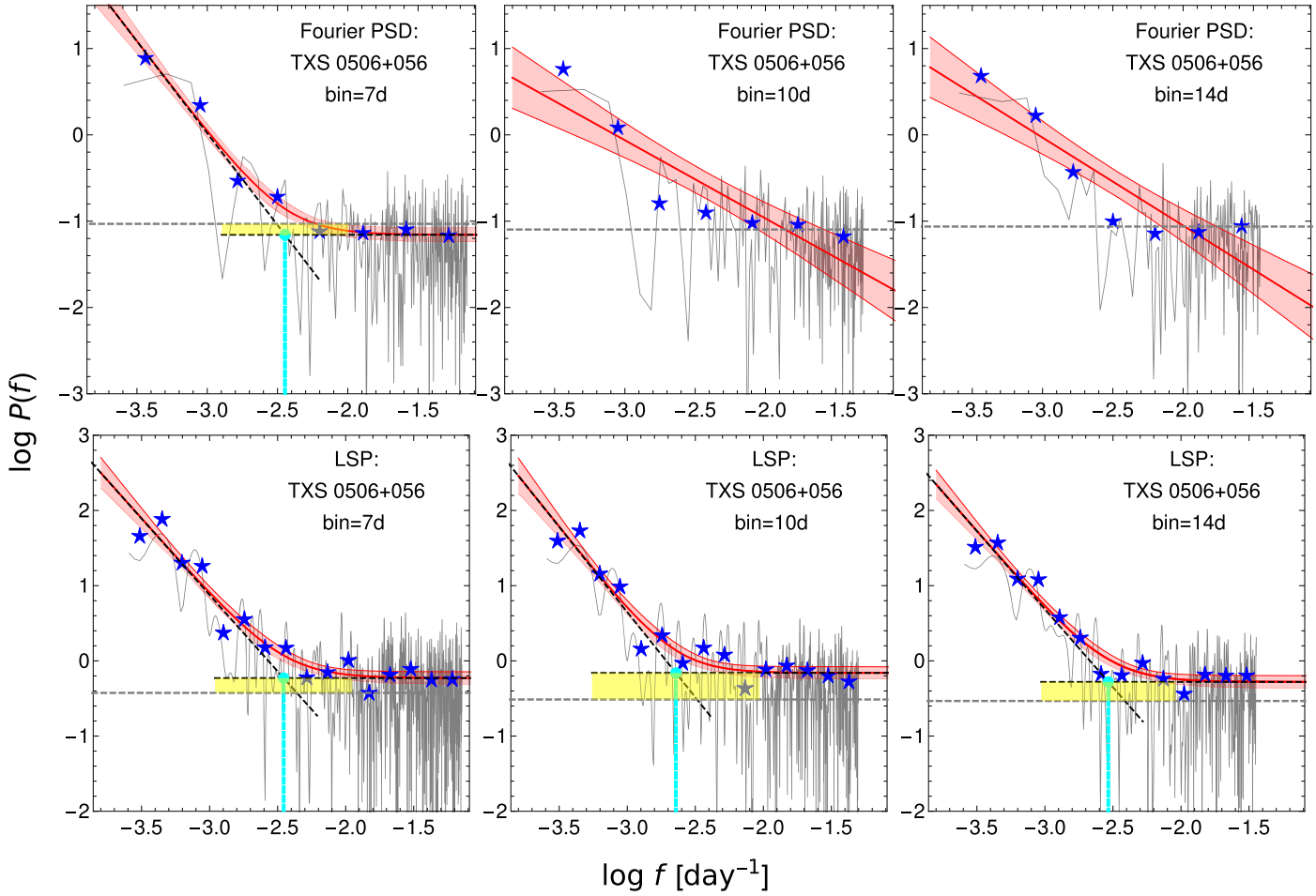

Figure 15. PSD fits with PL and PLC: Fourier spectra (*top row*) and LSPs (*bottom row*) of TXS 0506+056. The gray line is the raw LSP, and the blue stars are the binned periodogram to which fitting was performed. The red solid line is the best fit, with the lighter red region around it marking the 68% confidence interval. The black dashed lines are the PL component and C level (the parameter from Equation (13) returned by the fitting) whose intersection is marked with the cyan point. The vertical cyan line denotes the frequency f_0 above which Poisson noise dominates over the PL component. It is calculated as $P_{\rm norm}/f_0^{\beta} = C \Rightarrow f_0 = (P_{\rm norm}/C)^{1/\beta}$, and the error propagation law is used to estimate the uncertainty. The width of the yellow rectangle denotes the standard error of $\log f_0$. The horizontal gray dashed lines are the Poisson noise levels inferred from data as per Equations (11) and (17).

(The complete figure set (11 images) is available.)

regions of availability for ARMA processes, as well as fBm and fGn.

5. Results

5.1. Fourier Spectra

The Fourier spectra were generated and binned, as described in Section 3.1, for each of the 7, 10, and 14 day binnings. Next, Equations (12) and (13) were fitted in each case.[19] The better model was chosen based on the AIC_c values; if they obeyed $\Delta_i < 2$, we chose the pure PL model as the adequate one because it is simpler. The resulting β indices and their standard errors are gathered in Table 2; plots of the best fits are displayed in Figure 15. The PSDs of FSRQs are steeper than those of BL Lacs. Most of the objects gave consistent β estimates among the three bins, except for Mrk 501,[20] which yielded a wide range: 1.96, 2.53, and 1.73. Nevertheless, the PSDs are systematically flatter than in a red-noise case, $1/f^2$, with a mean of 1.19 and standard deviation of 0.43. One BL Lac, PKS 2155−304, exhibits $\beta \lesssim 1$, i.e., its PSD is significantly flatter than pink noise, $1/f$. On the other hand, two FSRQs, B2 1520+31 and B2 1633+38, are steeper than pink noise, yielding $\beta \in (1.2, 1.7)$. The remaining objects, both BL Lacs and FSRQs, are very close to a pink-noise description.

As demonstrated in Section 4.1, extracting the parameters of Equation (13) from a number of realizations of the same process leads to a wide range of results, obscuring the true underlying process. Hence, the obtained values of β are not entirely reliable. On the other hand, except for Mrk 501, employing different binnings gave highly consistent results, and in most cases it turned out that the Poisson noise did not influence the PSDs much, i.e., a pure PL was chosen as the better description. To test the robustness, from each LC we generated 1000 MC realizations by drawing the observations randomly from $\mathcal{N}(\mu, \sigma^2)$, where μ is the observed value and σ is its standard error. That is, we produced 1000 stochastic realizations of the LCs allowed by the observable uncertainties.

[19] We also checked the smoothly broken PL, where a transition between PLs with low- and high-frequency indices β_1 and β_2 occurs at a break frequency $f_{\rm break}$ (see Żywucka et al. 2020), but it was not competing in any instance.

[20] This source is dim, hence its variations are dominated by the observational (Poisson) noise.

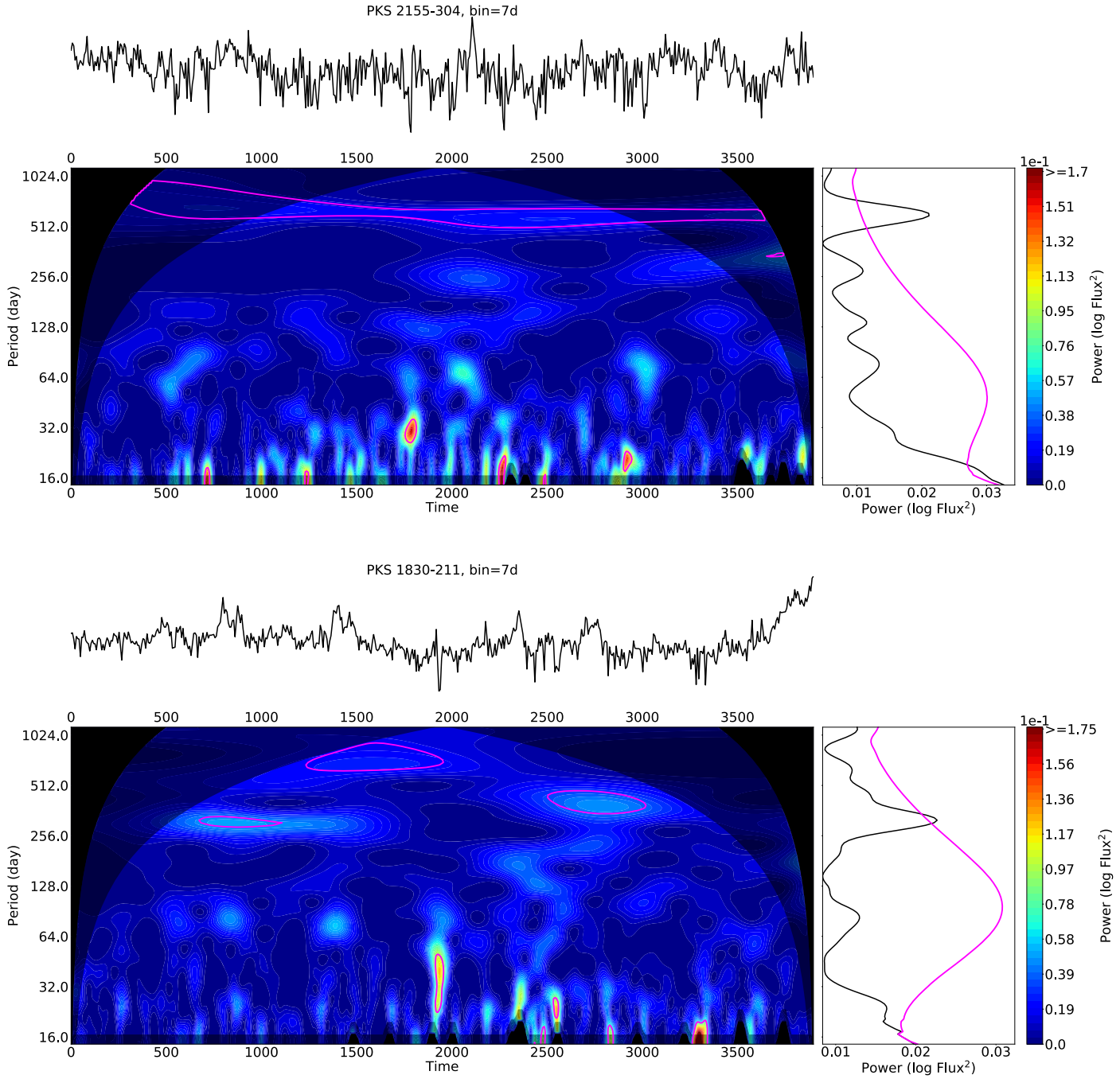

Figure 16. Wavelet scalograms of the logarithmic LCs. The magenta lines and contours denote 3σ global and local confidence levels, respectively. (The complete figure set (33 images) is available.)

The results of such procedure are gathered in Table 3, where we display the mode and standard deviation of the resulting distributions of best-fit indices, β, and the mode of their standard errors, $\Delta\beta$, which we interpret as a typical error.

The values of β from both Tables 2 and 3 are in agreement, hence the uncertainties of the flux do not play an important role in estimating β. However, it is crucial to emphasize that this only means that the estimates of the PL parameters for a given LC can be trustworthy when it comes to the impact of the errors on the outcome. Still, this particular time series might be a peculiar realization of the process governing the observed variability and need not represent the true parameters ultimately. In fact, as implied by the benchmark testing from Section 4.1, the mismatch between the (unknown) true value and the extracted one can be severe, especially when Poisson noise constitutes a significant component in the PSD.

5.2. Lomb–Scargle Periodograms

The same analysis as in Section 5.1 was performed with the LSP (see Section 3.2). The fitted β indices are gathered in Table 4; plots of the best fits are displayed in Figure 15. The values of β are slightly lower, and their errors are smaller than obtained by fitting Fourier spectra. The latter is caused by the

Table 3
Distributions' Characteristics of PL Indices β and Their Typical Errors, $\Delta\beta$, from Fourier PSDs—MC Realization of LCs by Varying Their Values within the Error Bars

Source	7 days			10 days			14 days		
	Mode	std	Typ. Err.	Mode	std	Typ. Err.	Mode	std	Typ. Err.
(1)	(2)	(3)	(4)	(5)	(6)	(7)	(8)	(9)	(10)
BL Lacs									
Mrk 501	1.61	0.17	0.25	2.07	0.27	0.52	1.74	0.33	0.32
Mrk 421	0.80	0.03	0.15	0.84	0.04	0.23	0.74	0.06	0.24
PKS 0716+714	0.89	0.02	0.20	0.88	0.04	0.24	0.87	0.04	0.31
PKS 2155−304	0.57	0.07	0.11	0.52	0.11	0.09	0.64	0.08	0.11
TXS 0506+056	1.94	0.42	0.20	0.75	0.67	0.18	0.82	0.39	0.21
FSRQs									
PKS 1510−089	0.97	0.06	0.08	1.03	0.02	0.08	1.02	0.02	0.11
3C 279	1.05	0.02	0.07	1.12	0.04	0.15	1.13	0.03	0.08
B2 1520+31	1.72	0.13	0.11	1.26	0.19	0.11	1.28	0.15	0.11
B2 1633+38	1.05	0.06	0.14	1.08	0.08	0.17	1.18	0.04	0.18
3C 454.3	1.50	0.04	0.15	1.54	0.08	0.16	1.59	0.06	0.16
PKS 1830−211	0.90	0.07	0.14	0.94	0.06	0.16	1.03	0.07	0.19

Note. Columns: (1) source name; (2) mode of the β distribution for the 7 day binning; (3) standard deviation of the β distribution for the 7 day binning; (4) typical error, i.e., mode of the $\Delta\beta$ distribution for the 7 day binning; (5) mode of the β distribution β for the 10 day binning; (6) standard deviation of the β distribution for the 10 day binning; (7) typical error, i.e., mode of the $\Delta\beta$ distribution for the 10 day binning; (8) mode of the β distribution β for the 14 day binning; (9) standard deviation of the β distribution for the 14 day binning; (10) typical error, i.e., mode of the $\Delta\beta$ distribution for the 14 day binning.

ability of the LSP to generate PSDs with larger number of points, hence constraining the fits better. In Table 5 the results of MC realizations drawn by varying the LC values within the error bars are displayed. We arrive at a similar conclusion to that in Section 5.1, i.e., the uncertainties of the flux do not affect the estimated PSD shape significantly. We repeat, though, that the PL parameters depend strongly on the particular realization of a time series, as was demonstrated in Section 4.1.

We also note that the PSDs of Mrk 501 behave in an unorganized manner—i.e., the spread of their β is wide, and the values do not overlap within errors. In particular, for the 10 day binning, the PSD is steepest. This is most likely due to it being a dim object, where the variability is obscured by observational fluctuations and statistical noise. Despite visually similar LCs among the three binnings, we clearly observe that the fitted form of the PSD is strongly dependent on the particular stochastic realization, in agreement with our findings from Section 4.1.

5.3. Wavelet Scalograms

We detect a well-known QPO in PKS 2155−304, at a period of 612 ± 42 days (Figure 16).[21] Additionally, when considering the global wavelet periodograms alone, PKS 1830−211 in the 7 day binning shows a marginal peak just above the 3σ confidence level. This peak, however, can be attributed to two short-lasting contours of $>3\sigma$ significance in the scalogram, at the borders of the COI. These contours correspond to apparently different periods. One can associate these contours with short, two-peak flux variations in the LC. They last, however, so short that they cannot be called QPOs—if so, they would consist of only two cycles each, which is likely just a chance occurrence owing to stochastic fluctuations and definitely does not constitute a significant QPO detection. There is also a 3σ contour at an even higher period, $\gtrsim$500 days, but its duration is comparable to its period. Overall, there is no convincing evidence to claim a QPO in PKS 1830−211, especially when compared to the clear picture painted by PKS 2155−304.

Table 4
PL Indices β from LSPs

Source	7 days	10 days	14 days
(1)	(2)	(3)	(4)
BL Lacs			
Mrk 501	1.83 ± 0.20[a]	2.39 ± 0.22[a]	2.08 ± 0.22[a]
Mrk 421	0.96 ± 0.07[b]	0.95 ± 0.08[b]	0.88 ± 0.08[b]
PKS 0716+714	0.97 ± 0.09[b]	0.97 ± 0.11[b]	1.03 ± 0.12[b]
PKS 2155−304	0.68 ± 0.10[b]	0.74 ± 0.10[b]	0.78 ± 0.11[b]
TXS 0506+056	2.03 ± 0.26[a]	2.26 ± 0.34[a]	2.07 ± 0.25[a]
FSRQs			
PKS 1510−089	0.96 ± 0.07[b]	0.99 ± 0.09[b]	0.98 ± 0.10[b]
3C 279	1.17 ± 0.09[b]	1.11 ± 0.11[b]	1.16 ± 0.12[b]
B2 1520+31	1.37 ± 0.14[a]	1.20 ± 0.08[b]	1.22 ± 0.09[b]
B2 1633+38	1.21 ± 0.08[b]	1.62 ± 0.18[a]	1.29 ± 0.10[b]
3C 454.4	1.95 ± 0.19[a]	2.12 ± 0.21[a]	2.05 ± 0.24[a]
PKS 1830−211	1.18 ± 0.10[b]	1.19 ± 0.11[b]	1.23 ± 0.12[b]

Notes. Columns: (1) source name; (2) β for the 7 day binning; (3) β for the 10 day binning; (4) β for the 14 day binning.
[a] PLC.
[b] Pure PL.

[21] For comparison with previous works (Sandrinelli et al. 2014, 2016; Zhang et al. 2017a) a Gaussian form was fitted to the corresponding peak in the LSP of the 7 day binned LC, and the error is the half width at half maximum. Applying the same procedure to the peak in the global wavelet periodogram yielded 605 ± 120 days (Figure 16). This period is smaller than reported by previous works (650–660 days by Sandrinelli et al. 2014; 642 days by Sandrinelli et al. 2016; 635 days by Zhang et al. 2017a), but consistent with more recent ones (610 days by Bhatta & Dhital 2020). Peñil et al. (2020) reported 620 days in a 28 day binned LC. Overall, a linear decrease over the years can be observed. The QPO is unambiguous in the 7 day binned LC examined herein, partially disappears in the 10 day binned LC, but is not present at all in the 14 day binned LC.

Table 5
Same as Table 3, but from LSPs

Source	7 days			10 days			14 days		
	Mode	std	Typ. Err.	Mode	std	Typ. Err.	Mode	std	Typ. Err.
(1)	(2)	(3)	(4)	(5)	(6)	(7)	(8)	(9)	(10)
BL Lacs									
Mrk 501	1.86	0.27	0.23	2.42	0.33	0.26	2.12	0.37	0.30
Mrk 421	0.85	0.08	0.07	0.83	0.11	0.09	0.77	0.30	0.09
PKS 0716+714	0.90	0.02	0.09	0.91	0.04	0.11	0.97	0.03	0.12
PKS 2155−304	0.56	0.05	0.09	0.56	0.26	0.10	0.62	0.08	0.12
TXS 0506+056	2.09	0.20	0.32	2.12	0.30	0.34	1.96	0.24	0.29
FSRQs									
PKS 1510−089	0.91	0.06	0.07	0.95	0.03	0.08	0.94	0.03	0.10
3C 279	1.05	0.02	0.09	1.12	0.04	0.11	1.13	0.03	0.12
B2 1520+31	1.36	0.16	0.19	1.07	0.12	0.08	1.09	0.12	0.09
B2 1633+38	1.49	0.15	0.16	1.58	0.12	0.18	1.61	0.21	0.19
3C 454.3	1.94	0.09	0.25	2.08	0.10	0.24	2.08	0.13	0.24
PKS 1830−211	1.03	0.05	0.10	1.09	0.04	0.11	1.13	0.04	0.12

Note. Columns: (1) source name; (2) mode of the β distribution for the 7 day binning; (3) standard deviation of the β distribution for the 7 day binning; (4) typical error, i.e., mode of the $\Delta\beta$ distribution for the 7 day binning; (5) mode of the β distribution β for the 10 day binning; (6) standard deviation of the β distribution for the 10 day binning; (7) typical error, i.e., mode of the $\Delta\beta$ distribution for the 10 day binning; (8) mode of the β distribution β for the 14 day binning; (9) standard deviation of the β distribution for the 14 day binning; (10) typical error, i.e., mode of the $\Delta\beta$ distribution for the 14 day binning.

Table 6
Best-fit (Method of Moments; Chosen Based on the BIC) ARMA (p, q) Orders and Break Timescales

Source	7 days		10 days		14 days	
	(p, q)	$T_{\rm break,L}$ (day)	(p, q)	$T_{\rm break,L}$ (day)	(p, q)	$T_{\rm break,L}$ (day)
(1)	(2)	(3)	(4)	(5)	(6)	(7)
BL Lacs						
Mrk 501	(5, 0)	288 ± 113	(5, 0)	593 ± 291	(5, 0)	681 ± 371
Mrk 421	(1, 1)	169 ± 42	(2, 0)	238 ± 78	(2, 0)	207 ± 87
PKS 0716+714	(4, 0)	372 ± 203	(2, 0)	268 ± 105	(1, 1)	488 ± 178
PKS 2155−304	(3, 0)	169 ± 38	(3, 0)	212 ± 60	(2, 0)	200 ± 62
TXS 0506+056	(6, 0)	772 ± 491	(5, 0)	509 ± 294	(4, 0)	813 ± 477
FSRQs						
PKS 1510−089	(1, 0)	145 ± 20	(1, 0)	216 ± 35	(1, 0)	251 ± 45
3C 279	(1, 2)	374 ± 97	(1, 1)	352 ± 84	(1, 0)	461 ± 96
B2 1520+31	(5, 0)	1199 ± 1501	(4, 0)	1438 ± 1930	(1, 1)	921 ± 351
B2 1633+38	(4, 0)	570 ± 405	(3, 0)	581 ± 350	(2, 0)	327 ± 106
3C 454.3	(1, 1)	1806 ± 724	(1, 0)	1568 ± 1918	(1, 0)	1350 ± 463
PKS 1830−211	(1, 1)	600 ± 167	(1, 1)	660 ± 195	(1, 1)	654 ± 187

Note. Columns: (1) source name; (2), (4), and (6) orders for 7, 10, and 14 day binnings; (3), (5), and (7) long timescales breaks.

There is a peculiar feature in B2 1633+38, with a 3σ contour starting at $P \sim 500$ days and increasing over the course of the LC to $P > 1000$ days. The two peaks in the global periodograms, at 634 and 1066 days, are spurious in the sense that they arise due to this one structure that evolves strongly in time. This might be called a QPO, with an emphasis on the "quasi" term, as no single leading period can be associated with it.

5.4. ARMA and FARIMA Modeling

To estimate the long-timescale breaks of the ARMA fits, we first observe that the obtained PSDs' shapes resemble the Lorentzian from Equation (40), i.e., they are flat at low frequencies, and then transition to an approximately PL decay (see the middle panels in Figure 17). The general PSD of an ARMA process, Equation (37), is not given by a combination of Lorentzian peaks,[22] though, so we proceed numerically in a way driven by an analogy with the simple Lorentzian shape. It is straightforward to check that $P_{\rm OU}(f)$ has its break at the same frequency as $fP_{\rm OU}(f)$ has its local maximum. We therefore locate the first local maximum of $fP_{\rm ARMA}(f)$ and identify it with the break frequency. To compute the uncertainties, the

[22] For some values of the parameters, the PSD can be completely non-Lorentzian, e.g., monotonically increasing.

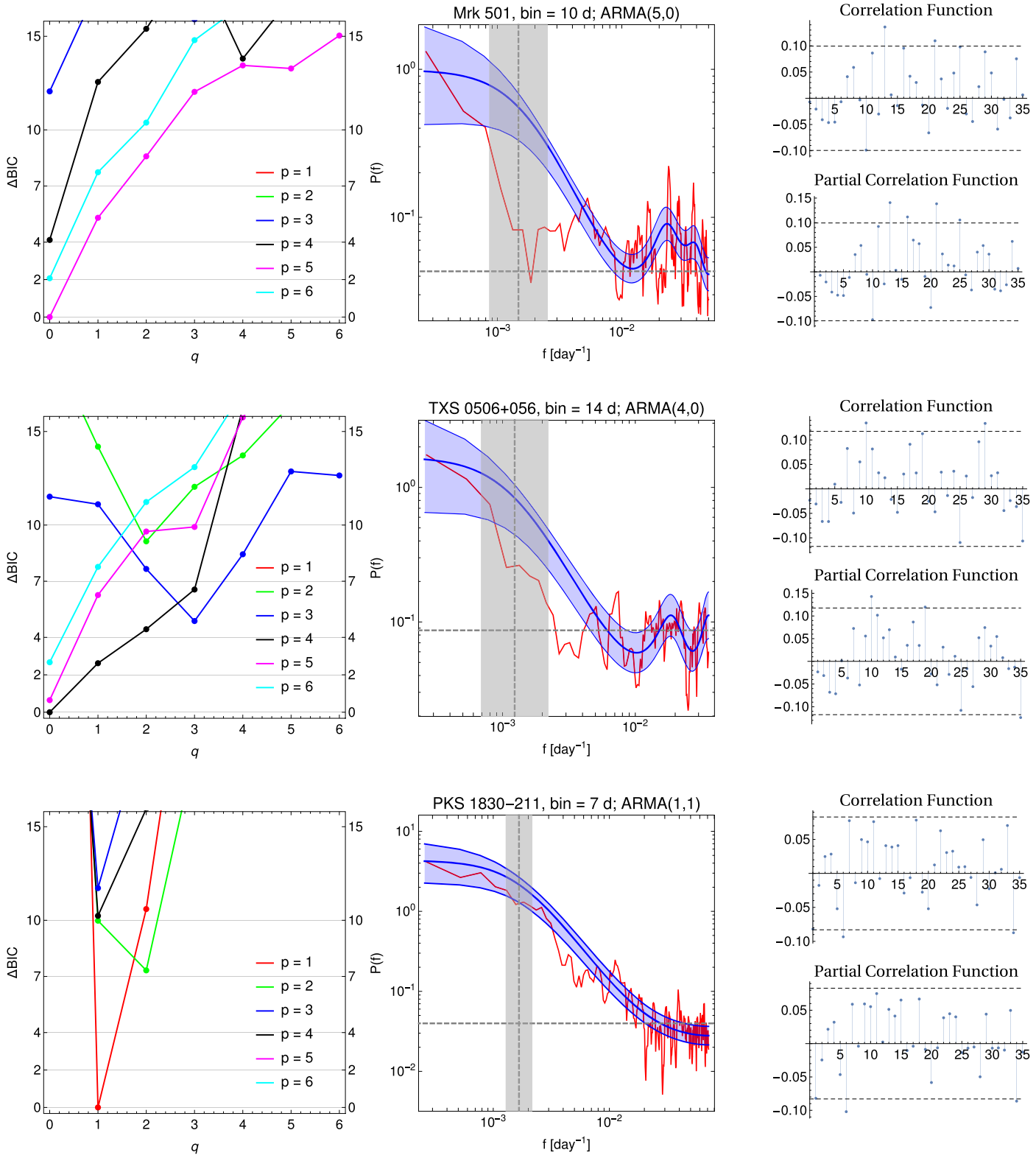

Figure 17. Results of the ARMA fitting. The blue line in the middle column is the PSD of the best-fit ARMA model, surrounded by a light blue 68% confidence band. The horizontal dashed line is the Poisson noise level inferred from the data. The vertical dashed line marks the break frequency, corresponding to $T_{\mathrm{break,L}}$ from Table 6, and the width of the gray rectangle symbolizes its standard error. The red line is the Fourier PSD, smoothed with a five-point moving average, to show the relation between the ARMA and Fourier features. The left column displays the ΔBIC scores of the ARMA(p, q) fits. The right column contains the correlation and partial correlation functions of the fits' residuals; the dashed lines enclose the 95% confidence region.

(The complete figure set (33 images) is available.)

parametric bootstrap is employed (Tarnopolski 2015b, and references therein): we generate 500 PSDs by varying randomly the coefficients of the best-fit ARMA model within their errors and take the standard deviation of the distribution of breaks as the standard error.

The ARMA(p, q) models were fitted using the method of moments first. For choosing the best fit, we employed BIC, because, as implied by the benchmark testing from Section 4.3, it is more likely to return if not q, then at least p close to the real value when noise is present in the observations. In particular, the best model is chosen to be the one with the smallest p within the band $\Delta_i < 2$. The outcomes of this method are compiled in Table 6. However, as demonstrated in Appendix A, the maximum likelihood estimation is prone to underestimate the order. In most instances the results do not match: (1, 1) was the most commonly returned order, with the occasional (2, 1), (2, 0), (1, 0), or (1, 2). On one hand, the method of moments is more likely to point at a plausible model as indicated by the testing from Section 4.3; on the other hand, the higher-order models, e.g., ARMA(5, 0) in the case of Mrk 501 or TXS 0505+056, but also B2 1510+31, B2 1633 +38, and PKS 2155−304, are modeling the variations at the Poisson noise level, hence are likely overfitting, i.e., are modeling the fluctuations related to uncertainties in the data, and hence their order is superficially elevated to take this into account and does not entirely reflect the features of the underlying process that governs the variability.

Note that AIC_c, as noted in Section 2.4, is more liberal than BIC, hence points at unnecessarily complex models. In the case of the examined blazars, it returned (p, q) as high as (8, 8) or (9, 7). All in all, the combination of the method of moments and BIC gives the most reliable description of the LCs at hand, and hence we proceed to discuss them.

In the defining Equation (29) of the ARMA process, the observation x_t is directly influenced by the p preceding ones. For example, let $p = 4$ in an LC with a 7 day binning. This means that the observations from the previous 28 days (in the observer frame) affect the current value. For an LC with a 14 day binning, one can then expect $p = 2$ in order to maintain the same timescale τ. We see exactly this pattern in the case of B2 1633+38 (Table 6).

Mrk 501 (in the 10 day binning) yields ARMA(5, 0). At higher frequencies (corresponding to timescales $\lesssim$90 days; see Figure 17), we observe local maxima above the Poisson noise level—these might be either QPOs or just fluctuations—especially as wavelet scalograms show no signs of QPOs at all (Section 5.3). In the case of TXS 0506+056 (for all binnings), the high-frequency variations are exactly at the Poisson noise level. PKS 1830−211 consistently exhibits a prominent break in its PSD at a timescale of several hundred days (see Table 6). On the other hand, Fourier spectra and LSPs do not hint at any break (compare with Sections 5.1 and 5.2).

Overall, we observed breaks at timescales of a few hundred days in all but the following objects: B2 1520+31 (for which we obtain very big uncertainties) and 3C 454.3 (for which the breaks correspond to very long timescales, as the PSD of this source is highly consistent with a pure PL). The most pronounced and well-constrained breaks occur in Mrk 421, PKS 2155−304, PKS 1510–089, and 3C 279. The break timescales are generally consistent with break timescales obtained by CARMA modeling (see Section 5.5). This equivalence is to be expected, as CARMA is just a continuous-time version of ARMA, and the data herein are nearly uniformly sampled, with not many missing points, hence the two models ought to give similar results.

5.5. CARMA Modeling

Ryan et al. (2019) recently investigated daily and weekly LCs of eight blazars examined herein as well, except for Mrk 501, TXS 0506+056, and PKS 1830−211, by fitting CARMA(p, $p-1$) models, $1 \leqslant p \leqslant 5$, and found that in all cases $p = 1$ or $p = 2$ give the best fits. We performed a broader search for $1 \leqslant p \leqslant 7$ and $0 \leqslant q \leqslant 6$. We employ BIC and choose the simplest model (i.e., with the lowest p) within the band $\Delta_i < 2$ as the best fit. Our results, summarized in Table 7, are generally in agreement with Ryan et al. (2019). In the case of the 7 day binning of PKS 2155−304, when restricted only to CARMA(p, $p-1$), we also obtain $p = 2$ as the best and $p = 1$ as the simplest model within $\Delta_i < 10$. Likewise for PKS 1830−211 in a 7 day binning. In these two fittings, however, the orders exceeding (2, 1) appear to be spuriously elevated to take into account subtle variations below the Poisson noise level and hence imply overfitting. Indeed, when the higher-order and simple models are compared (Figure 18), they all exhibit PSDs broadly consistent with each other within the confidence intervals.

In particular, almost all fits are in fact consistent with the simplest, CARMA(1, 0) model, as in the case of CARMA(2, 1) fits, the second break in the PSD is mostly located below the Poisson noise level. The only exception is 3C 279, with breaks at ∼2000 and ∼100 days (see Figure 19). Curiously, the 8.5 yr long Fermi-LAT LC of the famous source OJ 287 exhibits a break at ∼150 days in a CARMA(1, 0) best fit (Goyal et al. 2018).

The fits to Mrk 501, TXS 0506+056, and PKS 1830 −211 are featureless, with T_{break} at very long timescales, making the PSDs consistent with a PL description. In particular, there are no signs of a QPO in the case of PKS 1830−211, contrary to what the global wavelet periodogram (7 day binning; Section 5.3) might suggest. In conclusion, we did not detect any peculiar features in the PSDs obtained with fitting CARMA models to our data. The break timescales that are above the Poisson noise level are either at a few hundred or several thousands of days.

5.6. Hurst Exponents

We used all methods from Section 3.6 to estimate the Hurst exponents. The results are summarized graphically in Figure 20. In some instances, fitting a FARIMA model returned $d = 0.5$ (leading to $H = 1$), which implies nonstationarities present in the respective LCs. As illustrated in Figure 13, FARIMA fitting is biased toward higher H when applied to PLC (and even more biased in the case of fBm); it has great dispersion when used in fGn and FARIMA models; while usually correctly recovering $H \approx 0.5$ for ARMA, it can drift toward $H = 0$ or 1; and finally, for CARMA models it consistently returns H close to 1. Therefore, not much meaning can be given to the H estimates from the FARIMA fitting (Torre et al. 2007).

On the other hand, the Fourier spectra and LSPs yielded for many objects $\beta \approx 1$, which due to the discontinuity of H at the border between stationary and nonstationary processes (see Figure 6) makes it uncertain whether $H \gtrsim 0$ or $H \lesssim 1$. Only Mrk 501, PKS 2155−304, B2 1520+31, and B2 1633+38 are

Table 7
Best-fit CARMA(p, q) Orders and Break Timescales

Source	7 days			10 days			14 days		
	(p, q)	$T_{\rm break,L}$ (day)	$T_{\rm break,S}$ (day)	(p, q)	$T_{\rm break,L}$ (day)	$T_{\rm break,S}$ (day)	(p, q)	$T_{\rm break,L}$ (day)	$T_{\rm break,S}$ (day)
(1)	(2)	(3)	(4)	(5)	(6)	(7)	(8)	(9)	(10)
BL Lacs									
Mrk 501	(2, 1)	1907 ± 1355	22 ± 14[a]	(2, 1)	2727 ± 1137	17 ± 6[a]	(2, 1)	2140 ± 1995	35 ± 22[a]
Mrk 421	(1, 0)	389 ± 107	⋯	(1, 0)	502 ± 158	⋯	(1, 0)	497 ± 168	⋯
PKS 0716+714	(1, 0)	262 ± 64	⋯	(1, 0)	322 ± 74	⋯	(1, 0)	360 ± 92	⋯
PKS 2155−304	(3, 0)[b]	532 ± 333	17 ± 11[a]	(1, 0)	240 ± 65	⋯	(1, 0)	345 ± 111	⋯
TXS 0506+056	(2, 1)	2978 ± 975	13 ± 5[a]	(2, 1)	2739 ± 1214	21 ± 9[a]	(2, 1)	2885 ± 1063	24 ± 9[a]
FSRQs									
PKS 1510−089	(1, 0)	209 ± 34	⋯	(1, 0)	260 ± 48	⋯	(1, 0)	308 ± 65	⋯
3C 279	(2, 1)	2015 ± 1556	99 ± 61	(1, 0)	387 ± 87	⋯	(1, 0)	581 ± 187	⋯
B2 1520+31	(3, 1)[b]	3087 ± 961	102 ± 33[a]	(1, 0)	1447 ± 1131	⋯	(5, 0)[c]	2304 ± 1761	⋯
B2 1633+38	(1, 0)	802 ± 563	⋯	(1, 0)	1148 ± 756	⋯	(1, 0)	1284 ± 985	⋯
3C 454.3	(1, 0)	1967 ± 1610	⋯	(1, 0)	2671 ± 2414	⋯	(1, 0)	3073 ± 2639	⋯
PKS 1830−211	(3, 0)[b]	2110 ± 1126	20 ± 15[a]	(1, 0)	2483 ± 2434	⋯	(1, 0)	4217 ± 4061	⋯

Notes. Columns: (1) source name; (2), (5), (8) orders for 7, 10, and 14 day binnings; (3), (6), (9) long-timescale breaks; (4), (7), (10) short-timescale breaks.
[a] Below the Poisson noise level.
[b] This was returned as the best order, but the given $T_{\rm break,L}$ and $T_{\rm break,S}$ refer to a CARMA(2, 1) fit.
[c] For CARMA(2, 1), $T_{\rm break,S} = 120 \pm 355$ days, effectively implying no break. The given $T_{\rm break,L}$ refers to a CARMA(1, 0) fit.

far enough from the border to allow H to be confidently inferred from β (Tables 2 and 4). However, as Mrk 501 gives inconsistent β for different binnings, the corresponding H span the range 0.4–0.8. For PKS 1510−089, Fourier spectra lead to $H \approx 0$, while LSPs yield $H \approx 1$.

The AWC often drifts to $H > 1$, which is a nonsensical value. Overall, it systematically returns $H > 0.5$. Its performance for PLC (see Figure 13) is poor, and it greatly misidentifies $H \approx 0$ as $H \approx 1$ when nonstationarities are present, e.g., in the fBm case, so technically also for $\beta > 1$. The performance of the R/S algorithm is also poor and hence unreliable. Only DFA and DWT are left.

We undertook the following approach in order to try to differentiate between $H > 0.5$ and $H < 0.5$. Given a time series of length N, it was divided into windows of size $\lfloor n/2 \rfloor$. The first window starts at x_1, the second advances one points and starts at x_2, etc. We end with $\lceil n/2 \rceil$ such chunks; to each we apply the DFA algorithm, and eventually obtain the time evolution of H. The H values for each LC and binning will vary over time, but we aim to seek a general answer whether $H > 0.5$ or $H < 0.5$, or whether it oscillates discontinuously between $H \approx 0$ and $H \approx 1$. The results are compiled in Figure 21, where the time evolution of $\mathcal{A}$ and $\mathcal{T}$ is also displayed (see Section 5.7).

We indeed confirm that for blazars characterized by $\beta \approx 1$, the H values behave incoherently in time. For the most part, Mrk 501 and TXS 0506+056 actually exhibit $H > 0.5$, implying long-term memory. PKS 2155−304 is the best-behaved object, with the time evolution of H consistent in all three binnings. We observe jumps between $H \approx 0$ and $H \approx 1$ for B2 1520+31 and B2 1633+38, suggesting that the β estimates obtained in Sections 5.1 and 5.2 do not capture the true stochastic dynamics of the system. We can safely conclude that long-range dependence is rather confidently detected in the LC of PKS 2155−304, and likely also for Mrk 501 and TXS 0506+056. On the other hand, 3C 454.3 is the only object for which $H < 0.5$ is consistently returned, in agreement with $\beta \lesssim 2$, suggesting its variability is fBm like, with short-term memory.

5.7. The $\mathcal{A}$–$\mathcal{T}$ Plane

The locations in the $\mathcal{A}$–$\mathcal{T}$ plane were calculated according to Section 3.7. To constrain the errors, from each LC we generated 1000 MC realizations by drawing the observations randomly from $\mathcal{N}(\mu, \sigma^2)$, where μ is the observed value and σ is its standard error, and for each realization the $(\mathcal{A}, \mathcal{T})$ location was computed. The dispersion is assessed by the standard deviation of the 1000 MC samples. The results are displayed in Figure 22, where the region available to generic PLC models is highlighted. Per Sections 5.1 and 5.2, the majority of the examined blazars are well described by a pure PL: Mrk 421, PKS 0716+714, PKS 2155−304, PKS 1510−089, and 3C 279, using both Fourier spectra and LSPs. Four of them are close to a pink-noise PL with $\beta \approx 1$, except for PKS 2155−304, which yields $\beta \approx 0.7$–0.8. The $(\mathcal{A}, \mathcal{T})$ locations are roughly consistent with $\beta \in (1, 1.5)$, but generally shifted toward slightly steeper PL PSDs. This is in agreement with the underestimation of the β indices observed in the benchmark tests in Section 4.1. Note, however, that in the case of Mrk 421, we observed a slight, and in the case of PKS 2155−304, a strong, shift upwards the $\mathcal{A}$–$\mathcal{T}$ plane.

Mrk 501 is the source that is most shifted to the right and upwards, which is due to a high level of Poisson noise dominating the PL component in a substantial part of its PSD. The result of increasing the Poisson noise (Figure 7) is that the path for different β is raised and shortened. Hence, the $(\mathcal{A}, \mathcal{T})$ locations are shifted closer to the point $(1, 2/3)$ corresponding to white noise. Therefore, overall the description of Mrk 501 in the $\mathcal{A}$–$\mathcal{T}$ plane is reasonable.

Finally, B2 1520+31 and B2 1633+38 yield $\beta \gtrsim 1$, but for some binnings the PSDs were better described by a PLC rather than a pure PL. They behave differently in the $\mathcal{A}$–$\mathcal{T}$ plane: for

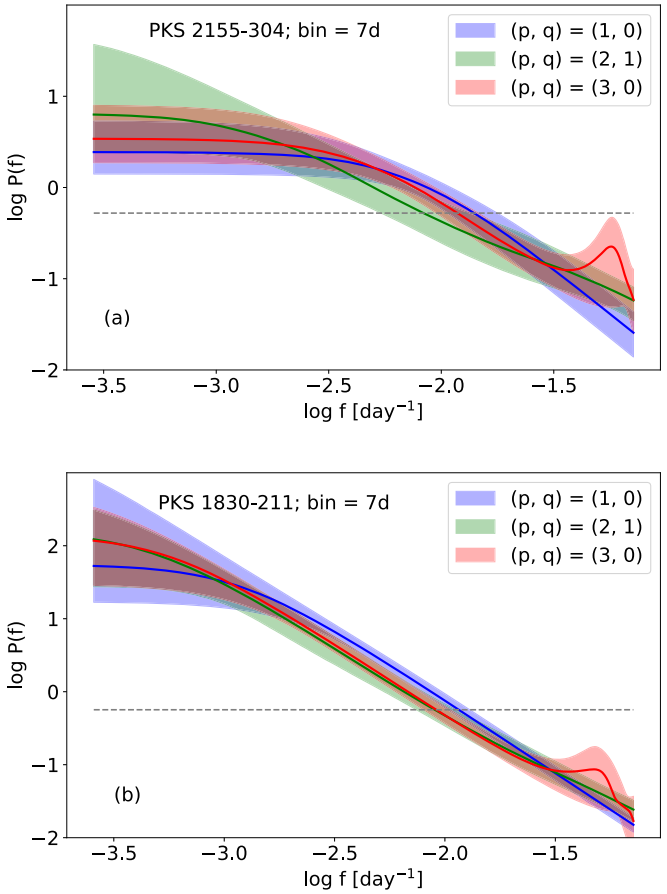

Figure 18. Comparison of the high-order CARMA model obtained as the best fit according to BIC, and the simple ones with orders (1, 0) and (2, 1), for (a) the 7 day binned LC of PKS 2155−304 and (b) PKS 1830−211 in the 7 day binning. The horizontal dashed lines mark the Poisson noise level inferred from the data. The two other cases (B2 1520+31 with 7 and 14 day binning—see Table 7) have similarly overlapping PSDs (but with no signs of the high-frequency peak visible here below the Poisson noise level), and hence are not displayed.

higher binnings, B2 1520+31 moves vertically upwards, while 1633+38 moves diagonally to the right and downwards. The latter appears to be more consistent with a pure PL location; for the 10 day binning, there is strong support for the pure PL model in the LSP approach ($\Delta_i \approx 3.5$). For the 7 day binning of B2 1520+31, though, the pure PL is out of question, with $\Delta_i > 10$ in the Fourier approach and $\Delta_i \approx 4.5$ in the case of the LSP, which means inconsiderable support for the pure PL model.

Recall that the LCs, despite spanning a long period in time, contain a moderate number of points, especially for the 10 day and 14 day binnings. On the other hand, the 7 day binning allows for a denser sampling, but increases the uncertainty of the measurements.

6. Discussion

6.1. Summary of Results

We analyzed with a number of techniques the Fermi-LAT γ-ray LCs of 11 blazars. The global PSDs were obtained via Fourier spectrum and the LSP, and subsequently used to compute the PL indices β. The values resulting from these methods are consistent with each other (see Tables 2 and 4). There is a small discrepancy only in the case of 3C 454.3, for which the Fourier PSD is described by a pure PL, and the LSP by PLC—the latter being slightly steeper than the former. Overall, the resultant shapes indicate a colored noise with $1 \lesssim \beta \lesssim 2$.

We employed wavelet scalograms to detect transient phenomena. We confirmed the well-known QPO in PKS 2155−304, with a period of 612 ± 42 days. We did not find any other similarly unambiguous QPOs at the 3σ confidence level. B2 1633+38 exhibits a peculiar significant feature that evolves from $P \sim 500$ days to $P > 1000$ days over the span of the LC, which might be associated with the previously reported presumed QPOs with $P \sim 600$ days (Otero-Santos et al. 2020). Additionally, there is a peak in the global wavelet PSD in the 7 day binned LC of PKS 1830−211. This, however, appears to be a dubious detection, as the statistically significant features in the scalogram are located exactly at the border of the COI, at two different frequencies, and can be identified with at most two cycles in the LC. Moreover, there is no significant detection in the 10 and 14 day binned LCs of this source. We therefore conclude a lack of significant QPOs in the remaining sample of blazars. In particular, we cannot confirm the presence of QPOs in Mrk 501 (Bhatta 2019), Mrk 421 and PKS 0716+714 (Bhatta & Dhital 2020), PKS 1510−089 and 3C 279 (Sandrinelli et al. 2016), and B2 1520+31 (Gupta et al. 2019; compare with Table 1). Finally, we observe hints of a significant, persistent structure in the scalograms of PKS 0716+714 at $P \gtrsim 1000$ days. This might be a candidate QPO, but because the ratio of the period to the length of the LCs allows for two to three cycles only, it does not constitute a detection yet. Similar conclusions were drawn by Bhatta & Dhital (2020), while Peñil et al. (2020) reported a low-significance QPO detection at a period of ∼1000 days. Further monitoring of this source is therefore required.

We modeled the LCs as discrete stochastic processes, ARMA and FARIMA, fitting them with the method of moments and by the maximum likelihood estimation. The latter yielded simple, low-order $p \leqslant 2$ models. The method of moments, however, in some instances (Mrk 501, PKS 0716+714, PKS 2155−304, B2 1520+31, B2 1633+38) returns higher orders. For most of them (Mrk 501, PKS 2155−304, B2 1520+31, B2 1633+38), the increased model complexity is caused by overfitting at the Poisson noise level. On the other hand, PKS 0716+714 shows nontrivial features significantly above the Poisson noise level and hence hints at a more complicated process underlying the observed variability.

The LCs were modeled as CARMA processes as well (Table 7). We searched for the best CARMA(p, q) model with $1 \leqslant p \leqslant 7$ and $0 \leqslant q \leqslant 6$. In almost every instance we obtained the orders (1, 0) or (2, 1). In only a few cases did the BIC point at more complex models, but their PSDs are consistent with these simple instances (see Figures 18 and 19), as the additional parameters introduced by higher orders were utilized for overfitting below the Poisson noise level. We are therefore in agreement with the results of Ryan et al. (2019) when it comes to the eight blazars common to both works. Additionally, the CARMA fits to Mrk 501, TXS 0506+056, and PKS 1830−211 are consistent with a PL description, i.e., CARMA(1, 0) with a high $T_{\rm break,L}$.

Nevertheless, motivated by the fact that the proper model to describe the data may not necessarily be a simple PL, we estimated the Hurst exponents with several of the most popular and established methods. For most BL Lacs we obtain $H > 0.5$

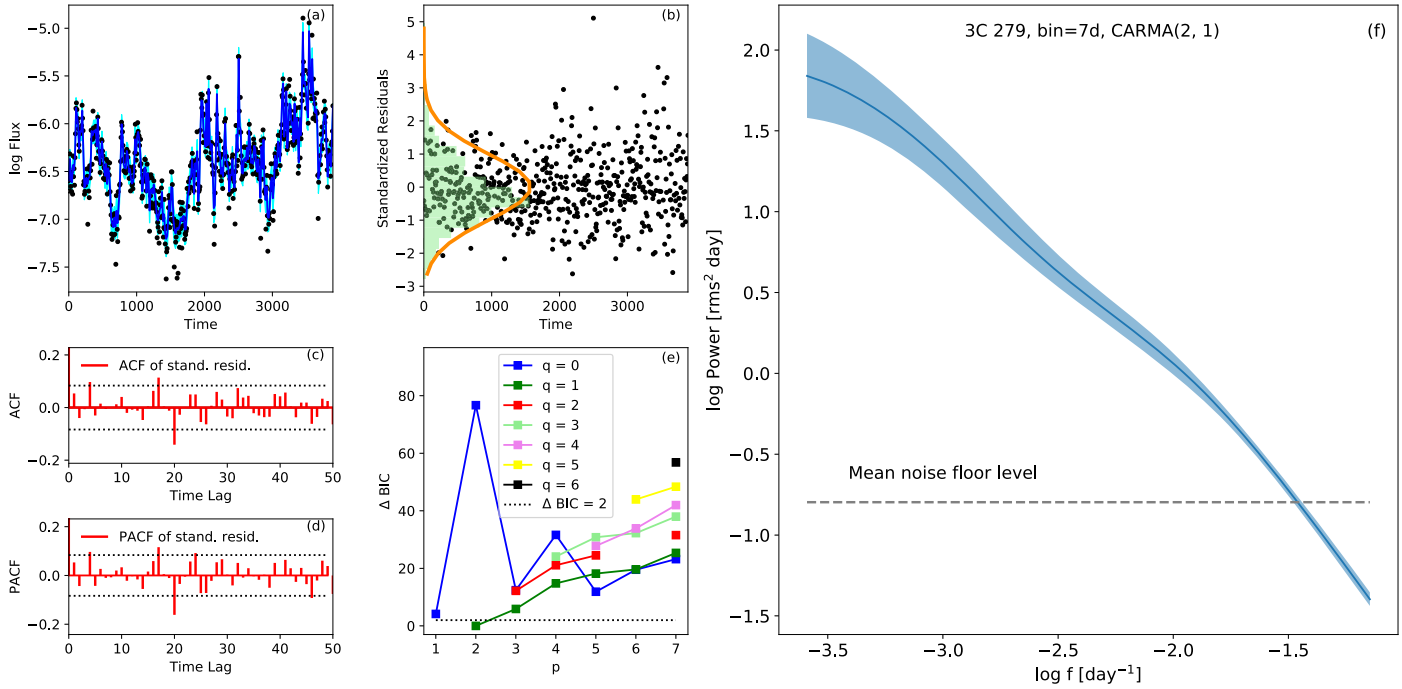

Figure 19. Results of the CARMA fitting. (a) The best fit to the LC. (b) Standardized residuals of the fit. (c)–(d) Autocorrelation and partial autocorrelation functions of the fit's residuals. (e) The ΔBIC scores of the CARMA(p, q) fits. (f) The blue line is the PSD of the best-fit CARMA model, surrounded by a light blue 68% confidence band. The horizontal dashed line is the Poisson noise level inferred from the data.

(The complete figure set (33 images) is available.)

significantly, signifying long-term memory. The FSRQs, however, kept oscillating between $H \lesssim 1$ and $H \gtrsim 0$, except 3C 454.3 for which $H < 0.5$ convincingly. We emphasize, though, that some of the objects (Mrk 421, PKS 0716+714, and most FSRQs) do not allow an unambiguous claim about their persistence to be formulated: there is no convincing majority of consistent H estimates to infer whether $H \lessgtr 0.5$. This is in accordance with the fact that their PSDs are highly consistent with a PL description with $\beta \sim 1$: due to the discontinuity of H (see Figure 6), it is difficult to distinguish between stationary cases with $H \lesssim 1$ and nonstationary ones with $H \gtrsim 0$. We note that it might be proper to model the LCs as a CARFIMA process (Tsai & Chan 2005; Tsai 2009; Feigelson et al. 2018), i.e., a fractionally integrated CARMA process (or, in other words, a continuous-time FARIMA) that allows for long-term memory, as well as CARMA driven by a Lévy process (Brockwell 2004; Brockwell & Marquardt 2005). Likewise, the fractional Fokker–Planck equation admits long-term memory solutions (Weron et al. 2008; Deng & Barkai 2009) and might be used to model the electron distribution (Stawarz & Petrosian 2008; Chen et al. 2011), thus constituting a generalization of the kinetic continuity equation (Finke & Becker 2014, 2015).

With regard to the memory of the process, consider again the orders of the ARMA models. If the observed variability is caused by some (possibly recurring) disturbance in the jet or disk, it will need some time to dissolve. One can then expect that increasing the binning of an LC twice will reduce the ARMA order twice as well, which is indeed the case for some blazars (Section 5.4). The relation between the rest and observer frames is $\tau_{\rm rest} = (1+z)^{-1}\tau_{\rm obs}$. In particular, for B2 1633+38 (7 day binning; as per Table 6), $\tau_{\rm obs} = 28$ days transforms to 10 days in the rest frame. A decrease of the order p with the increase of the bin size is also evident, although less clear, for PKS 0716+714, PKS 2155−304, and B2 1520+31, to which we relate $\tau_{\rm rest} = 21$, 19, and 14 days, assuming $\tau_{\rm obs} = 28$, 21, and 35 days, according to the orders p for a 7 day binning. Such a relation suggests there might exist a characteristic timescale for the perturbations to die out, i.e., any fluctuation in the jet affects the emission for time $\tau_{\rm rest}$. Physical differences in the blazars, e.g., BH mass, accretion rate, etc. could lead to different $\tau_{\rm rest}$.

Finally, we highlight a novel finding made with the recently introduced $\mathcal{A}$–$\mathcal{T}$ plane: the FSRQs and BL Lacs are clearly separated, as shown in Figure 22. The FSRQs are characterized by values of $\mathcal{A}$ lower than those of BL Lacs. The same phenomenon was also discovered by Żywucka et al. (2020) in the optical (I-band) LCs of blazar candidates behind the Magellanic Clouds (Żywucka et al. 2018), observed by the Optical Gravitational Lensing Experiment (OGLE). This demonstrates that the interrelations between flux values are different for the two blazar populations and allows them to be distinguished based solely on data in the time domain, without referring to PSDs or spectroscopic properties. Moreover, the separation is insensitive to sampling: the blazar candidates from Żywucka et al. (2020) were observed irregularly, with a time step approximately a multiple of 1 day, while the γ-ray LCs examined herein were binned into 7, 10, and 14 day intervals.

The separation, at first glance, might appear to be a result of FSRQs having on average steeper PSDs than BL Lacs. This is not the case: this would be true if all objects were located at the pure PL line in the $\mathcal{A}$–$\mathcal{T}$ plane, and their locations would be consistent with the β estimates. However, the examined sources attain various values of $\mathcal{T}$, too, sometimes placing them far from the PL line. As an effect of adding Poisson noise, the PL line is elevated and shortened, i.e., pulled closer to the point

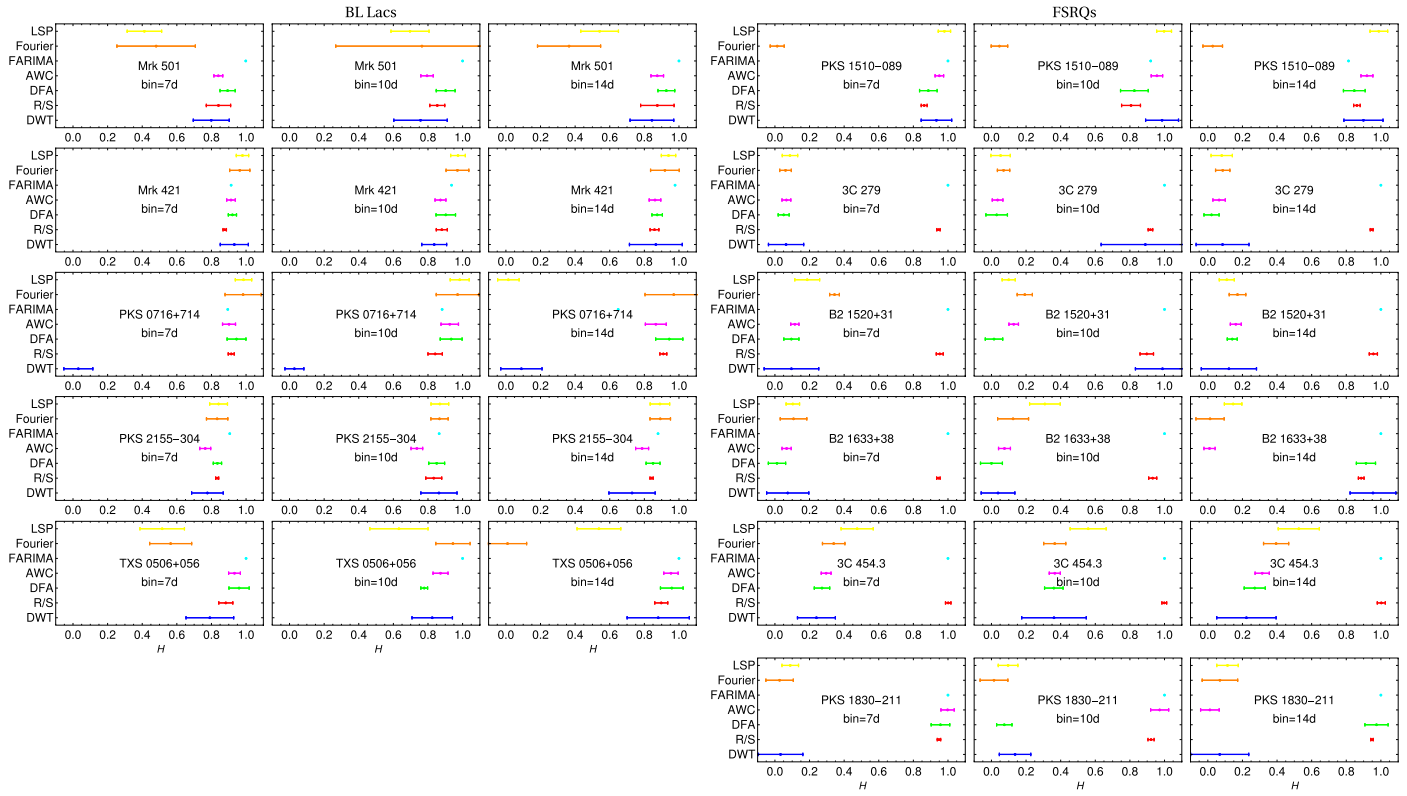

Figure 20. Estimates of H for BL Lac–type objects and FSRQs.

$(1, 2/3)$ corresponding to white noise. Such a path is depicted in magenta in Figure 22, and it does not separate the two classes at all. Most of the blazars' PSDs herein are consistent with a pure PL, though; hence, the location in the $\mathcal{A}$–$\mathcal{T}$ plane highlights some hidden properties in the time series' temporal structure, not revealed by Fourier spectra or LSPs. Moreover, the region of availability for PSDs of PLC is also available to ARMA processes (see Figure 14 and Tarnopolski 2019a for an analytic treatment).

6.2. Comparison with Previous Studies

PL indices—Nakagawa & Mori (2013) analyzed almost 4 yr long LCs of 15 blazars from the Monitored Source List (MSL), provided by the Fermi-LAT team, using the Fourier transform. Their sample contains five blazars the same as in our work, i.e., Mrk 421, 3C 279, PKS 1510−089, PKS 2155−304, and 3C 454.3. The PL indices β of the considered blazars are compatible with our results within errors, except for Mrk 421, for which we obtained a steeper PSD (0.93 ± 0.12 versus 0.38 ± 0.21). Thirteen blazars, with a particular emphasis on blazar types, i.e., eight FSRQs and five BL Lacs, were analyzed by Sobolewska et al. (2014) with a superposition of OU processes. Their sample also includes a bunch of blazars studied in this work: B2 1633+38, B2 1520+31, 3C 454.3, 3C 279, PKS 1510−089, PKS 0716+714, PKS 2155−304, and Mrk 421, for which they find PL indices mostly to be $\beta \lesssim 1$. There is also no difference in β values among the two blazar types. Abdo et al. (2015) studied a 3 yr long LC of PKS 1830−211, generated with the unbinned maximum likelihood technique. Our Fourier PSD is slightly flatter than theirs (1.05 ± 0.15 versus 1.25 ± 0.12). The 7 yr long LCs (calculated with unbinned maximum likelihood method) of three blazars were analyzed by Kushwaha et al. (2017). Common objects in this case are Mrk 421, B2 1520+31, and PKS 1510−089. The PL index of Fourier PSDs is in agreement only for PKS 1510−089, while for Mrk 421 and B2 1520+31, we obtained flatter and steeper PSDs, respectively. Prokhorov & Moraghan (2017) obtained $\beta = 0.57$ for PKS 0716+714 and $\beta = 0.67$ for PKS 2155−304, while we obtain $\beta \sim 1$ and $\beta \sim 0.75$, respectively. They get β within ∼0.5–0.8, though, for all their sources. Algaba et al. (2018) analyzed a 3 yr long LC of B2 1633+38, generated with the adaptive binning method, to study its variability in radio, optical, and HE γ-rays. Here again the fitted PL is flatter in our case (1.22 ± 0.15 versus 1.70 ± 0.20). Bhatta (2019) investigated a 10 yr long LC of Mrk 501, generated with the unbinned maximum likelihood method, finding a PL index of 0.99 ± 0.01, which is much flatter than the value found in this work (1.83 ± 0.20). Covino et al. (2019) examined long-term (∼decade), 30 day binned aperture photometry LCs generated by the Fermi team of 10 blazars, including PKS 0716+714 and PKS 2155−304. Our PL index is comparable in the case of the previous blazar, but gives a flatter PSD for the latter one. Subsequently, Meyer et al. (2019) investigated 9.5 yr long, weekly binned LCs of six FSRQs, including PKS 1510−089, 3C 279, and 3C 454.3. Except for PKS 1510−089, they obtained clearly flatter PL fits than we do, i.e., ∼0.9, 0.65, 1.1 versus our 1.03, 1.12, 1.68 (Fourier PSDs) or 0.96, 1.17, 1.95 (LSPs), respectively. Our results are consistent with Bhatta & Dhital (2020), except for 3C 454.3, for which the authors reported $\beta = 1.3 \pm 0.17$, while we obtained $\beta \sim 2$. Finally, regarding Mrk 421 and PKS 2155−304, we obtained values broadly consistent with those of Goyal (2020).

All discrepancies highlighted here are most likely caused by different methods of data analysis, e.g., the methods of

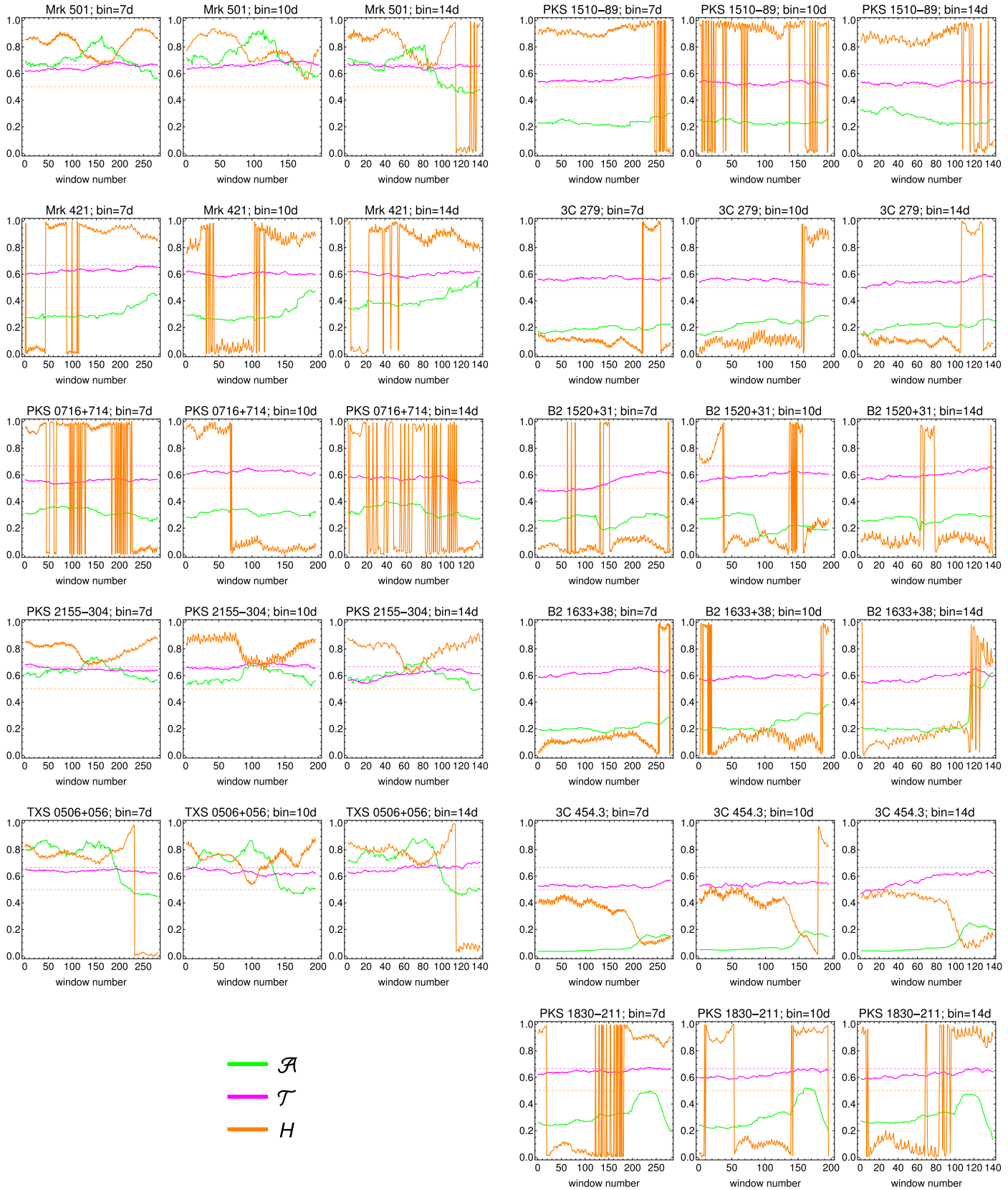

Figure 21. Time evolution of the Hurst exponents H estimated with the DFA, Abbe values $\mathcal{A}$, and fractions of turning points $\mathcal{T}$. The legend applies to all panels. The horizontal dashed orange line denotes $H = 0.5$, and the magenta one is $\mathcal{T} = 2/3$. Left three columns: BL Lacs; right three columns: FSRQs.

generating and fitting the PSDs, as well as differences in the data itself, i.e., lengths of the analyzed LCs or method of their generation.

QPOs—Several authors reported QPOs in different blazars in recent years. Sandrinelli et al. (2014) analyzed long-term IR, optical, and HE γ-ray (MSL Fermi-LAT) LCs of PKS 2155

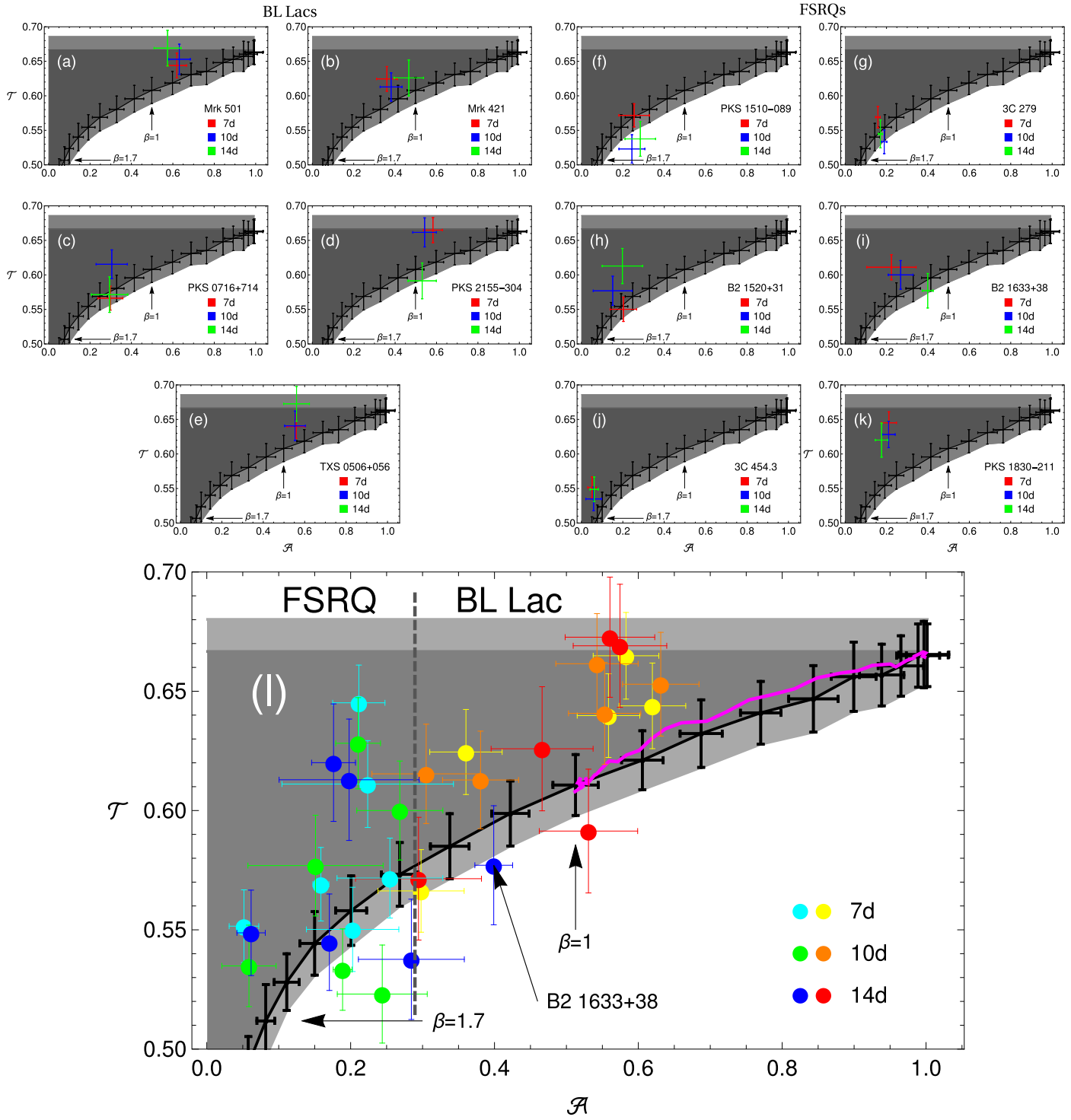

Figure 22. Locations in the $\mathcal{A}$–$\mathcal{T}$ plane of (a)–(e) BL Lacs and (f)–(k) FSRQs. The dark-gray area is the region between the pure PL line (traced by the red points from Figure 7, repeated here—in black—for convenience) and $\mathcal{T} = 2/3$, and the light-gray regions represent the error bars of the simulations. The red, blue, and green points correspond to different binnings, indicated in the legends. Locations of the $\beta = 1$ and $\beta = 1.7$ noise are also displayed for reference. (l) Separation of FSRQs and BL Lacs in the $\mathcal{A}$–$\mathcal{T}$ plane. The FSRQs are denoted with cold colors, while BL Lacs with warm ones. Note a different color-coding than in panels (a)–(k). The vertical dashed line marks the rough separation. The outlier, B2 1633+38 in a 14 day binning, is indicated with an arrow. The magenta line is the PLC with $\beta = 1$ and increasing Poisson level, starting from $C = 0$.

−304, with LSP and the Date Compensated Discrete Fourier Transform methods, finding a QPO with a period of 650 days in the 0.1–300 GeV energy range. Afterwards, Sandrinelli et al. (2016) investigated similar data of six blazars, including 3C 279, PKS 1510−089, and PKS 2155−304, using LSPs. All objects showed QPOs in HE γ-ray LCs, at periods of 24 and 39 days with 3σ significance in the case of 3C 279, 115 days with 2.58σ for PKS 1510−089, as well as 642 days (3σ), and 52 and 61 days (2.58σ) for PKS 2155−304. Sandrinelli et al. (2017) studied optical and MSL Fermi-LAT data of three blazars, i.e., BL Lac, Mrk 421, and PKS 0716+714, using LSP and claiming no QPOs with significance $>3\sigma$. Zhang et al. (2017a)

generated 8 yr long Fermi-LAT LCs of PKS 2155−304 using two methods: the maximum likelihood optimization and the exposure-weighted aperture photometry. The authors searched for QPOs with LSP and WWZ methods, finding a QPO with the period of ∼635 days at the ∼4.9σ significance level, thus confirming the QPO period found by Sandrinelli et al. (2014, 2016). We also confirm this QPO at the 3σ significance level, finding a period of 612 ± 42 days, consistent with a linear decrease of its value over the years.

The 7 yr long LCs of Mrk 421, PKS 1510–089, and B2 1520 +31 were generated with the unbinned likelihood analysis method by Gupta et al. (2019), and then QPOs were searched for by applying LSP and WWZ techniques. A quasi-periodic signal was found only for B2 1520+31, with a period of ∼71 days with >3σ significance. We did not obtain any peculiar structures in the scalograms for this source. Covino et al. (2019) studied long-term (∼decade) MSL Fermi-LAT LCs, including PKS 0716+714 and PKS 2155−304, finding no QPOs at a 3σ significance level as well.

Bhatta (2019) generated a 10 yr long Fermi-LAT LC, using unbinned likelihood analysis. The LC was analyzed with the LSP and WWZ, showing a QPO with a period of ∼330 days, reaching a significance of 2.58σ. We did not observe any signs of this QPO at a 3σ level in the scalograms, though. Likewise, we did not confirm the QPOs in Mrk 421 and PKS 0716+714, reported by Bhatta & Dhital (2020) on a <4σ level.

Otero-Santos et al. (2020) analyzed the 11 yr long Fermi-LAT LC of B2 1633+38, generated with unbinned likelihood analysis, using three different techniques: the Discrete Correlation Function (DCF), LSP, and WWZ. They found a hint of QPOs with periods of 639 and 646 days at the 2σ level, with the WWZ and LSP methods, respectively, as well as a more significant QPO at 3σ–4σ having a period of 581 days with DCF. We obtained a peculiar structure in the scalograms of this blazar, evolving from $P \sim 500$ days to $P > 1000$ days over the course of the LC, with 3σ significance.

Discrepancies with previous analyses—Covino et al. (2019) analyzed blazars' LCs generated by the Fermi-LAT team with the aperture photometry method, available on the LAT 3FGL Catalog Aperture Photometry Lightcurves webpage.[23] These LCs constitute a quick-look facility to easily scan for interesting features in the data. At the same time, it is strongly discouraged to use this data directly for detailed scientific analysis, as the LCs can contain the emission from nearby sources. Also the fluxes may be affected by the background emission (point-like and/or diffuse). Similarly, Nakagawa & Mori (2013), Sandrinelli et al. (2014, 2016, 2017), Castignani et al. (2017), and Ryan et al. (2019) studied the LCs accessible on the Monitored Source List Light Curves webpage[24] provided by the Fermi Science Support Center. Here again, the LCs are generated in an automatic way, using preliminary calibration and instrument response functions, to help search for flares in the data and plan the follow-up analysis in other bands. It is not recommended to use this data in scientific analysis as well.

Various authors adopted different significance levels to assert the significance of QPO detections, ranging from $\lesssim 2\sigma$, through arbitrary values like 95% or 99%, rarely exceeding 3σ (99.73%). For example, Bhatta (2019) was the first to try to look for possible QPOs in the Fermi-LAT data of Mrk 501, finding a QPO with a period of ∼330 days. This is a very interesting result, which, however, needs to be further verified, because this possible QPO was reported only on a 2.58σ significance level. Moreover, Gupta et al. (2019) claimed a QPO detection in B2 1520+31 merely on a 1.96σ level. The correct methodology is to set a goal, e.g., for finding a signal on a given significance level (though one that warrants a detection, i.e., at least >3σ) and not report just any detected feature (especially with low significance). Moreover, sometimes a false-alarm probability is reported (Sandrinelli et al. 2014) or used to set the significance (Gupta et al. 2019). This, however, tests a peak in the periodogram against a white-noise model (VanderPlas 2018), while blazars exhibit PL-like PSDs, hence peaks exceeding the 3σ level against white noise will usually not be significant when tested against colored noise. Another issue is an abuse of the wavelet scalogram: while this is a powerful tool sensitive to transient phenomena in a time series, and therefore ideal to search for QPOs in blazar LCs, it is often used—with the significance asserted—as a global periodogram, like an LSP with which it is often highly consistent (Zhang et al. 2017a, 2017b). A global periodogram is an average of the power at a given frequency among the whole LC. As was demonstrated in Section 5.3, a scalogram can reveal that an apparently statistically significant peak in a global periodogram can signal a spurious quasi-periodicity, which is not supported when looking at how the power among different frequencies is distributed in time. Unfortunately, in many works, the scalogram is merely displayed, without performing any significance estimation (Zhang et al. 2017a, 2017b; Bhatta 2019; Gupta et al. 2019; Otero-Santos et al. 2020) or even displaying the COI. We performed here such an estimation that allowed us to conclude that any quasi-periodicity in our sample that might be claimed based on the global periodogram is spurious. While in some instances the scalogram is very convincing, e.g., in the case of PG 1553 +113 (Ackermann et al. 2015), still a significance analysis of its local features, not only global ones, is required. Finally, we stress again that a QPO, when present in the data, is not necessarily a signature of any periodic phenomenon occurring in the system. Hence attributing a significant, constant period obtained from a global periodogram, with a true periodicity is in our opinion unjustified. Indeed, the peaks observed in an LC can be spaced very nonuniformly; therefore, a visual inspection of the LC for the presence of equidistant peaks can be misleading.

ARMA—The only attempt, to the best of our knowledge, to analyze γ-ray Fermi-LAT data with an ARMA(p, q) model is the case of a BL Lac−type object PKS 0301−243, located at $z = 0.266$, using a 30 day binned LC (Zhang et al. 2017b). Fitting returned (3, 2) as the order, meaning that three previous observations affect any given flux value in the LC. This implies a characteristic timescale of $\tau_{\rm rest} = 71$ days, which is substantially greater compared to our results. This is intriguing, because it suggests that such a timescale might differ among different blazars. Adding this source to B2 1633+38, PKS 0716+714, PKS 2155−304, and B2 1520+31 produces a lack of correlation between $\log M_{\rm BH}$ and $\tau_{\rm rest}$ ($M_{\rm BH} = 8 \times 10^8\, M_\odot$ of PKS 0301−243 taken from Ghisellini et al. 2010). When $\tau_{\rm rest}$ is calculated for all 11 of our blazars, with the best-fit orders for the 7 day binning, no correlation with $M_{\rm BH}$ can be inferred either. It appears that the BH mass is not a

[23] https://fermi.gsfc.nasa.gov/ssc/data/access/lat/4yr_catalog/ap_lcs.php
[24] https://fermi.gsfc.nasa.gov/ssc/data/access/lat/msl_lc/

crucial parameter in influencing the values of $\tau_{\rm rest}$. Further research on a bigger sample is therefore necessary for assessing the meaningfulness of such timescale regarding its physical origin.

It is worth mentioning that the 22 and 37 GHz LCs of 3C 279 and 3C 454.3 were fitted with the ARIMA(p, d, q) models (Bewketu Belete et al. 2019), resulting in $d = 1$ (i.e., once differenced to ensure stationarity), with $(p, q) = (1, 1)$ for 3C 279, and (5, 1), (1, 2) for 3C 454.3 at 22 and 37 GHz, respectively. The fits are slightly inadequate, and hence suggest that long-term memory processes (FARIMA/CARFIMA) might be a better model. The correlation between radio and γ-ray bands (Angelakis et al. 2019 and references therein) implies a common emission site, hence a multiwavelength approach to $\tau_{\rm rest}$ might provide additional constraints on the radiation mechanism.

CARMA—Ryan et al. (2019) analyzed γ-ray LCs of eight blazars common to our sample in 1 and 7 day binning, with the CARMA models. For two sources they obtained the same (1, 0) orders as we did (with the 7 day binning), and constrained the break timescales $T_{\rm break}$ of their Lorentzian PSDs. Those are Mrk 421 with $T_{\rm break} = 389^{+502}_{-107}$ days, and PKS 1510−089 with $T_{\rm break} = 186^{+89}_{-31}$ days. We obtain (389 ± 107) days and (209 ± 24) days, respectively, which is in agreement within the errors.

For B2 1520+31, in turn, both Ryan et al. (2019) and we arrived at CARMA(2, 1) as the best fit. The break timescales, corresponding to the widths of the zero-centered Lorentzians that the PSD is composed of, are >1230 days and 68^{+18}_{-27} days (Ryan et al. 2019), which are in agreement with our results, (3075 ± 961) days and (102 ± 33) days.

We also calculated the $T_{\rm break}$ of the CARMA(1, 0) models of all objects in our sample and compared them with values given by Ryan et al. (2019). Both sets are consistent within errors.

Hurst exponents—The Hurst exponents of blazar LCs have been computed for optical data of blazar candidates behind Magellanic Clouds (Żywucka et al. 2020), with a much more irregular sampling than the γ-ray observations utilized herein. It was found that in most instances $H < 0.5$, contrary to the γ-ray case. While this might suggest that optical and γ-ray emission are governed by different processes, or with different parameters, the computation of Hurst exponents is a delicate matter, and especially with short-term data needs to be done with caution (Katsev & L'Heureux 2003). The most straightforward approach is to analyze the time series with a greater number of points, which can be achieved in the case of Fermi-LAT data by using a smaller binning for the LCs.

The $\mathcal{A}$–$\mathcal{T}$ plane—Likewise, the separation of FSRQ and BL Lac γ-ray LCs in the $\mathcal{A}$–$\mathcal{T}$ plane is a novel finding; however it is supported by the separation observed using optical LCs of blazar candidates behind Magellanic Clouds (Żywucka et al. 2020). Therefore, both optical and γ-ray observations, with very different sampling, suggest that there are intrinsically different variability patterns between different types of blazars.

6.3. Interpretation and Context

There has not been a unified procedure in the literature for detecting QPOs in astronomical data: various methods have been used to produce the PSDs, and no consistent significance level has been adopted (see Table 1 and Section 6.2). We performed a homogeneous investigation (similar in spirit to Covino et al. 2019) of wavelet scalograms, confirmed the QPO in PKS 2155−304, with a period of ∼610 days in the 7 day binned LC, but detected only a dubious quasi-periodicity just above the 3σ level in the global wavelet periodogram of PKS 1830−211 (only in the 7 day binned LC, though). We stress the importance of the subtle meaning of the term "quasi" while interpreting any such detection: a QPO need not be inherently linked to any periodic behavior of the system. In fact, it is a well-known fact that red-noise-type processes often resemble QPOs for a few cycles (Vaughan et al. 2016; Ait Benkhali et al. 2020) and that detections reported so far were only on QPOs lasting four to six cycles. X-ray data, despite a much finer sampling of LCs, usually span relatively short periods (compared to optical or γ-ray LCs), and the number of cycles reported is also not high (e.g., Lachowicz et al. 2009). Hence, a QPO, usually understood as a transient phenomenon with a Lorentzian feature in the PSD, is very likely to be a manifestation of correlations governing the variability inherent, e.g., in ARMA or CARMA models. Such correlations may be the result of stochastically occurring disruptions in the relativistic jet itself or the accretion disk coupled to the jet. QPO signatures might come from jet wobbling, its precession and nutation, peculiar plasma injections into the jet, or interaction of the jet with ambient medium (Caproni et al. 2004; Bosch-Ramon et al. 2012; Britzen et al. 2018; Lico et al. 2020). One cannot also exclude the possibility that nonlinear physical processes (e.g., intermittency; Garcia & Theodorsen 2017a, 2017b) lead naturally to coupling that results in such features or that a combination of all the above effects occurs, with various relative strengths in different AGNs. Finally, a binary SMBH system is often invoked as a driving mechanism for the QPOs, but such systems must be too rare to be a universal explanation (Holgado et al. 2018).

The generating mechanism for QPOs has thus not been unambiguously identified. It is therefore not clear whether QPOs are an inherent property of γ-ray emission of blazars, and that it is just the difficulty of its detection or insufficient data that make them so rare and elusive. On the other hand, the general shape of the PSD has also not been convincingly derived so far. Finke & Becker (2014, 2015) considered synchrotron self-Compton (SSC) and external Compton (EC) as models for the emission, including Klein–Nishina effects. They modeled the evolution of nonthermal plasma with an assumption of PL injection rate to the jet that lead to a PL form of the PSD as well. In particular, a broken PL with low- and high-frequency indices β and $\beta + 2$ was obtained, and the break frequency might be associated with the electron escape timescale. Recall that we do not observe a break in either Fourier spectra or LSPs for any object. On the other hand, we obtained some clear breaks by fitting ARMA and CARMA models, reaching consistent values of a few hundred days with both methods. It is curious to note that similar timescales (100–400 days) were obtained with the LSP for a sample of optical LCs of the FSRQ candidates behind the Magellanic Clouds (Żywucka et al. 2020). A rotating helical structure can be formed in the jet due to it being tied to the rotating BH or accretion disk (Raiteri et al. 2013). The evolving viewing angle may alter the observed flux, even though the total emitted flux remains constant. Different parts of the jet can attain different orientations in time, thus leading to a complex flux variability. These effects might be the origin of the PL-like shape of blazar PSDs.

Kaulakys et al. (2006) derived a stochastic differential equation whose solutions yield a PL PSD. Unfortunately, this cannot constitute a model for blazar variability, as these solutions also exhibit a PL distribution of the signal intensity, while the PDFs of observed fluxes are lognormal (Section 2.2). CARMA models, on the other hand, being Gaussian processes, are good candidates for modeling the logarithmic flux variations, and their PSDs are flexible enough to incorporate nearly pure PL, broken PL, and QPOs. The defining Equation (38), however, needs to be directly connected to physical properties of the system. Up to now, only the simplest cases were given a heuristic interpretation in terms of, e.g., some characteristic timescales in the jet and disk, or related to BH mass (Moreno et al. 2019; Ryan et al. 2019). CARMA processes with low orders, (1, 0) and (2, 1), are in turn easily associated with simple physical models, i.e., the OU process and damped harmonic oscillator (Kasliwal et al. 2017). This is, however, an inverse-engineering approach, as it is desired to derive the equations from first principles, not to associate observed features with some parameters of phenomenological models. Identification of physical processes occurring in the emission region (SSC, EC, etc.; Finke & Becker 2014, 2015; Chen et al. 2016) with a justified injection rate is one possible direction to pursue. In particular, the particle-in-cells (PIC) simulations (Sironi et al. 2013) suggest that the injection rate's dependence on the Lorentz factor is not necessarily a PL. The PIC simulations are based on microturbulence occurring in the jet shocks. In turn, Narayan & Piran (2012) considered a jets-in-a-jet model, in which turbulence in the jet fluid gives rise to relativistic random motion in different directions in different subregions of the jet. The sum of the flux contributions from each subregion produces the observed variability. The distribution of the Doppler beaming factors adds to the observed PSD. This model works well for PKS 2155−304 under sufficiently strong magnetization of the medium, although it again shifts the question: what causes the turbulence, and what are its properties?

As the presence of a QPO in CARMA (and also ARMA) processes of a given order (p, q) depends on the AR and MA coefficients, it may be possible to identify the broader class of physical processes that generate the variations in the LCs, i.e., to describe the variability by means of some (stochastic) differential equation, in which the coefficients depend on physical parameters of the system. If so, one might recognize which of the physical parameters (e.g., magnetic fields, density of the ambient medium, viscosity of the disk, etc.) govern the steepness of the PSD, whether it contains a break or a QPO, and their corresponding timescales. In particular, the fact that in some objects we observe lower orders p of fitted ARMA(p, q) models for LCs with a higher binning hints at a characteristic timescale above which the observations become less correlated. Indeed, our ARMA fits suggest that the state of the γ-emitting region affects future measurements for a few weeks. Zhang et al. (2017b) considered a 9 yr long LC (30 day binning) of the BL Lac object PKS 0301−243. They fitted an ARMA(3, 2) process, a relatively high order, implying a characteristic rest-frame timescale of ∼71 days. On the other hand, the relation between order p and binning is not present when fitting CARMA models—in fact, for B2 1520+31, we even obtained the opposite dependence. Overall, all of the CARMA fits are low order, and higher orders appear as a result of overfitting to account for variations below the Poisson noise level. Therefore, whether such timescales, inferred directly from temporal data, are of any meaning is yet to be determined.

In the case of Fourier spectra and LSPs, the PL and PLC fits were performed to binned PSDs, hence there are relatively few points for the fitting algorithm. In PL and PLC, there is by definition no break. As mentioned in Section 5.1, an attempt to model the binned PSDs with a smoothly broken PL was ruled out in all cases, likely owing to the small number of points. On the other hand, ARMA and CARMA models are fitted to the points in the LC, so there are many more points available; second, the PSDs of these processes by definition have a break since they contain a Lorentzian around $f \sim 0$. The ARMA and CARMA fits are therefore more sensitive to detecting a break —i.e., the break will always be present, but (i) it may be located at very low frequencies, related to the length of the time series, so not physical (and practically not detectable), or (ii) be not well constrained in the sense of having a large uncertainty, including within the errors frequencies corresponding to the length of the time series. This is most prominent in the case of B2 1520+31 (Table 6) or Mrk 501 (Table 7).

Overall, we note that the utilized methods to model the PSDs (PL fits to Fourier spectra and LSP; ARMA and CARMA modeling) returned outcomes quite similar in shape among the examined blazars. One can see in Tables 2 and 4 that sources with a significant contamination of Poisson noise (Mrk 501 and TXS 0506+056, which are the dimmest among the examined herein) yield steeper PSDs, although β falls roughly in the range of ∼1–2 for our sample. CARMA models and Hurst exponents are all consistent with each other among our objects. This leads to an observation that the population of blazars is an ensemble, i.e., it suggests that each blazar should be treated as a different realization of the same underlying process, taking into account the unequivocal differentiation into two classes, FSRQs and BL Lacs, also visible clearly in the $\mathcal{A}$–$\mathcal{T}$ plane. Hence, a population synthesis study of blazars will likely shed light on the nature of the variability from a global perspective.

Moreover, $H > 0.5$, obtained in most instances, suggests that the presence of persistence in modeling the variability should be accounted for. In discrete models, FARIMA is a generalization of ARMA that, through a fractional differencing parameter d, allows for $H \neq 0.5$. Likewise, a CARFIMA process (Tsai & Chan 2005; Tsai 2009; Feigelson et al. 2018) is a candidate description for the blazar variability, whose advantages are both its inherent continuity and long-term memory. Here, too, the reservations about the interpretation of CARMA models hold, i.e., it is desired to connect the AR and MA coefficients, as well as d, to some physically meaningful properties of the blazar. We generally see in Figure 20 that $H \gtrsim 0.8$ (sometimes spilling to $H \lesssim 0.2$ due to the discontinuity at the fBm–fGn border; see Figure 6), except for 3C 454.3, which prefers $H \lesssim 0.5$, consistent with PL indices from Tables 2 and 4. This, on one hand, suggests that the processes governing blazar emission are inherently described by high values of H, but on the other hand, it requires an explanation for the unusual, compared to other objects in our sample, behavior of 3C 454.3

Finally, the sharp separation of FSRQs and BL Lacs in the $\mathcal{A}$–$\mathcal{T}$ plane suggests that either the processes governing the variability are different between the two classes or are qualitatively different realizations of the same physical scenario. We stress that this separation is not trivially connected with FSRQs having steeper PSDs, as the $\beta \lesseqgtr 1$

division in the $\mathcal{A}$–$\mathcal{T}$ plane does not divide the classes at all. That the separation is meaningful is supported by a recent finding that FSRQ and BL Lac blazar candidates observed behind Magellanic Clouds also occupy distinct regions of the $\mathcal{A}$–$\mathcal{T}$ plane (Żywucka et al. 2020). This finding can therefore serve as an additional tool in classifying blazars, in particular when spectroscopy is not feasible.

6.4. Possible Applications

The methodology employed herein to study blazar LCs consists of various time series analysis techniques and hence is applicable to any temporally (or spatially) ordered data. Below we list some of the potentially interesting applications.

1. Multiwavelength analysis of blazar LCs. We examined herein the γ-ray data from Fermi-LAT, but some of the methods (LSPs, Hurst exponents, the $\mathcal{A}$–$\mathcal{T}$ plane) were already applied to optical LCs of blazar candidates behind the Magellanic Clouds (Żywucka et al. 2020), observed by OGLE. Also, the densely sampled optical LCs (e.g., Smith et al. 2018) or X-ray data (e.g., Gaur et al. 2018) are a promising target for such investigations.
2. Likewise other AGN types, e.g., Seyfert galaxies (Gallo et al. 2018), radio galaxies (Marshall et al. 2009), or quasars, including the search for QPOs (Li et al. 2010) in various energy bands. Moreover, the characteristic features as well as differences between jetted and nonjetted AGNs can be studied (e.g., Padovani et al. 2017; Padovani 2017).
3. X-ray binaries exhibit broadband PSDs (Bayless et al. 2011), whose shape can be constrained with several techniques, complementing each other, including modeling the LCs with Gaussian stochastic processes. Moreover, chaotic modulation is also a considered possibility (Mannattil et al. 2016; Suková et al. 2016; Phillipson et al. 2018) that further validates the use of nonstandard, in particular nonlinear, tools of time series analysis.
4. Pulsar spin-down rates can be erratic, or even chaotic (Seymour & Lorimer 2013). One might expect that persistence analysis via Hurst exponents will lead to insights on the properties of the processes governing the spin-down of the periodic pulsation.
5. Gamma-ray bursts (GRBs). The Hurst exponents were already shown to differ for short and long GRBs (MacLachlan et al. 2013; Tarnopolski 2015a). The $\mathcal{A}$–$\mathcal{T}$ plane, operating exclusively in the time domain, might be an insightful addition to other methods, e.g., the minimum variability timescale (Golkhou & Butler 2014), in classifying the prompt LCs. Therefore, it will possibly allow a meaningful inference of the number of classes, i.e., rejecting or supporting the existence of the elusive GRB group with intermediate durations (see Tarnopolski 2019b for an overview of this issue). The PSDs of individual GRBs were also already analyzed with PL models, and it was found that they exhibit high PL indices, $1 \lesssim \beta \lesssim 6$, which are anticorrelated with peak energy (Dichiara et al. 2016; Guidorzi et al. 2016). QPOs in prompt LCs remain undetected (Dichiara et al. 2013).
6. Variable stars, e.g., of the T Tauri type, which are young, pre-main-sequence stars that exhibit significant variability in all wavelength bands, but also spectral and polarization changes, and are surrounded by protoplanetary accretion disks (Appenzeller & Mundt 1989). Their long-term, densely sampled LCs (Rigon et al. 2017) could be modeled with CARMA processes. Their different subtypes may be classified in the $\mathcal{A}$–$\mathcal{T}$ plane as well as with the Hurst exponents. Typical quasi-periodic variations on the order of days make them interesting targets for the time-series analysis techniques employed herein, especially for searching QPOs with wavelet scalograms, likewise in the case of, e.g., sdB stars exhibiting stochastic pulsations (Østensen et al. 2014).
7. The $\mathcal{A}$–$\mathcal{T}$ plane of densely sampled optical spectroscopic observations of binary and multiple stellar systems (e.g., Dimitrov et al. 2018), covering the entire cycle phases, could help to distinguish these systems from single stars.
8. The X-ray flickering of cataclysmic variables yields $H > 0.5$ (Anzolin et al. 2010). However, the employed R/S method was demonstrated herein to be strongly biased; therefore, a reanalysis of the XMM-Newton LCs with a variety of H estimation techniques, in order to establish consistency, is desired.
9. Extrasolar planets manifest their existence in optical data by, e.g., small changes in the LCs of the stellar–planetary systems that can be detected by transient and/or gravitational microlensing methods (e.g., Seager & Mallén-Ornelas 2003; Bond et al. 2004). A planet search algorithm utilizing ARIMA models has already been proven to be effective (Caceres et al. 2019). Moreover, the locations in the $\mathcal{A}$–$\mathcal{T}$ plane, estimated based on properly sampled data sets, could assist in detections of new extrasolar planets.
10. Sunspots have been investigated with ARMA models, in particular to formulate predictions on the solar cycle (Brajša et al. 2009), although recently a neural network approach has been utilized more often (Liu et al. 2019a). Forecasts based on estimated Hurst exponents were also performed (Pesnell 2012). In regard to solar physics, solar wind proton density fluctuations are characterized by $H \sim 0.8$, placing constraints on the models of kinetic turbulence (Carbone et al. 2018). Moreover, the solar radio emission[25] variability is perfect for such analyses and might provide useful insights into the solar dynamics.
11. The background emission, e.g., in X-rays in the case of XMM-Newton, consists of several components, i.e., electronic readout noise, HE particles, particle-induced X-rays generated inside the camera, and thermal CCD noise (Nevalainen et al. 2005). Estimation of the statistical properties of the blank-sky background is crucial in properly extracting the signal of interest.
12. While magnetically arrested disks (Narayan et al. 2003; Tchekhovskoy 2015) and those with standard and normal evolution accretion flow (Narayan et al. 2012) have similar spectral density distributions (Xie & Zdziarski 2019), it is a question whether these two states can be distinguished in the time domain, e.g., by analyzing numerically computed accretion rates or the magnetic flux with the presented time series analysis tools.
13. The recently released gravitational wave data (The LIGO Scientific Collaboration et al. 2019), in the form of

[25] http://www.oa.uj.edu.pl/slonce/index.html

densely sampled strain time series, are a tempting target for various analyses, like the ones performed herein.

14. Time-dependent magnetohydrodynamic numerical simulations of the stellar interior (Merkin et al. 2016), resulting in the time series of, e.g., magnetic field or plasma density, are tempting applications for a variety of methods of time-series analysis. The spatial evolution of relativistic jet properties is also subject to such analyses, as time series need not be ordered in time only. The subtle variations along the jet might shed light on GRB or AGN physics as well (Huarte-Espinosa et al. 2011; Sironi et al. 2013).
15. Observations in the extremely low-frequency (ELF) regime of electromagnetic waves. Long-term observations of natural electromagnetic fields in the ELF range (0.03–300 Hz) are conducted by several ELF stations all over the world.[26] The PSD analysis of ELF data reveals several resonances in the Earth-ionosphere cavity: the Schumann resonances, which are the global electromagnetic resonances in the Earth-ionosphere waveguide, generated and excited by lightning discharges over the world (Kułak et al. 2006; Nieckarz et al. 2009); and ionospheric Alfvén resonances, caused by magnetic waves trapped between different layers of the ionosphere (Odzimek et al. 2006). The measured ELF variations of the magnetic field contain colored stochastic noise, which can be modeled by ARMA/CARMA processes as well.
16. It is well known that many problems in celestial mechanics, like the three-body problem or the stability of the solar system, are chaotic in its nature. Centaurs—a transient population of small bodies at the outskirts of the solar system—have chaotic orbits whose evolution resembles different types of stochastic processes. These types can be distinguished using the Hurst exponents (Bailey & Malhotra 2009). Whether techniques stemming from stochastic analysis can provide even further insight into the dynamics of solar and extraterrestrial systems is an interesting open problem.

7. Conclusions

1. From extensive MC testing, we found that parametric modeling gives unreliable results. In particular, retrieval of the PL index of the PSD, β, yields a wide range of outcomes for different realizations of the same underlying stochastic process, and similarly, the dispersion of the parameters of autoregressive models is high. Likewise, the Hurst exponent values returned by different algorithms can in principle be inconsistent. We therefore recommend simultaneously employing various algorithms and examining the consistency of the obtained estimates, as well as performing MC simulations, e.g., bootstrapping the LC within the measurements' uncertainties or resorting to Bayesian methods.
2. Due to the very consistent PSD properties of blazars in our sample, we suggest that each object can be treated as one realization of a common stochastic process underlying the observed variability. Therefore, the population of blazars (although possibly differentiated into FSRQs and BL Lacs) should be treated as an ensemble, allowing for a more global insight into the governing mechanisms driving the variability.
3. Orders of the ARMA models, fitted for different LC bins, hint at some characteristic dissipation timescale, after which the disturbances in the emitting region stop affecting the emission significantly.
4. ARMA and CARMA models imply the existence of a break in the PSDs at timescales of ∼hundreds of days.
5. In a majority of cases, the Hurst exponents are greater than 0.5, indicating the presence of long-term memory in the systems, except for 3C 454.3, which yields $H < 0.5$. Stochastic processes that allow persistence are therefore promising candidates for modeling blazar LCs.
6. We confirm the presence of a QPO in PKS 2155−304, with a period of 612 ± 42 days. We detect a peculiar structure in the scalogram of B2 1633+38, at periods of ∼600–1000 days, and a candidate QPO in PKS 0716 +714 at a period of >1000 days. However, we do not detect any QPOs in the remaining sources; in particular, we do not confirm the QPOs in Mrk 501, Mrk 421, PKS 1510−089, 3C 279, and B2 1520+31.
7. We confirmed a proposition, initially put forward based on optical data of blazar candidates (Żywucka et al. 2020), that FSRQs and BL Lacs are separated in the $\mathcal{A}$–$\mathcal{T}$ plane, i.e., they can be distinguished based on the LCs only.

M.T. acknowledges support by the Polish National Science Center (NSC) through OPUS grant No. 2017/25/B/ST9/01208. The work of N.Ż. is supported by the South African Research Chairs Initiative (grant No. 64789) of the Department of Science and Innovation and the National Research Foundation[27] of South Africa. V.M. is supported by NSC grant No. 2016/22/E/ST9/00061. J.P.-G. acknowledges financial support from the State Agency for Research of the Spanish MCIU through the "Center of Excellence Severo Ochoa" award to the Instituto de Astrofísica de Andalucía (SEV-2017-0709) and from Spanish public funds for research under project ESP2017-87676-C5-5-R.

Software: MATHEMATICA (Wolfram Research 2016), R (R Core Team 2016, http://www.R-project.org), CARMA_PACK (Kelly et al. 2014, https://github.com/bckelly80/carma_pack), WAVEPAL (Lenoir & Crucifix 2018a, 2018b, https://github.com/guillaumelenoir/WAVEPAL), MATLAB (Mathworks Inc. 2010).

Appendix A
Maximum Likelihood Estimation of ARMA and FARIMA

The benchmark testing for fitting ARMA and FARIMA processes from Section 4.3 was repeated in R in order to utilize a different computer system, implementation, algorithm, and method. Time series were simulated with `arima.sim` and `fracdiff.sim`. The commands `auto.arima` and `arfima`, with the maximum likelihood method (`method = "ML"`), were used for the fitting. The results are displayed in Figure A1.

[26] In particular, by the World ELF Radiolocation Array (WERA) project (http://oa.uj.edu.pl/elf), which consists of three ELF stations located in Poland, Argentina and USA (Kulak et al. 2014; Mlynarczyk et al. 2017) that measure continuously with a sampling frequency of ∼1 kHz.

[27] Any opinion, finding, and conclusion or recommendation expressed in this material is that of the authors and the NRF does not accept any liability in this regard.

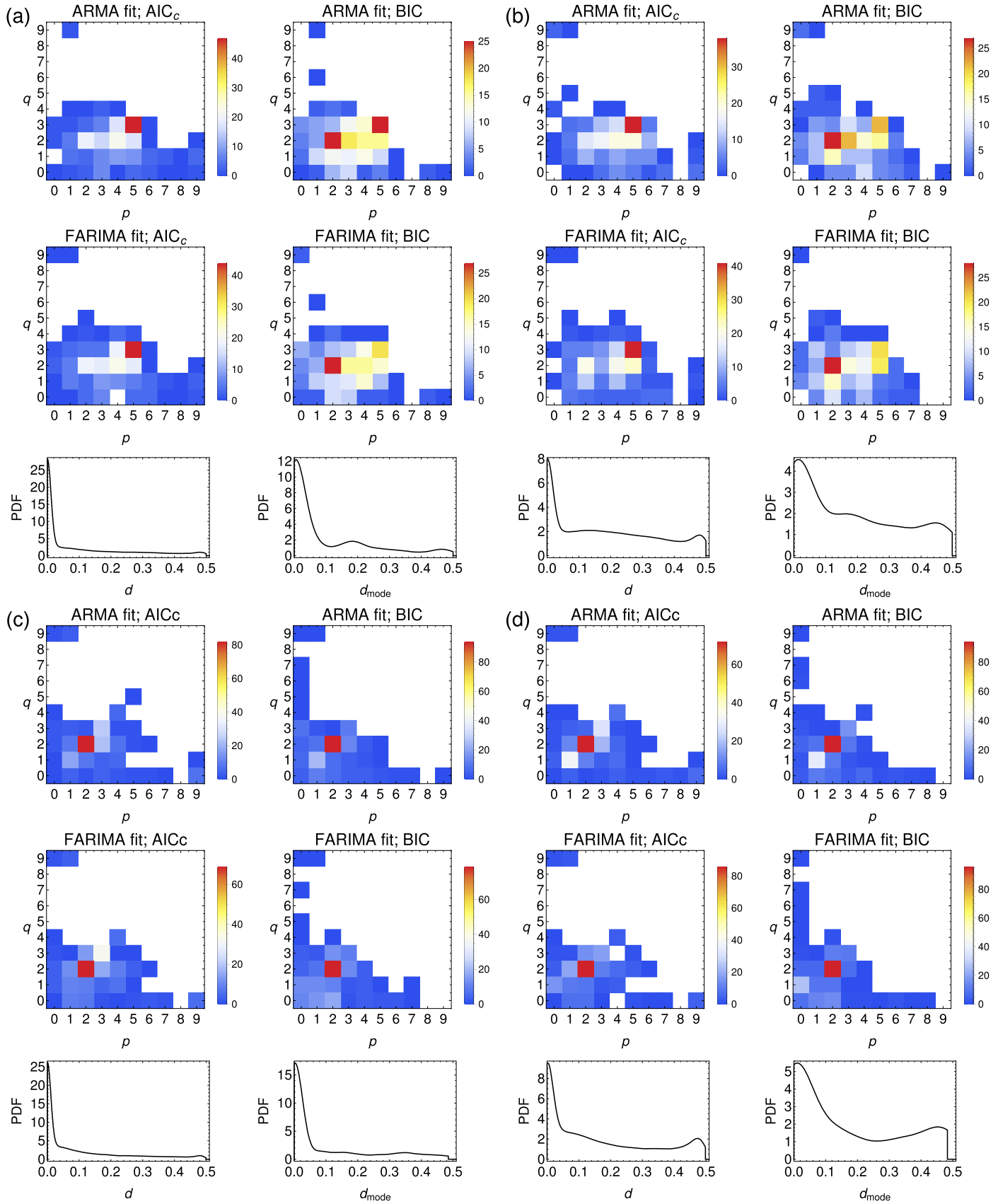

Figure A1. Same as Figure 11, but fitted with R.

Appendix B
Implementations of the Codes

1. Fourier spectra and LSPs: they were computed in MATHEMATICA by directly implementing the methodology from Sections 3.1 (employing the command `Fourier`[28] with default `FourierParameters`) and 3.2 (Equations (14) and (15)). To bin the raw PSDs, the function `BinListsBy`[29] was utilized. Fits to the binned PSDs (in log–log scale) were done with `NonlinearModelFit`.[30]
2. WAVEPAL: the scalograms were computed using the function `Wavepal.plot_scalogram`, with the 99.73rd percentile for the 3σ confidence level. Before calculating the scalograms, the LCs were detrended by the polynomial trend of degree $n = 7$ using the function `Wavepal.choose_trend_degree`.
3. ARMA: the best fit was obtained using MATHEMATICA with[31] `TimeSeriesModelFit[data, {"ARMA", {p, q}}]` by iterating over `p` and `q`, and choosing according to the BIC. The confidence intervals of the resulting PSD were inferred by bootstrapping with the best-fit parameters' standard errors. So were the uncertainties of f_0 and the breaks obtained.
4. CARMA: the maximum likelihood estimates for AIC_c were computed using the function `CarmaModel.choose_order`, and then the values of AIC_c were recalculated to BIC for further estimation of (p, q) order. The MCMC sampler was run using `CarmaModel.run_mcmc` for 150,000 iterations, with the first 50,000 of those discarded as burn in. To check the chain convergence, we used the multiple-chain convergence diagnostics (Gelman & Rubin 1992) implemented in the PyMC Python module[32] by the function `pymc.gelman_rubin`.
5. Hurst exponents and $\mathcal{A}$–$\mathcal{T}$ plane: the MATHEMATICA implementations are available at https://github.com/mariusz-tarnopolski/Hurst-exponent-and-A-T-plane.

ORCID iDs

Mariusz Tarnopolski https://orcid.org/0000-0003-4666-0154
Natalia Żywucka https://orcid.org/0000-0003-2644-6441
Volodymyr Marchenko https://orcid.org/0000-0002-7175-1923
Javier Pascual-Granado https://orcid.org/0000-0003-0139-6951

References

Abdo, A. A., Ackermann, M., Agudo, I., et al. 2010a, ApJ, 721, 1425
Abdo, A. A., Ackermann, M., Ajello, M., et al. 2009, ApJ, 700, 597
Abdo, A. A., Ackermann, M., Ajello, M., et al. 2010b, ApJ, 715, 429
Abdo, A. A., Ackermann, M., Ajello, M., et al. 2010c, ApJ, 722, 520
Abdo, A. A., Ackermann, M., Ajello, M., et al. 2011, ApJL, 733, L26
Abdo, A. A., Ackermann, M., Ajello, M., et al. 2015, ApJ, 799, 143
Abdollahi, S., Acero, F., Ackermann, M., et al. 2020, ApJS, 247, 33
Abramowicz, M. A., Kluźniak, W., McClintock, J. E., & Remillard, R. A. 2004, ApJL, 609, L63
Abry, P., Flandrin, P., Taqqu, M. S., & Veitch, D. 2000, in Wavelets for the Analysis, Estimation, and Synthesis of Scaling Data, ed. K. Park & W. Willinger (Chichester: Wiley), 39
Ackermann, M., Ajello, M., Albert, A., et al. 2015, ApJL, 813, L41
Ackermann, M., Anantua, R., Asano, K., et al. 2016, ApJL, 824, L20
Addison, P. S. 2002, The Illustrated Wavelet Transform Handbook (1st ed.; Bristol: IOPP)
Aharonian, F., Akhperjanian, A. G., Aye, K. M., et al. 2005, A&A, 430, 865
Ahnen, M. L., Ansoldi, S., Antonelli, L. A., et al. 2016, A&A, 593, A91
Ait Benkhali, F., Hofmann, W., Rieger, F. M., & Chakraborty, N. 2020, A&A, 634, A120
Akaike, H. 1974, ITAC, 19, 716
Akiyama, K., Stawarz, Ł., Tanaka, Y. T., et al. 2016, ApJL, 823, L26
Aleksić, J., Ansoldi, S., Antonelli, L. A., et al. 2014, A&A, 569, A46
Aleksić, J., Ansoldi, S., Antonelli, L. A., et al. 2015, A&A, 578, A22
Algaba, J.-C., Lee, S.-S., Rani, B., et al. 2018, ApJ, 859, 128
Angel, J. R. P., & Stockman, H. S. 1980, ARA&A, 18, 321
Angelakis, E., Fuhrmann, L., Myserlis, I., et al. 2019, A&A, 626, A60
Ansoldi, S., Antonelli, L. A., Arcaro, C., et al. 2018, ApJL, 863, L10
Anzolin, G., Tamburini, F., de Martino, D., & Bianchini, A. 2010, A&A, 519, A69
Appenzeller, I., & Mundt, R. 1989, A&ARv, 1, 291
Asano, K., & Hayashida, M. 2015, ApJL, 808, L18
Atwood, W. B., Abdo, A. A., Ackermann, M., et al. 2009, ApJ, 697, 1071
Atwood, W. B., Bagagli, R., Baldini, L., et al. 2007, APh, 28, 422
Bailey, B. L., & Malhotra, R. 2009, Icar, 203, 155
Barthel, P. D., Conway, J. E., Myers, S. T., Pearson, T. J., & Readhead, A. C. S. 1995, ApJL, 444, L21
Bayless, A. J., Robinson, E. L., Mason, P. A., & Robertson, P. 2011, ApJ, 730, 43
Beran, J. 1994, Statistics for Long Memory Processes (New York: Chapman and Hall)
Beran, J., Feng, Y., Ghosh, S., & Kulik, R. 2013, Long Memory Processes: Probabilistic Properties and Statistical Methods (Berlin: Springer)
Bewketu Belete, A., Femmam, S., Tornikosk, M., et al. 2019, ApJ, 873, 108
Bhatta, G. 2019, MNRAS, 487, 3990
Bhatta, G., & Dhital, N. 2020, ApJ, 891, 120
Błażejowski, M., Blaylock, G., Bond, I. H., et al. 2005, ApJ, 630, 130
Bond, I. A., Udalski, A., Jaroszyński, M., et al. 2004, ApJL, 606, L155
Bosch-Ramon, V., Perucho, M., & Barkov, M. V. 2012, A&A, 539, A69
Box, G. E. P., Jenkins, G. M., & Reinsel, G. C. 1994, Time Series Analysis: Forecasting and Control (3rd ed.; Englewood Cliffs, NJ: Prentice-Hall)
Brajša, R., Wöhl, H., Hanslmeier, A., et al. 2009, A&A, 496, 855
Britzen, S., Fendt, C., Witzel, G., et al. 2018, MNRAS, 478, 3199
Brockwell, P. J. 2004, J. Appl. Probability, 41, 375
Brockwell, P. J., & Davis, R. A. 1996, Time Series: Theory and Methods (2nd ed.; New York: Springer-Verlag)
Brockwell, P. J., & Davis, R. A. 2002, Introduction to Time Series and Forecasting (2nd ed.; New York: Springer-Verlag)
Brockwell, P. J., & Marquardt, T. 2005, Statist. Sinica, 15, 477
Burbidge, E. M., & Kinman, T. D. 1966, ApJ, 145, 654
Burbidge, E. M., & Rosenberg, F. D. 1965, ApJ, 142, 1673
Burnham, K. P., & Anderson, D. R. 2004, Sociological Methods & Research, 33, 261
Caceres, G. A., Feigelson, E. D., Babu, G. J., et al. 2019, AJ, 158, 57
Caproni, A., Abraham, Z., & Monteiro, H. 2013, MNRAS, 428, 280
Caproni, A., Mosquera Cuesta, H. J., & Abraham, Z. 2004, ApJL, 616, L99
Carbone, F., Sorriso-Valvo, L., Alberti, T., et al. 2018, ApJ, 859, 27
Carnerero, M. I., Raiteri, C. M., Villata, M., et al. 2017, MNRAS, 472, 3789
Castignani, G., Pian, E., Belloni, T. M., et al. 2017, A&A, 601, A30
Cavaliere, A., Tavani, M., & Vittorini, V. 2017, ApJ, 836, 220
Chadwick, P. M., Lyons, K., McComb, T. J. L., et al. 1999, ApJ, 513, 161
Chandra, S., Zhang, H., Kushwaha, P., et al. 2015, ApJ, 809, 130
Chen, X., Fossati, G., Liang, E. P., & Böttcher, M. 2011, MNRAS, 416, 2368
Chen, X., Pohl, M., Böttcher, M., & Gao, S. 2016, MNRAS, 458, 3260
Collmar, W., Böttcher, M., Krichbaum, T. P., et al. 2010, A&A, 522, A66
Costamante, L., Ghisellini, G., Giommi, P., et al. 2001, A&A, 371, 512
Covino, S., Sandrinelli, A., & Treves, A. 2019, MNRAS, 482, 1270
Danforth, C. W., Nalewajko, K., France, K., & Keeney, B. A. 2013, ApJ, 764, 57
Deeming, T. J. 1975, Ap&SS, 36, 137
Deng, W., & Barkai, E. 2009, PhRvE, 79, 011112
Dichiara, S., Guidorzi, C., Amati, L., Frontera, F., & Margutti, R. 2016, A&A, 589, A97
Dichiara, S., Guidorzi, C., Frontera, F., & Amati, L. 2013, ApJ, 777, 132
Diltz, C., & Böttcher, M. 2016, ApJ, 826, 54

[28] https://reference.wolfram.com/language/ref/Fourier.html
[29] https://community.wolfram.com/groups/-/m/t/1081009
[30] https://reference.wolfram.com/language/ref/NonlinearModelFit.html
[31] https://reference.wolfram.com/language/ref/TimeSeriesModelFit.html
[32] https://pymc-devs.github.io/pymc/modelchecking.html

Dimitrov, W., Żywucka, N., Polińska, M., Kamiński, K., & Kamińska, M. K. 2018, AcA, 68, 269
Espaillat, C., Bregman, J., Hughes, P., & Lloyd-Davies, E. 2008, ApJ, 679, 182
Eyer, L., & Bartholdi, P. 1999, A&AS, 135, 1
Falomo, R., Kotilainen, J. K., & Treves, A. 2002, ApJL, 569, L35
Falomo, R., Pesce, J. E., & Treves, A. 1993, ApJL, 411, L63
Farge, M. 1992, AnRFM, 24, 395
Feigelson, E. D., Babu, G. J., & Caceres, G. A. 2018, FrP, 6, 80
Finke, J. D., & Becker, P. A. 2014, ApJ, 791, 21
Finke, J. D., & Becker, P. A. 2015, ApJ, 809, 85
Flandrin, P. 1992, ITIT, 38, 910
Foschini, L., Bonnoli, G., Ghisellini, G., et al. 2013, A&A, 555, A138
Foschini, L., Ghisellini, G., Tavecchio, F., et al. 2007, ApJL, 657, L81
Fossati, G., Buckley, J. H., Bond, I. H., et al. 2008, ApJ, 677, 906
Fraija, N., Benítez, E., Hiriart, D., et al. 2017, ApJS, 232, 7
Gallo, L. C., Blue, D. M., Grupe, D., Komossa, S., & Wilkins, D. R. 2018, MNRAS, 478, 2557
Gao, J. B., Cao, Y., & Lee, J.-M. 2003, PhLA, 314, 392
Garcia, O. E., & Theodorsen, A. 2017a, PhPl, 24, 020704
Garcia, O. E., & Theodorsen, A. 2017b, PhPl, 24, 032309
Gaur, H., Mohan, P., Wierzcholska, A., & Gu, M. 2018, MNRAS, 473, 3638
Gelman, A., & Rubin, D. B. 1992, StaSc, 7, 457
Ghisellini, G., & Tavecchio, F. 2008, MNRAS, 386, L28
Ghisellini, G., Tavecchio, F., Foschini, L., et al. 2010, MNRAS, 402, 497
Ghisellini, G., Tavecchio, F., Foschini, L., & Ghirlanda, G. 2011, MNRAS, 414, 2674
Gilfriche, P., Deschodt-Arsac, V., Blons, E., & Arsac, L. M. 2018, Front. Physiol, 9, 293
Gilmore, M., Yu, C. X., Rhodes, T. L., & Peebles, W. A. 2002, PhPl, 9, 1312
Giommi, P., Massaro, E., Chiappetti, L., et al. 1999, A&A, 351, 59
Golkhou, V. Z., & Butler, N. R. 2014, ApJ, 787, 90
Goyal, A. 2020, MNRAS, 494, 3432
Goyal, A., Stawarz, Ł., Zola, S., et al. 2018, ApJ, 863, 175
Granger, C. W. J., & Joyeux, R. 1980, J. Time Ser. Anal., 1, 15
Grech, D., & Mazur, Z. 2004, PhyA, 336, 133
Grech, D., & Mazur, Z. 2005, AcPPB, 36, 2403
Guidorzi, C., Dichiara, S., & Amati, L. 2016, A&A, 589, A98
Gupta, A. C., Mangalam, A., Wiita, P. J., et al. 2017, MNRAS, 472, 788
Gupta, A. C., Srivastava, A. K., & Wiita, P. J. 2009, ApJ, 690, 216
Gupta, A. C., Tripathi, A., Wiita, P. J., et al. 2019, MNRAS, 484, 5785
Halzen, F., Kheirandish, A., Weisgarber, T., & Wakely, S. P. 2019, ApJL, 874, L9
Hartman, R. C., Bertsch, D. L., Bloom, S. D., et al. 1999, ApJS, 123, 79
Hartman, R. C., Bertsch, D. L., Fichtel, C. E., et al. 1992, ApJL, 385, L1
Hayashida, M., Nalewajko, K., Madejski, G. M., et al. 2015, ApJ, 807, 79
H. E. S. S. Collaboration, Abdalla, H., Abramowski, A., et al. 2017, A&A, 598, A39
H. E. S. S. Collaboration, Abramowski, A., Acero, F., et al. 2013, A&A, 554, A107
Holgado, A. M., Sesana, A., Sandrinelli, A., et al. 2018, MNRAS, 481, L74
Hosking, J. R. M. 1981, Biometrika, 68, 165
Hovatta, T., Petropoulou, M., Richards, J. L., et al. 2015, MNRAS, 448, 3121
Hu, K., Ivanov, P. C., Chen, Z., Carpena, P., & Eugene Stanley, H. 2001, PhRvE, 64, 011114
Huarte-Espinosa, M., Krause, M., & Alexander, P. 2011, MNRAS, 418, 1621
Hurst, H. E. 1951, Trans. American Soc. Civil Engineers, 116, 770
Hurvich, C. M., & Tsai, C.-L. 1989, Biometrika, 76, 297
IceCube Collaboration, Aartsen, M. G., Ackermann, M., et al. 2018, Sci, 361, 147
Isobe, N., Sato, R., Ueda, Y., et al. 2015, ApJ, 798, 27
Jauncey, D. L., Reynolds, J. E., Tzioumis, A. K., et al. 1991, Natur, 352, 132
Jurkevich, I. 1971, Ap&SS, 13, 154
Kapanadze, B., Vercellone, S., Romano, P., et al. 2018, ApJ, 858, 68
Kasliwal, V. P., Vogeley, M. S., & Richards, G. T. 2017, MNRAS, 470, 3027
Kass, R. E., & Raftery, A. E. 1995, J. Am. Stat. Assoc., 90, 773
Kataoka, J., & Stawarz, Ł. 2016, ApJ, 827, 55
Katsev, S., & L'Heureux, I. 2003, CG, 29, 1085
Katz, J. I. 1997, ApJ, 478, 527
Kaulakys, B., Ruseckas, J., Gontis, V., & Alaburda, M. 2006, PhyA, 365, 217
Kaur, N., Baliyan, K. S., Chandra, S., Sameer, & Ganesh, S. 2018, AJ, 156, 36
Kelly, B. C., Bechtold, J., & Siemiginowska, A. 2009, ApJ, 698, 895
Kelly, B. C., Becker, A. C., Sobolewska, M., Siemiginowska, A., & Uttley, P. 2014, ApJ, 788, 33
Kelly, B. C., Sobolewska, M., & Siemiginowska, A. 2011, ApJ, 730, 52
Kendall, M., & Stuart, A. 1973, The Advanced Theory of Statistics (3rd ed.; London: Griffin)
Kendall, M. G. 1971, Biometrika, 58, 369
Kirby, J. F., & Swain, C. J. 2013, GeoJI, 194, 78
Knight, M. I., Nason, G. P., & Nunes, M. A. 2017, Stat. Comput., 27, 1453
Koen, C. 2005, MNRAS, 361, 887
Kulak, A., Kubisz, J., Klucjasz, S., et al. 2014, RaSc, 49, 361
Kułak, A., Młynarczyk, J., Zieba, S., Micek, S., & Nieckarz, Z. 2006, JGRA, 111, A10304
Kushwaha, P., Sinha, A., Misra, R., Singh, K. P., & de Gouveia Dal Pino, E. M. 2017, ApJ, 849, 138
Lachowicz, P., Gupta, A. C., Gaur, H., & Wiita, P. J. 2009, A&A, 506, L17
Lamb, R. C., & Macomb, D. J. 1997, ApJ, 488, 872
Lawrence, C. R., Bennett, C. L., Garcia-Barreto, J. A., Greenfield, P. E., & Burke, B. F. 1983, ApJS, 51, 67
Lenoir, G., & Crucifix, M. 2018a, NPGeo, 25, 145
Lenoir, G., & Crucifix, M. 2018b, NPGeo, 25, 175
Li, H. Z., Jiang, Y. G., Yi, T. F., et al. 2018, Ap&SS, 363, 45
Li, H. Z., Xie, G. Z., Dai, H., et al. 2010, NewA, 15, 254
Liang, E. W., & Liu, H. T. 2003, MNRAS, 340, 632
Liao, N. H., Bai, J. M., Liu, H. T., et al. 2014, ApJ, 783, 83
Lico, R., Liu, J., Giroletti, M., et al. 2020, A&A, 634, A87
Lidman, C., Courbin, F., Meylan, G., et al. 1999, ApJL, 514, L57
Lin, Y. C., Bertsch, D. L., Chiang, J., et al. 1992, ApJL, 401, L61
Liu, H., Liu, C., Wang, J. T. L., & Wang, H. 2019a, ApJ, 877, 121
Liu, H. T., Feng, H. C., Xin, Y. X., et al. 2019b, ApJ, 880, 155
Lomb, N. R. 1976, Ap&SS, 39, 447
Lynds, C. R. 1967, ApJ, 147, 837
MacLachlan, G. A., Shenoy, A., Sonbas, E., et al. 2013, MNRAS, 436, 2907
MAGIC Collaboration, Albert, J., Aliu, E., et al. 2008, Sci, 320, 1752
Malamud, B. D., & Turcotte, D. L. 1999, J. Stat. Planning Inference, 80, 173
Mallat, S. 2009, A Wavelet Tour of Signal Processing (3rd ed.; Boston, MA: Academic Press)
Mandelbrot, B. B., & van Ness, J. W. 1968, SIAMR, 10, 422
Mandelbrot, B. B., & Wallis, J. R. 1969, WRR, 5, 967
Mannattil, M., Gupta, H., & Chakraborty, S. 2016, ApJ, 833, 208
Marshall, K., Ryle, W. T., Miller, H. R., et al. 2009, ApJ, 696, 601
Martínez, V. J., Saar, E., Martínez-González, E., & Pons-Bordería, M.-J. 2009, LNP, 665, 1
Marti-Vidal, I., & Muller, S. 2019, A&A, 621, A18
MathWorks Inc. 2010, MATLAB v.7.11.0.584 (R2010b) (Natick, MA: MathWorks Inc.)
Mattox, J. R., Bertsch, D. L., Chiang, J., et al. 1993, ApJ, 410, 609
Merkin, V. G., Lyon, J. G., Lario, D., Arge, C. N., & Henney, C. J. 2016, JGRA, 121, 2866
Meyer, M., Scargle, J. D., & Blandford, R. D. 2019, ApJ, 877, 39
Miller, H. R. 1975, ApJL, 201, L109
Mlynarczyk, J., Kulak, A., & Salvador, J. 2017, RaSc, 52, 1245
Moreno, J., Vogeley, M. S., Richards, G. T., & Yu, W. 2019, PASP, 131, 063001
Morris, P. J., Chakraborty, N., & Cotter, G. 2019, MNRAS, 489, 2117
Mowlavi, N. 2014, A&A, 568, A78
Muno, M. P., Morgan, E. H., & Remillard, R. A. 1999, ApJ, 527, 321
Nair, S., Jin, C., & Garrett, M. A. 2005, MNRAS, 362, 1157
Nakagawa, K., & Mori, M. 2013, ApJ, 773, 177
Narayan, R., Igumenshchev, I. V., & Abramowicz, M. A. 2003, PASJ, 55, L69
Narayan, R., & Piran, T. 2012, MNRAS, 420, 604
Narayan, R., Sadowski, A., Penna, R. F., & Kulkarni, A. K. 2012, MNRAS, 426, 3241
Nevalainen, J., Markevitch, M., & Lumb, D. 2005, ApJ, 629, 172
Nieckarz, Z., Zieba, S., Kułak, A., & Michalec, A. 2009, MWRv, 137, 4401
Nilsson, K., Lindfors, E., Takalo, L. O., et al. 2018, A&A, 620, A185
Nilsson, K., Pursimo, T., Sillanpää, A., Takalo, L. O., & Lindfors, E. 2008, A&A, 487, L29
North, C. P., & Halliwell, D. I. 1994, MatG, 26, 531
Odzimek, A., Kułak, A., Michalec, A., & Kubisz, J. 2006, AnGeo, 24, 2151
Organokov, M., & Pradier, T. 2019, Proc. ICRC, 36, 972
Østensen, R. H., Reed, M. D., Baran, A. S., & Telting, J. H. 2014, A&A, 564, L14
Otero-Santos, J., Acosta-Pulido, J. A., Becerra González, J., et al. 2020, MNRAS, 492, 5524
Padovani, P. 2017, NatAs, 1, 0194
Padovani, P., Alexander, D. M., Assef, R. J., et al. 2017, A&ARv, 25, 2
Padovani, P., Giommi, P., Resconi, E., et al. 2018, MNRAS, 480, 192
Padovani, P., Oikonomou, F., Petropoulou, M., Giommi, P., & Resconi, E. 2019, MNRAS, 484, L104
Paiano, S., Falomo, R., Treves, A., & Scarpa, R. 2018, ApJL, 854, L32
Paliya, V. S., Sahayanathan, S., & Stalin, C. S. 2015, ApJ, 803, 15

Papadakis, I. E., & Lawrence, A. 1993, MNRAS, 261, 612
Pascual-Granado, J., Garrido, R., & Suárez, J. C. 2015, A&A, 575, A78
Pascual-Granado, J., Suárez, J. C., Garrido, R., et al. 2018, A&A, 614, A40
Patiño-Álvarez, V. M., Fernandes, S., Chavushyan, V., et al. 2018, MNRAS, 479, 2037
Pekeur, N. W., Taylor, A. R., Potter, S. B., & Kraan-Korteweg, R. C. 2016, MNRAS, 462, L80
Peng, C.-K., Buldyrev, S. V., Havlin, S., et al. 1994, PhRvE, 49, 1685
Peng, C.-K., Havlin, S., Stanley, H. E., & Goldberger, A. L. 1995, Chaos, 5, 82
Peñil, P., Domínguez, A., Buson, S., et al. 2020, ApJ, 896, 134
Pesnell, W. D. 2012, SoPh, 281, 507
Stawarz, Ł., & Petrosian, V. 2008, ApJ, 681, 1725
Phillipson, R. A., Boyd, P. T., & Smale, A. P. 2018, MNRAS, 477, 5220
Pihajoki, P., Valtonen, M., & Ciprini, S. 2013, MNRAS, 434, 3122
Pramesh Rao, A., & Subrahmanyan, R. 1988, MNRAS, 231, 229
Press, W. H., & Rybicki, G. B. 1989, ApJ, 338, 277
Principe, G., Malyshev, D., Ballet, J., & Funk, S. 2018, A&A, 618, A22
Prokhorov, D. A., & Moraghan, A. 2017, MNRAS, 471, 3036
Punch, M., Akerlof, C. W., Cawley, M. F., et al. 1992, Natur, 358, 477
Qian, S. J., Britzen, S., Krichbaum, T. P., & Witzel, A. 2019, A&A, 621, A11
Quinn, J., Akerlof, C. W., Biller, S., et al. 1996, ApJL, 456, L83
Raiteri, C. M., Villata, M., D'Ammando, F., et al. 2013, MNRAS, 436, 1530
Raiteri, C. M., Villata, M., Smith, P. S., et al. 2012, A&A, 545, A48
Rani, B., Gupta, A. C., Joshi, U. C., Ganesh, S., & Wiita, P. J. 2010a, ApJL, 719, L153
Rani, B., Gupta, A. C., Strigachev, A., et al. 2010b, MNRAS, 404, 1992
Rani, B., Krichbaum, T. P., Fuhrmann, L., et al. 2013, A&A, 552, A11
Rao, C. R. 1973, Linear Statistical Inference and its Applications (2nd ed.; New York: Wiley)
R Core Team 2016, R: A Language and Environment for Statistical Computing (Vienna: R Foundation for Statistical Computing), https://www.R-project.org/
Rieger, F. M. 2004, ApJL, 615, L5
Righi, C., Tavecchio, F., & Pacciani, L. 2019, MNRAS, 484, 2067
Rigon, L., Scholz, A., Anderson, D., & West, R. 2017, MNRAS, 465, 3889
Romero, G. E., Chajet, L., Abraham, Z., & Fan, J. H. 2000, A&A, 360, 57
Ryan, J. L., Siemiginowska, A., Sobolewska, M. A., & Grindlay, J. 2019, ApJ, 885, 12
Sandrinelli, A., Covino, S., Dotti, M., & Treves, A. 2016, AJ, 151, 54
Sandrinelli, A., Covino, S., & Treves, A. 2014, ApJL, 793, L1
Sandrinelli, A., Covino, S., Treves, A., et al. 2017, A&A, 600, A132
Sasada, M., Uemura, M., Fukazawa, Y., et al. 2014, ApJ, 784, 141
Sbarrato, T., Ghisellini, G., Maraschi, L., & Colpi, M. 2012, MNRAS, 421, 1764
Scargle, J. D. 1981, ApJS, 45, 1
Scargle, J. D. 1982, ApJ, 263, 835
Schulz, M., & Mudelsee, M. 2002, CG, 28, 421
Schwartz, D. A., Bradt, H. V., Doxsey, R. E., et al. 1978, ApJL, 224, L103
Schwarz, G. 1978, AnSta, 6, 461
Schwarzenberg-Czerny, A. 1996, ApJL, 460, L107
Seager, S., & Mallén-Ornelas, G. 2003, ApJ, 585, 1038
Serinaldi, F. 2010, PhyA, 389, 2770
Seymour, A. D., & Lorimer, D. R. 2013, MNRAS, 428, 983
Shaw, M. S., Romani, R. W., Cotter, G., et al. 2012, ApJ, 748, 49
Simonsen, I., Hansen, A., & Nes, O. M. 1998, PhRvE, 58, 2779
Sironi, L., Spitkovsky, A., & Arons, J. 2013, ApJ, 771, 54
Smith, K. L., Mushotzky, R. F., Boyd, P. T., & Wagoner, R. V. 2018, ApJL, 860, L10
Sobolewska, M. A., Siemiginowska, A., Kelly, B. C., & Nalewajko, K. 2014, ApJ, 786, 143
Stella, L., & Vietri, M. 1998, ApJL, 492, L59
Strittmatter, P. A., Carswell, R. F., Gilbert, G., & Burbidge, E. M. 1974, ApJ, 190, 509
Subrahmanyan, R., Narasimha, D., Pramesh Rao, A., & Swarup, G. 1990, MNRAS, 246, 263
Suková, P., Grzedzielski, M., & Janiuk, A. 2016, A&A, 586, A143
Suyal, V., Prasad, A., & Singh, H. P. 2009, SoPh, 260, 441
Tarnopolski, M. 2015a, MNRAS, 454, 1132
Tarnopolski, M. 2015b, Ap&SS, 359, 20
Tarnopolski, M. 2016, PhyA, 461, 662
Tarnopolski, M. 2019a, PhRvE, 100, 062144
Tarnopolski, M. 2019b, ApJ, 887, 97
Tavani, M., Cavaliere, A., Munar-Adrover, P., & Argan, A. 2018, ApJ, 854, 11
Tchekhovskoy, A. 2015, ASSL, 414, 45
The LIGO Scientific Collaboration, The Virgo Collaboration, Abbott, R., et al. 2019, arXiv:1912.11716
Thompson, D. J., Djorgovski, S., & de Carvalho, R. 1990, PASP, 102, 1235
Török, G., Abramowicz, M. A., Kluźniak, W., & Stuchlík, Z. 2005, A&A, 436, 1
Torre, K., Delignières, D., & Lemoine, L. 2007, British J. Math. Stat. Psych., 60, 85
Torrence, C., & Compo, G. P. 1998, BAMS, 79, 61
Tsai, H. 2009, Bernoulli, 15, 178
Tsai, H., & Chan, K. S. 2005, J. Royal Stat. Soc. Ser. B, 67, 703
Turley, C. F., Fox, D. B., Murase, K., et al. 2016, ApJ, 833, 117
Ulrich, M. H., Kinman, T. D., Lynds, C. R., Rieke, G. H., & Ekers, R. D. 1975, ApJ, 198, 261
Urry, C. M., & Padovani, P. 1995, PASP, 107, 803
Uttley, P., McHardy, I. M., & Papadakis, I. E. 2002, MNRAS, 332, 231
Uttley, P., McHardy, I. M., & Vaughan, S. 2005, MNRAS, 359, 345
Valtonen, M. J., Lehto, H. J., Nilsson, K., et al. 2008, Natur, 452, 851
VanderPlas, J. T. 2018, ApJS, 236, 16
Vaughan, S. 2005, A&A, 431, 391
Vaughan, S., Edelson, R., Warwick, R. S., & Uttley, P. 2003, MNRAS, 345, 1271
Vaughan, S., & Uttley, P. 2005, MNRAS, 362, 235
Vaughan, S., Uttley, P., Markowitz, A. G., et al. 2016, MNRAS, 461, 3145
Veitch, D., & Abry, P. 1999, ITIT, 45, 878
Vercellone, S., Striani, E., Vittorini, V., et al. 2011, ApJL, 736, L38
Villata, M., Raiteri, C. M., Larionov, V. M., et al. 2008, A&A, 481, L79
Vlahakis, N., & Königl, A. 2004, ApJ, 605, 656
von Neumann, J. 1941a, Annals Math. Stat., 12, 153
von Neumann, J. 1941b, Annals Math. Stat., 12, 367
Wagner, S. J., & Witzel, A. 1995, ARA&A, 33, 163
Weaver, Z. R., Balonek, T. J., Jorstad, S. G., et al. 2019, ApJ, 875, 15
Weron, A., Magdziarz, M., & Weron, K. 2008, PhRvE, 77, 036704
Wiklind, T., & Combes, F. 1996, Natur, 379, 139
Williams, J. D. 1941, Annals Math. Stat., 12, 239
Wojtaszczyk, P. 1997, A Mathematical Introduction to Wavelets: London Mathematical Society Student Texts (Cambridge: Cambridge Univ. Press),
Wolfram Research 2016, Mathematica v.10.4 (Champaign, IL: Wolfram Research, Inc.), https://www.wolfram.com
Woo, J.-H., & Urry, C. M. 2002, ApJ, 579, 530
Wood, M., Caputo, R., Charles, E., et al. 2017, Proc ICRC, 35, 824
Xie, F.-G., & Zdziarski, A. A. 2019, ApJ, 887, 167
York, D. 1966, CaJPh, 44, 1079
Zechmeister, M., & Kürster, M. 2009, A&A, 496, 577
Zhang, B.-B., Zhang, B., Murase, K., Connaughton, V., & Briggs, M. S. 2014, ApJ, 787, 66
Zhang, P.-f., Yan, D.-h., Liao, N.-h., & Wang, J.-c 2017a, ApJ, 835, 260
Zhang, P.-F., Yan, D.-H., Zhou, J.-N., et al. 2017b, ApJ, 845, 82
Zhou, J., Wang, Z., Chen, L., et al. 2018, NatCo, 9, 4599
Zunino, L., Olivares, F., Bariviera, A. F., & Rosso, O. A. 2017, PhLA, 381, 1021
Żywucka, N., Goyal, A., Jamrozy, M., et al. 2018, ApJ, 867, 131
Żywucka, N., Tarnopolski, M., Böttcher, M., Stawarz, Ł., & Marchenko, V. 2020, ApJ, 888, 107